

REPORT DOCUMENTATION PAGE			Form Approved OMB No. 0704-0188	
Public reporting burden for this collection of information is estimated to average 1 hour per response, including the time for reviewing instructions, searching existing data sources, gathering and maintaining the data needed, and completing and reviewing the collection of information. Send comments regarding this burden estimate or any other aspect of this collection of information, including suggestions for reducing this burden, to Washington Headquarters Services, Directorate for Information Operations and Reports, 1215 Jefferson Davis Highway, Suite 1204, Arlington, VA 22202-4302, and to the Office of Management and Budget, Paperwork Reduction Project (0704-0188), Washington, DC 20503.				
1. AGENCY USE ONLY (Leave blank)		2. REPORT DATE 11.Jan.99		3. REPORT TYPE AND DATES COVERED DISSERTATION
4. TITLE AND SUBTITLE THE ARCCOS AND LOMMEL DIFFRACTION AN APPROXIMATE FOURIER TRANSFORM PAIR LEADING TO A UNIFIED THEORY OF SPATIALLY AVERAGED DIFFRACTION CORRECTIONS FOR ULTRASONIC PISTON			5. FUNDING NUMBERS	
6. AUTHOR(S) CAPT DALY CHARLES J				
7. PERFORMING ORGANIZATION NAME(S) AND ADDRESS(ES) ROCHESTER INSTITUTE OF TECHNOLOGY			8. PERFORMING ORGANIZATION REPORT NUMBER	
9. SPONSORING/MONITORING AGENCY NAME(S) AND ADDRESS(ES) THE DEPARTMENT OF THE AIR FORCE AFIT/CIA, BLDG 125 2950 P STREET WPAFB OH 45433			10. SPONSORING/MONITORING AGENCY REPORT NUMBER FY99-44	
11. SUPPLEMENTARY NOTES				
12a. DISTRIBUTION AVAILABILITY STATEMENT Unlimited distribution In Accordance With AFI 35-205/AFIT Sup 1			12b. DISTRIBUTION CODE	
13. ABSTRACT (Maximum 200 words)				
1 9990216203				
14. SUBJECT TERMS			15. NUMBER OF PAGES	
			16. PRICE CODE	
17. SECURITY CLASSIFICATION OF REPORT			18. SECURITY CLASSIFICATION OF THIS PAGE	
19. SECURITY CLASSIFICATION OF ABSTRACT			20. LIMITATION OF ABSTRACT	

The Arccos and Lommel Diffraction Formulations: An Approximate Fourier Transform Pair Leading to A Unified Theory of Spatially Averaged Diffraction Corrections for Ultrasonic Piston Transducers Operating in Pulsed Mode

by

Charles J. Daly
Captain, United States Air Force

B.S., Electrical Engineering, Texas A & M University, College Station, Texas, 1988
M.S., Electrical Engineering, Air Force Institute of Technology,
Wright-Patterson Air Force Base, Ohio, 1992

A dissertation submitted in partial fulfillment of the
requirements for the degree of Doctor of Philosophy
to the Chester F. Carlson Center for Imaging Science
Rochester Institute of Technology

1998

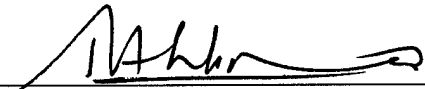
Signature of the Author Charles J. Daly
Accepted by Henry E. Ruddy August 5, 1998
Coordinator, Ph.D. Degree Program Date

CHESTER F. CARLSON CENTER FOR IMAGING SCIENCE
ROCHESTER INSTITUTE OF TECHNOLOGY
ROCHESTER, NEW YORK

CERTIFICATE OF APPROVAL

Ph.D. DEGREE DISSERTATION

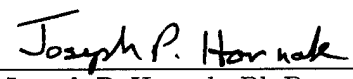
The Ph.D. Degree Dissertation of Captain Charles J. Daly
has been examined and approved by the
dissertation committee as satisfactory for the
dissertation required for the
Ph.D. degree in Imaging Science



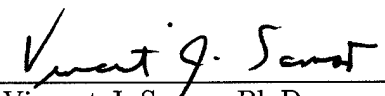
N. A. H. K. Rao, Ph.D., Dissertation Advisor



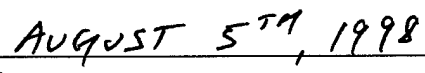
Roger L. Easton, Jr., Ph.D.



Joseph P. Hornak, Ph.D.



Vincent J. Samar, Ph.D.



Date

DISSERTATION RELEASE PERMISSION
ROCHESTER INSTITUTE OF TECHNOLOGY
CHESTER F. CARLSON CENTER FOR IMAGING SCIENCE

Title of Dissertation:

The Arccos and Lommel Diffraction Formulations: An Approximate Fourier Transform Pair Leading to A Unified Theory of Spatially Averaged Diffraction Corrections for Ultrasonic Piston Transducers Operating in Pulsed Mode

I, Charles J. Daly, hereby grant permission to Wallace Memorial Library of R.I.T. to reproduce my thesis in whole or in part. Any reproduction will not be for commercial use or profit.

Signature

Charles J. Daly

AUGUST 5, 1998

Date

The Arccos and Lommel Diffraction Formulations: An Approximate Fourier Transform Pair Leading to A Unified Theory of Spatially Averaged Diffraction Corrections for Ultrasonic Piston Transducers Operating in Pulsed Mode

by
Charles J. Daly

Submitted to the Chester F. Carlson Center for Imaging Science
in partial fulfillment of the requirements for the
Doctor of Philosophy Degree
at the Rochester Institute of Technology

Abstract

This work has three goals. The first is to derive closed-form spatially averaged two-way diffraction corrections for focused piston transducers operating in pulsed mode. The goal is attained by (i) establishing that the arccos and Lommel diffraction formulations form an approximate Fourier transform pair and (ii) exploiting this newly established Fourier equivalence in rigorous and original derivations of spatially averaged diffraction corrections for one-way and two-way diffraction. In addition to the first goal, this research has two larger goals. The first is to develop a unified theory of spatially averaged diffraction corrections for piston transducers. The second is to advance the scientific community's understanding of diffraction from a circular aperture, a ubiquitous and fundamental physical problem. When viewed in its entirety, this research attains these larger goals by presenting rigorous derivations and original analyses that unify and extend existing theory with generalized results and fresh insights. Finally, an aspect of the unified theory is tested in a practical application. Specifically, two-way diffraction corrections are applied to ultrasonic data obtained from laboratory experiments. The diffraction corrections are implemented as time-varying filters using a short-time Fourier technique known as the weighted overlap-add method. Raw and diffraction-corrected RF data are quantitatively compared via spectral centroids, and B-mode images are reconstructed from diffraction-corrected data.

Acknowledgements

This research had three goals. The first was to derive diffraction corrections for focused piston transducers. The second was to develop a unified theory of spatially averaged diffraction corrections. The last was to advance the scientific community's understanding of diffraction from a circular aperture. I have accomplished these goals. Indeed, it is fair to say that my work connects and puts in new perspective over a century of research on diffraction from a circular aperture. I owe my success to many people, and I publicly thank them here.

I am deeply indebted to the members of my dissertation committee. Dr. Hornak provided valuable criticism and suggested pedagogical improvements to the layout of this document. Dr. Easton inspired me with his unique perspective on life and linear system theory. Discussions with him streamlined at least one of my derivations and changed my life in some way, I'm sure. Dr. Samar asked challenging questions. Indeed, the questions he posed at our initial meeting changed the direction of my research for the better. Dr. Rao was my dissertation advisor. Professionally, he is a man of ideas, insight, and intelligence. He encouraged me every step along the way and was always a few steps ahead of me. Personally, he is a man of warmth, compassion, and good will. The best compliment I can pay Dr. Rao is to say that he seeks the truth. I thank Dr. Rao for all he has taught me. Additionally, I thank the United States Air Force for sending me to school.

Outside my committee, the faculty and staff at the Chester F. Carlson Center for Imaging Science were top-notch; they made everyday at RIT an enjoyable one. Many thanks to Marion Bleiler, Barb Capierso, Sue Chan, Carolyn Kitchen, and all the rest. Among my fellow students, Ajit, María, Gary and many others provided stimulating conversation and warm friendship. Mary Ellen gave me lots of chocolate, and Kevin Magde ensured I had a beer or two. Al, Daisei, and Lee made me pregnant during one annual Hunt, and they turned me over to the cops in another. Thanks, guys! Sorry to those RIT folks I missed. Finally, thanks to Aunt Peg & Uncle George, my youngest brother Dave, and my Ma who dared me to be different.

This work is dedicated to my family,
Rose of Sharon, Mister Charlie, and
especially my beloved wife,
Yon Hui,
and to my father,
Joseph C. Daly, Sr.,
who taught me the value of an education.
May he rest in peace.

Contents

List of Figures	x
1 Introduction	1
1.1 Ultrasonic Reflection Imaging	2
1.2 Diffraction from a Circular Aperture	4
1.3 The Arccos and Lommel Diffraction Formulations	7
1.4 One-way and Two-way Diffraction	8
1.5 Spatial Averaging	9
1.6 The Need for Diffraction Correction	12
1.7 Experimental Investigation	15
1.8 Analytical Investigation	15
1.9 Mathematical Definitions	16
1.10 Scope and Assumptions	17
1.11 Document Organization and Preview	19
1.12 Criticism and Counter	21
2 Literature Review	23
2.1 Ultrasonic Reflection Imaging	23
2.2 Diffraction from a Circular Aperture	24
2.3 Spatially Averaged Diffraction Corrections	25
2.4 Short-Time Fourier Techniques	27
2.5 Short-Time Fourier Techniques in Ultrasound	28
2.6 Chapter Summary	28
3 The Arccos and Lommel Diffraction Formulations	30
3.1 The Lommel Diffraction Formulation	31
3.2 The Arccos Diffraction Formulation	34
3.3 Similarities and Differences	37
3.4 Fourier Equivalence	38
3.5 Verification	41
3.6 Computational Considerations	44
3.7 The Focused Case	45
3.8 Chapter Summary	45

4	Spatially Averaged One-Way Diffraction	48
4.1	Spatially Averaged Arccos Diffraction Formulation	48
4.2	Spatially Averaged Lommel Diffraction Formulation	53
4.3	Extending Fourier Equivalence	55
4.4	Verification	56
4.5	Computational Considerations	64
4.6	Chapter Summary	64
5	Spatially Averaged Two-Way Diffraction	66
5.1	Spatially Averaged Arccos Diffraction Formulation	66
5.2	Spatially Averaged Lommel Diffraction Formulation	68
5.3	Extending Fourier Equivalence with Minimum Phase	71
5.4	Verification	72
5.5	Computational Considerations	74
5.6	Chapter Summary	79
6	Experimental Investigation	80
6.1	A Computational Consideration	81
6.2	Equipment, Parameters, and Processing	82
6.3	Experiments and Results	84
6.4	Discussion of Results	86
6.5	Chapter Summary	88
7	Analytical Investigation	114
7.1	One-way Diffraction	115
7.2	Two-Way Diffraction	118
7.2.1	Mirror-Image Diffraction	118
7.2.2	Autoconvolution Diffraction	119
7.2.3	Mirror-Image vs. Autoconvolution Diffraction	121
7.3	Two-Way Diffraction and Linear Models	124
7.4	Chapter Summary	126
8	Conclusions and Recommendations	147
8.1	Conclusions	147
8.1.1	Research Goals	147
8.1.2	Fourier Equivalence	148
8.1.3	Spatially Averaged One-Way Diffraction	149
8.1.4	Spatially Averaged Autoconvolution Diffraction	151
8.1.5	Experimental Investigation	151
8.1.6	Analytical Investigation	152
8.2	Recommendations for Improvement and Further Research	152
8.2.1	General	153
8.2.2	Fourier Equivalence	153
8.2.3	Spatially Averaged One-Way Diffraction	154
8.2.4	Spatially Averaged Autoconvolution Diffraction	154

8.2.5 More Experiments and Analysis	155
A Two Lemmas	157
Bibliography	159

List of Figures

1.1	Ultrasonic reflection imaging.	3
1.2	Example of diffraction.	5
1.3	Factors affecting diffraction.	6
1.4	Diffraction from a circular aperture.	7
1.5	Diffraction with point receiver/scatterer.	8
1.6	Realistic diffraction.	10
1.7	Tissue characterization.	13
3.1	Piston transducer and fictitious point receiver.	31
3.2	Pressures after Seki, <i>et al.</i> [56]	34
3.3	Point receiver impulse responses.	42
3.4	Focused impulse responses.	46
4.1	Piston transmitter and finite receiver.	50
4.2	A brachistochrone.	52
4.3	One-way spatially averaged impulse responses: $b = a/1000$	58
4.4	One-way spatially averaged impulse responses: $b = a/2$	59
4.5	One-way spatially averaged impulse responses: $b = a$	60
4.6	One-way spatially averaged impulse responses: $b = 2a$	61
4.7	One-way spatially averaged impulse responses: $b = 10a$	62
5.1	Piston transducer and reflecting disk.	68
5.2	Two-way spatially averaged impulse responses: $b = a/1000$	75
5.3	Two-way spatially averaged impulse responses: $b = a/2$	76
5.4	Two-way spatially averaged impulse responses: $b = a$	77
5.5	Two-way spatially averaged impulse responses: $b = 2a$	78
6.1	Reflecting disk in main beam.	81
6.2	Experimental set-up.	83
6.3	Short-time Fourier processing of A-lines.	85
6.4	Raw and diffraction-corrected envelope data.	87
6.5	Breast tissue on sponge: 2.25 MHz unfocused	89
6.6	Magnitude response	90

6.7	Phase response	91
6.8	Breast tissue on sponge: 5.0 MHz unfocused	92
6.9	Magnitude response	93
6.10	Phase response	94
6.11	Pig liver on sponge: 2.25 MHz unfocused	95
6.12	Magnitude response	96
6.13	Phase response	97
6.14	Pig liver on sponge: 2.25 MHz long focus	98
6.15	Magnitude response	99
6.16	Pig liver on sponge: 5.0 MHz unfocused	100
6.17	Magnitude response	101
6.18	Phase response	102
6.19	Pig liver on sponge: 5.0 MHz long focus	103
6.20	Magnitude response	104
6.21	Disk phantom: 2.25 MHz medium focus	105
6.22	Magnitude response	106
6.23	Disk phantom: 3.5 MHz medium focus	107
6.24	Magnitude response	108
6.25	Disk phantom: 5.0 MHz medium focus	109
6.26	Magnitude response	110
6.27	Wire targets: 2.25 MHz unfocused	111
6.28	Magnitude response	112
6.29	Phase response	113
7.1	Near-field attenuation.	115
7.2	Near-field and far-field attenuation.	116
7.3	Unfocused autoconvolution: $b = a/1000$	128
7.4	Long focus autoconvolution: $b = a/1000$	129
7.5	Medium focus autoconvolution: $b = a/1000$	130
7.6	Short focus autoconvolution: $b = a/1000$	131
7.7	Unfocused autoconvolution: $b = a/10$	132
7.8	Long focus autoconvolution: $b = a/4$	133
7.9	Medium focus autoconvolution: $b = a/4$	134
7.10	Short focus autoconvolution: $b = a/4$	135
7.11	Unfocused autoconvolution: $b = a$	136
7.12	Long focus autoconvolution: $b = a$	137
7.13	Medium focus autoconvolution: $b = a$	138
7.14	Short focus autoconvolution: $b = a$	139
7.15	Mirror-image and autoconvolution: unfocused.	140
7.16	Mirror-image and autoconvolution: long locus.	141
7.17	Mirror-image and autoconvolution: medium focus.	142
7.18	Mirror-image and autoconvolution: short focus.	143
7.19	One-way point receiver response	144
7.20	Two-way autoconvolution point scatterer response	145
7.21	Two-way mirror-image point scatterer response	146

Chapter 1

Introduction

This work has three goals. The first and most immediate is to derive a closed-form spatially averaged two-way diffraction correction for a focused piston transducer operating in pulsed mode. The immediate goal is attained by (i) establishing that, in the case of one-way diffraction with a point receiver, the arccos and Lommel diffraction formulations form an approximate Fourier transform pair and (ii) exploiting this newly established Fourier equivalence in rigorous and original derivations of spatially averaged diffraction corrections for both one-way and two-way diffraction. In addition to the immediate goal, this research has two larger goals. The first is to develop a unified theory of spatially averaged diffraction corrections for piston transducers. The second is to advance the scientific community's understanding of diffraction from a circular aperture. When viewed in its entirety, this research attains these two goals by presenting rigorous derivations and original analyses that unify and extend previously disjoint and limited theory with fresh insights and generalized results. Finally, an aspect of the new unified theory is applied to gauge the practicality of the theory. Specifically, two-way diffraction corrections are applied to ultrasonic data obtained from laboratory experiments. The diffraction corrections are time-varying filters implemented with a short-time Fourier technique known as the weighted overlap-add method. Raw and diffraction-corrected RF data are quantitatively compared via spectral centroids, and B-mode images are reconstructed from diffraction-corrected data.

Diffraction from a circular aperture is a ubiquitous and fundamental physical problem. Its occurrence in optics (lenses), acoustics (loudspeakers), electromagnetics (dish antennas) and ultrasonics (piston transducers) testifies to its ubiquity, while its fundamental nature is found in its simple description coupled with its not-so-simple set of solutions—solutions which have preoccupied scientific minds since 1885 at least.

What is diffraction from a circular aperture, and why bother looking at a problem that has been investigated off and on for over a century? What do terms such as *spatially averaged*, *two-way*, and *pulsed-mode* mean? And why are they important? How does diffraction from a circular aperture arise in the context of ultrasound?

The purpose of this chapter is to answer these and other questions and, in so doing, introduce concepts and definitions used in later chapters. The emphasis at this stage is on pedagogy rather than precision. Also included in this chapter is a section which delineates the scope of the research; the same section also states underlying assumptions. Another section previews the remaining chapters, and a final section refutes two potential objections to the unified theory being proposed.

1.1 Ultrasonic Reflection Imaging

In a biomedical context, an ultrasonic transducer generates and couples a sound wave to the anatomy under examination (Fig. 1.1). The sound wave interacts with tissue and is scattered as it propagates. Some of the scattered energy reflects back to the transducer. The acoustic energy of the reflected wave is received and converted into a voltage that varies as a function of time. The voltage at the output of the receiver shown in Fig. 1.1 is known as an *A-line*.

An A-line is a radio-frequency (RF) voltage whose spectrum is centered about a particular frequency. The RF A-line can be analyzed at RF or, more commonly, its center frequency can be brought to baseband via a process known as *envelope detection* and subsequently displayed as an intensity line. This is known as *A-mode* imaging [4].

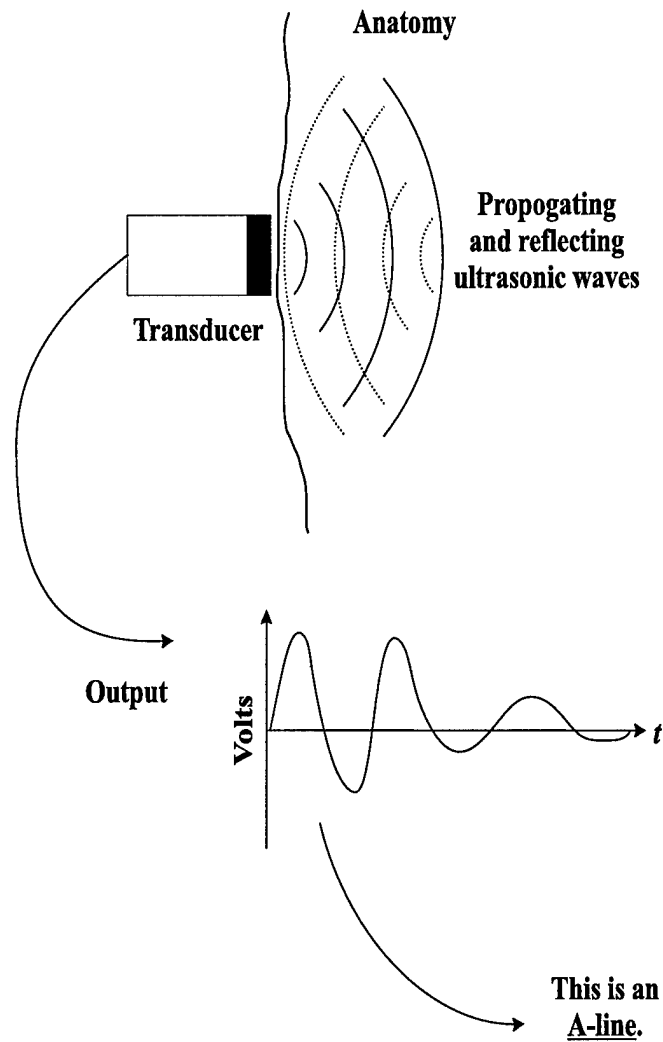


Figure 1.1: Ultrasonic reflection imaging.

As an aside, RF data is high-frequency data, while baseband or envelope-detected data is low-frequency data. See Gagliardi [21] for definitions of *RF* and *baseband*.

The transducer can be moved laterally and a 2-D array of RF A-lines built up. Each RF A-line in the 2-D array can be processed via envelope detection and subsequently displayed as a gray-scale image. This is known as *B-mode* imaging. Gray-scale obstetric images (a baby in a mother's tummy, if you will) are familiar examples of B-mode imaging.

Both A-mode and B-mode reflection imaging are similar to radar. The transducer sends out ultrasonic energy and detects what energy is reflected back. Like an antenna in radar, the transducer in ultrasonic reflection imaging acts as both transmitter and receiver.

In terms of efficiency and cost, ultrasonic imaging is much faster and cheaper than other imaging modalities such as X-ray and magnetic resonance imaging (MRI). But in terms of resolution and contrast, ultrasonic imaging is vastly inferior to these same imaging modalities. One cause for the inferior quality of ultrasonic imaging is diffraction, the topic of the next section.

1.2 Diffraction from a Circular Aperture

The phenomenon known as *diffraction* is fundamental to the study of wave propagation through an aperture of any shape. However, only circular apertures are considered in this research. Diffraction from a circular aperture can be described with a simple, yet familiar, example from optics. Consider shining a flashlight on a wall in a dark room. The illumination on the wall depends on the distance between the flashlight and the wall—the larger the distance between the flashlight and the wall, the dimmer the illumination but the greater the illuminated area; the smaller the distance, the brighter the illumination but the smaller the illuminated area. More succinctly, brightness is inversely proportional in some fashion to distance, while illuminated area is proportional in some fashion to distance. Fig. 1.2 illustrates this familiar example and depicts diffraction as beam or energy spread. Diffraction affects acoustic and ultrasonic energy in a similar fashion. A loudspeaker and piston transducer are quintessential examples of diffraction from a circular aperture in acoustics and ultrasonics, respectively.

The important point is that diffraction causes waves to spread in a spatially varying fashion. In ultrasound, distance or depth z is related to time t via $z = ct/2$ where c is the speed of sound. Thus, the effects of ultrasonic diffraction change with time, and correcting for the effects of ultrasonic diffraction will require time-varying filtering. This simplistic

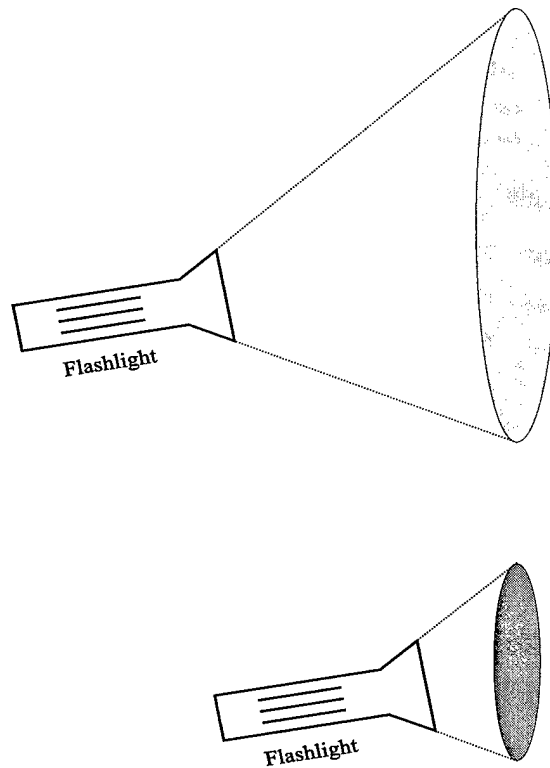


Figure 1.2: Simple example of diffraction.

characterization of diffraction as spatially varying beam spread becomes inadequate when other factors, such as aperture size, frequency, and focusing, are considered.

The term *monochromatic* implies single-frequency or continuous wave excitation. For monochromatic excitation of a given frequency, the distance from the aperture at which noticeable beam spread begins is proportional in some fashion to the aperture size. Similarly, for a given aperture size, the distance from the aperture at which noticeable beam spread begins is proportional in some fashion to the excitation frequency. Focusing adds even more complexity. Fig. 1.3 illustrates how changes in aperture size, frequency, and focusing affect diffraction from a piston transducer.

Fig. 1.3 implies that the beam is approximately collimated out to a certain distance and then begins to diverge. The notion of a clear-cut demarcation between collimated and

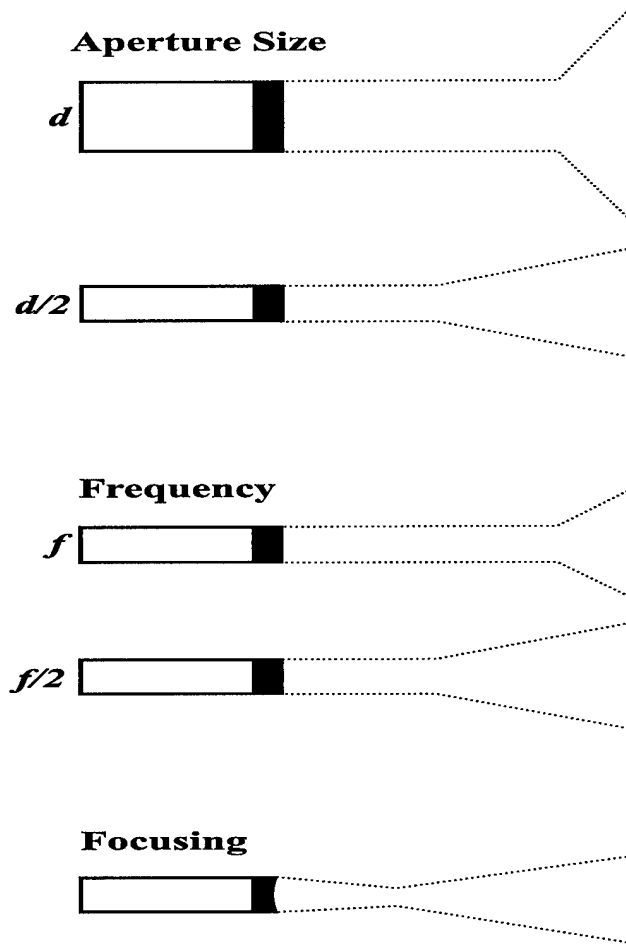


Figure 1.3: Factors affecting diffraction.

diverging regions is a useful oversimplification and applies to monochromatic excitation only. Furthermore, the collimated and diverging regions are loosely associated with the *near field* and *far field*, respectively [22]. The importance of these observations will be clarified later.

The term *polychromatic* implies multi-frequency or pulsed excitation; a piston transducer operating in pulsed mode is said to be excited polychromatically or impulsively. And describing the diffraction effects becomes exceedingly complicated if the transducer excitation is polychromatic. In this case, there are collimated and diverging regions associated with each frequency contained in the excitation.

1.3 The Arccos and Lommel Diffraction Formulations

The discussion of diffraction can be put on a more mathematical footing by considering Fig. 1.4 and introducing the scalar function $H_1(\rho, z, \omega)$ which characterizes the disturbance

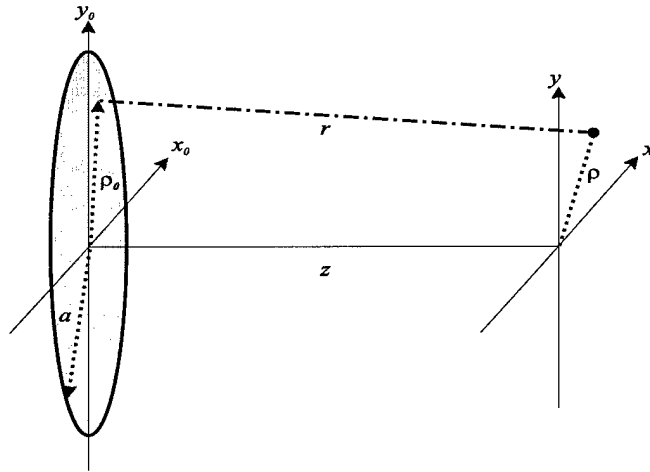


Figure 1.4: Diffraction from a circular aperture.

sensed by a point receiver at a radial distance ρ from the axis due to some monochromatic excitation of the aperture. It can be shown [24] that $H_1(\rho, z, \omega)$ satisfies the time-independent Helmholtz wave equation:

$$(\nabla^2 + k^2)H_1(\rho, z, \omega) = 0. \quad (1.1)$$

Lommel [25] investigated this problem in 1885, and his solution for $H_1(\rho, z, \omega)$ is the Lommel diffraction formulation. In 1961, Oberhettinger [44] characterized the disturbance at the point ρ due to pulsed or impulsive excitation of the aperture, and his solution is the arccos diffraction formulation.

For now, attention is drawn to the fact that the two formulations are similar in that they both characterize the effects of *one-way* diffraction from a circular aperture at a *point* (an infinitesimally small area); thus, the arccos and Lommel diffraction formulations seem amenable to some type of unification. Much more will be said about these two formulations

and their heretofore overlooked connection in Chapter 3. The distinction between one-way and two-way diffraction and its importance is explained in the next section.

1.4 One-way and Two-way Diffraction

From a physical standpoint, one-way diffraction implies energy travel in one direction—away from the source. Two-way diffraction implies energy travel in two directions—first away from the source and then back to source after interaction with matter. The physical distinction is illustrated in Fig. 1.5 for a point receiver and point scatterer. This distinction is

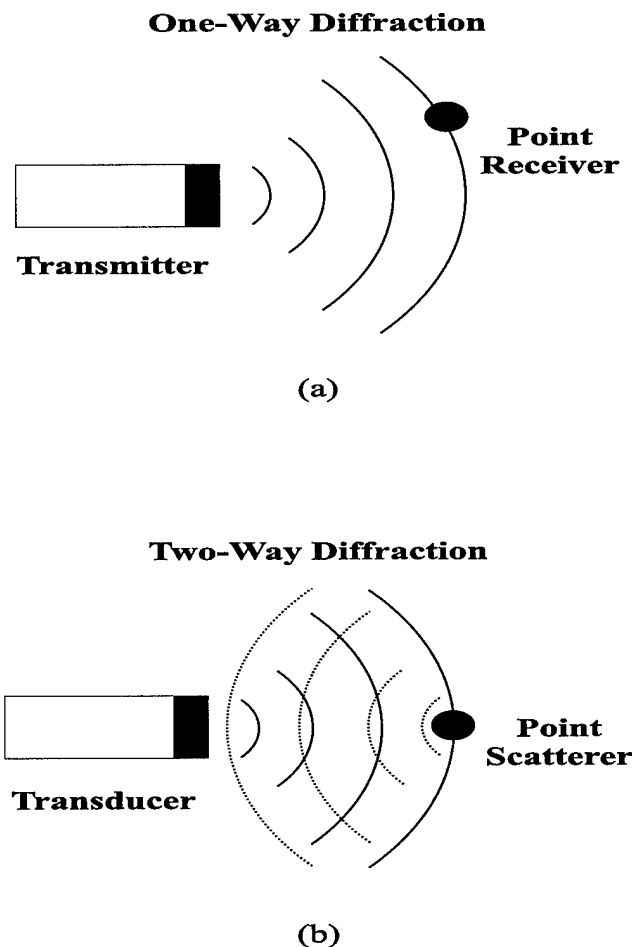


Figure 1.5: (a) One-way diffraction with point receiver; (b) two-way diffraction with point scatterer.

particularly important in ultrasonic reflection imaging because it is subject to mathematical interpretation.

Specifically, some authors state that equations derived for one-way diffraction can be used to calculate two-way diffraction simply by doubling the distance between the source and scatterer in the one-way equations [11, 33, 52, 56, 67]. This claim is based on a *mirror-image* interpretation of two-way diffraction. On the other hand, some authors state that two-way diffraction is properly described by the square of $H_1(\rho, z, \omega)$ [18, 29, 64]. This claim is based on an interpretation of two-way diffraction as an autoconvolution. Both interpretations have merit and mathematical appeal. Because of this, closed-form spatially averaged equations applicable to both interpretations will be derived in later chapters.

A note on terminology is required at this point. The physical distinction between one-way and two-way diffraction coupled with the mirror-image and autoconvolution interpretations of two-way diffraction leads to a rich but potentially confusing taxonomy. The confusion arises because the term *two-way diffraction* is imprecise; it may imply either the mirror-image or autoconvolution interpretation of two-way diffraction. Here, the term *two-way diffraction* is associated with the autoconvolution interpretation. The terms *mirror-image diffraction* and *autoconvolution diffraction*, although awkward, will be used when the mathematical interpretation of two-way diffraction requires specification. More will be said about mirror-image and autoconvolution diffraction in Section 1.8.

1.5 Spatial Averaging

The discussion up to this point has focused on fictitious point receivers and point scatterers. The receiving area of a real transducer, however, is finite, and real transducers are often referred to as *finite receivers*. Fig. 1.6 depicts more realistic scenarios for one-way and two-way ultrasonic diffraction. In the one-way case, an ultrasonic transducer emits energy and another transducer coaxially located with the transmitter some distance z away acts as a receiver.

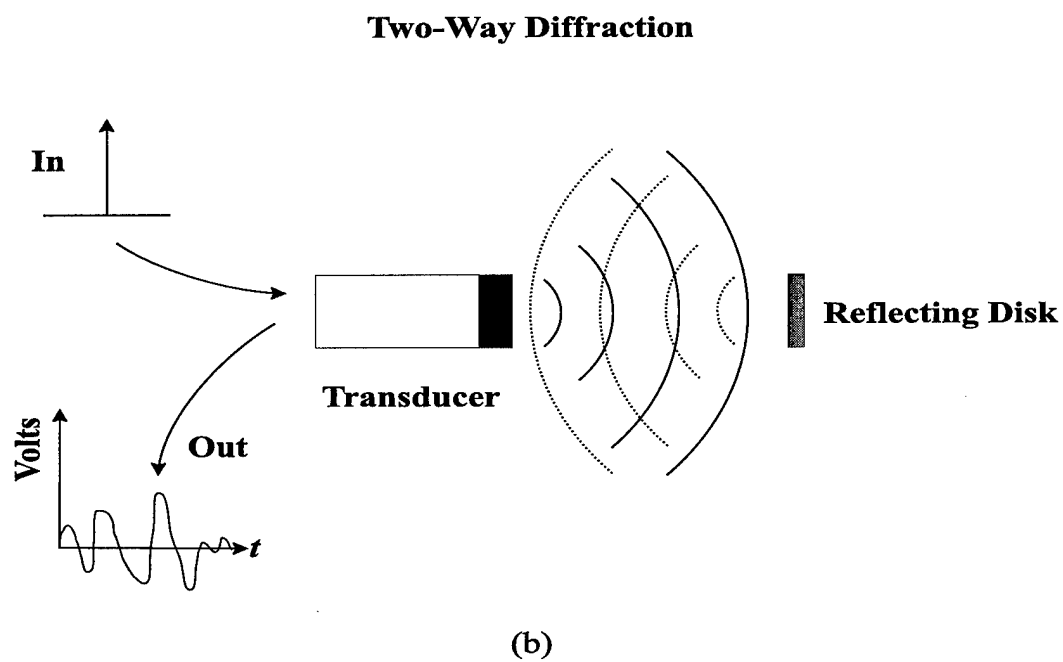
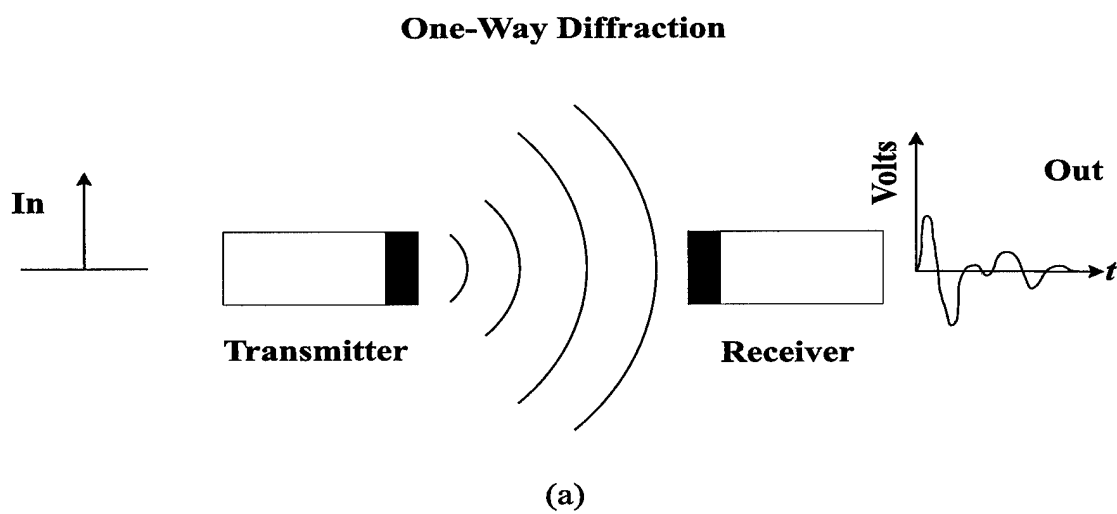


Figure 1.6: (a) One-way diffraction with finite receiver; (b) two-way diffraction with finite reflecting disk.

The usual goal of one-way ultrasonic probing is to extract information about the medium between the transmitter and receiver. This information is encoded on the RF A-line. Recall that an A-line is the output voltage of the receiver and is illustrated in Fig. 1.1. The A-line is assumed to be a function of either the total pressure or spatially averaged pressure impinging on the face of the receiver [5, 10, 27, 67]. Williams makes the case for total pressure, while Harris makes the case for spatially averaged pressure. In either case, total pressure is found by spatial integrating the incoming pressure field over the face of the receiving aperture; note that the receiving aperture is referred to as a *measurement circle* by Williams [66]. Spatially averaging consists of simply dividing the total pressure by the receiver area. Since spatial integration and spatial averaging differ only by a constant multiplicative factor, both can be said to give a relative quantitative estimate of one-way diffraction effects.

Spatial averaging of one-way ultrasonic diffraction has been investigated extensively, and, numerous authors have used one-way results to explain two-way diffraction by invoking the mirror-image interpretation of reflection imaging. Chapter 4 extends existing theory by presenting new derivations of time-domain and frequency-domain results for one-way diffraction.

In the autoconvolution interpretation of reflection imaging, diffraction occurs during transmission and reflection. In this case, total pressure is found by spatial integrating the incoming (reflected) pressure field over the receiving aperture; the reflected pressure, in turn, is found by spatially integrating the outgoing (transmitted) pressure field over some suitably chosen reflecting plane [9, 18]. Averaging consists of dividing by the area of the receiving aperture.

Spatial averaging over a volume is more realistic because, at any given instant after insonification, acoustic energy is reflected back from a mass or three-dimensional (3-D) volume of material rather than from a disk. Thus, ultrasonic reflection imaging is a volumetric or 3-D imaging modality. However, the only observation available in non-Doppler reflection imaging is a set of A-lines, that is, one-dimensional (1-D) time-domain voltage

signals. In essence, an A-line contains information about a 3-D volume of material and that information has been encoded via spatial averaging onto a 1-D time-domain waveform. Averaging over a volume may be more realistic, but is also more difficult to compute. Thus, spatial averaging over disks is quite common in the literature on ultrasound.

Spatially averaged autoconvolution diffraction has not been investigated as extensively as spatially averaged one-way diffraction, [9] being a notable exception. Chapter 5 attacks autoconvolution diffraction with new tactics; there it is empirically shown that closed-form results derived by Wolf in 1951 for optical diffraction can be used to estimate a spatially averaged form of autoconvolution diffraction in ultrasonic reflection imaging. This new but relatively straightforward empirical proof is based on the Cauchy-Schwarz inequality for integrals [48, pp. 177-178] and an *ad hoc* assumption concerning its interpretation. Despite the *ad hoc* and empirical development, useful results are obtained.

1.6 The Need for Diffraction Correction

Terms such as *spatially averaged*, *two-way*, and *pulsed-mode* have been defined and their importance explained in the context of ultrasound. The phenomenon of diffraction from a circular aperture and its applicability to ultrasonic reflection imaging have been considered. The question of why a century-old problem is being investigated again remains. The inescapably long answer explains the need to correct for ultrasonic diffraction and can be found in an area of ultrasonic research known as *tissue characterization* [17, 39].

Tissue characterization has been called the Holy Grail of ultrasound [50]. Radiologists, when limited to diagnosis via ultrasound, are already very good at *differentiating* between healthy and diseased tissue. They are not yet as adept at *characterizing* or *classifying* the diseased tissue when presented with the same B-mode images. One of the reasons radiologists are not adept at classifying diseased tissue is their almost exclusive reliance on B-mode images when limited to ultrasonic diagnoses. Recall, B-mode images are constructed from low-frequency envelope-detected data.

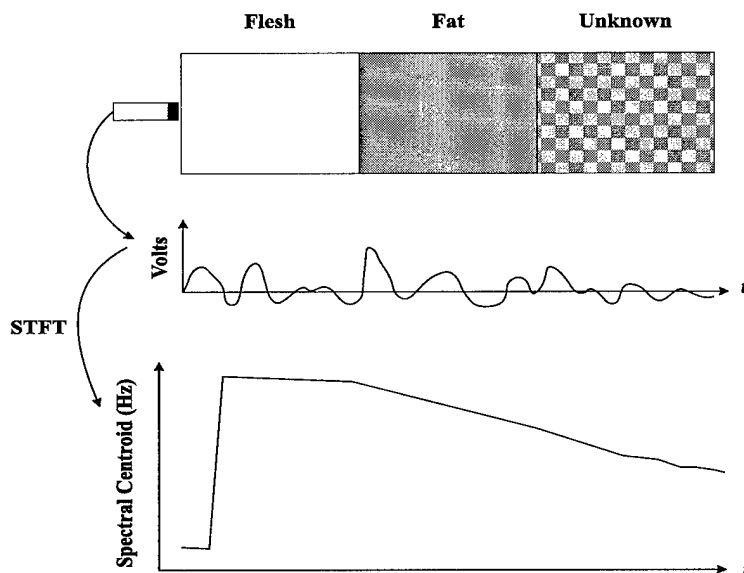


Figure 1.7: Tissue characterization.

Thus, a radiologist examining a B-mode image does not see all the data; he or she is making a radiological diagnosis based primarily on low-frequency envelope-detected data. Any potentially important diagnostic information encoded on the high-frequency RF data is lost as a result of envelope detection. Thus, biopsy, an invasive and expensive procedure, remains the gold standard for tissue characterization.

Researchers in ultrasonic tissue characterization are trying to avoid invasive and expensive biopsy procedures by giving radiologists new tools and methods to make reliable tissue classifications based solely on ultrasound data. And many methods of tissue characterization involve spectral analysis of RF data [20,58]. Tissue characterization based on spectral analysis combines diagnostic information from low-frequency envelope-detected data—B-mode images—with additional information available from the high-frequency data—RF A-lines. Advanced digital signal processing offers many methods of obtaining this additional information from the high-frequency data. Fig. 1.7 illustrates a notional example. For simplicity, only one A-line is considered. The figure shows three layers of tissue and the RF A-line obtained by probing the layers with a piston transducer operating in pulsed-mode.

A measure of the average or dominant frequency contained in the RF A-line—its spectral centroid [20]—can be obtained via short-time Fourier processing. A notional spectral centroid is shown in the figure. The spectral centroid varies in some quantitative fashion that correlates, at least theoretically, with the type of tissue being probed. This theoretical correlation, however, is complicated by diffraction effects. Specifically, the spectral centroid is based on high-frequency RF data, but diffraction, as will be shown, attenuates high-frequency information. Thus, the spectral centroid will be biased by high-frequency attenuation unless the diffraction effects are corrected in some fashion. Furthermore, physically meaningful correction of two-way diffraction effects for finite receivers requires spatial averaging.

Derivation of a spatially averaged autoconvolution diffraction correction using the arccos diffraction formulation [59] was attempted but proved too difficult. This difficulty prompted our investigation of the Lommel diffraction formulation, a solution to the century-old problem of monochromatic diffraction from a circular aperture. As will be shown, deriving and implementing a spatially averaged autoconvolution diffraction correction turns out to be fairly straightforward once the Fourier equivalence of the arccos and Lommel diffraction formulations is established.

In summary, diffraction attenuates high-frequency information and biases tissue characterization; hence, a correction is required to remove the bias caused by diffraction. We derive equations describing diffraction effects as a set of time/depth-varying filters. These diffraction filters are simply inverted to obtain diffraction corrections.

A note on terminology is required at this point. Note that the term *diffraction correction* can be interpreted as the total removal of unwanted diffraction effects. No such claim is made for this process. The time-varying filters derived here simply compensate for depth-dependent high-frequency attenuation caused by diffraction, and the term *correction* is used loosely. Furthermore, the distinction between diffraction *effects* and diffraction *correction* is simply a matter of inversion, and the two terms are often used interchangeably in the literature on diffraction correction. The same semantic liberty is taken here.

1.7 Experimental Investigation

Up to this point, only theoretical results have been promised. While it is true that theory precedes application, it is also true that application of theory is better sooner than later. Thus, an aspect of the unified diffraction theory developed here is investigated experimentally in Chapter 6. Specifically, autoconvolution diffraction corrections will be implemented with time-varying filters, and diffraction-corrected B-mode images will be reconstructed using a short-time Fourier analysis/synthesis algorithm known as the weighted overlap-add (WOLA) method. The raw and diffraction-corrected images will be compared only qualitatively. Differences between raw and corrected RF data will be analyzed quantitatively via the spectral centroids described in the previous section.

Three points concerning the experiments require discussion. First, it must be emphasized that the experiments were not designed to validate the theory in any authoritative fashion. Rather, they were designed to gauge the feasibility of the proposed autoconvolution diffraction correction. Second, the diffraction-corrected images are an important contribution of this work. Although the differences between the raw and diffraction-corrected images are subtle, they reveal that diffraction correction appears to have a more pronounced effect on RF data than on envelope-detected data. *Finally and most importantly, the experiments are not to be considered, in any way, clinical validation of the proposed diffraction corrections.*

1.8 Analytical Investigation

A theory is gauged by its simplicity, practicality, and predictive power. Predictions based on the proposed unified theory are investigated analytically in Chapter 7. In particular, predictions based on the mirror-image and autoconvolution interpretations of two-way diffraction are compared. Until now, the two interpretations have not been quantitatively compared because closed-form expressions allowing comparison did not exist. The closed-form equations developed as part of the proposed unified theory permit a new quantitative analysis of

the two interpretations. This quantitative comparison reveals that these two interpretations of two-way diffraction are similar in much narrower sense than was previously realized.

1.9 Mathematical Definitions

The development of a unified theory of spatially averaged diffraction corrections for piston transducers is made possible, in part, by a group of related mathematical functions which will surface repeatedly in later chapters. Following Wolf [68], u and v are real variables, n and m are non-negative integers, and $J_n(u)$ is a Bessel function of the first kind of order n . U_n and V_n are Lommel functions of two variables and are defined by summations of Bessel functions:

$$U_n(u, v) = \sum_{s=0}^{\infty} (-1)^s \left(\frac{u}{v}\right)^{n+2s} J_{n+2s}(v), \quad (1.2)$$

$$V_n(u, v) = \sum_{s=0}^{\infty} (-1)^s \left(\frac{v}{u}\right)^{n+2s} J_{n+2s}(v). \quad (1.3)$$

Because they are infinite summations, the Lommel functions can be computed only approximately, and these approximations can be programmed either recursively [25, 68] or directly in a do-loop. Do-loops were used in this research.

$U_n(u, v)$ converges slowly for when $u/v > 1$, and so the following formulae from Gray and Mathews [25, p. 185, Eq. 20] will prove useful:

$$U_{2n+1}(u, v) + V_{-2n+1}(u, v) = (-1)^n \sin \left(\frac{1}{2} \left[u + \frac{v^2}{u} \right] \right), \quad (1.4a)$$

$$-U_{2n}(u, v) + V_{-2n}(u, v) = (-1)^n \cos \left(\frac{1}{2} \left[u + \frac{v^2}{u} \right] \right). \quad (1.4b)$$

Special-case formulae for $u/v = 1$ can be found in Gray and Mathews. A group of related functions will also be encountered:

$$\begin{aligned} Z_n(u, v) &= (-1)^s U_{n+2s}(u, v), \\ &= \sum_{s=0}^{\infty} (-1)^s (s+1) \left(\frac{u}{v}\right)^{n+2s} J_{n+2s}(v); \end{aligned} \quad (1.5)$$

$$W_n(u, v) = (-1)^s V_{n+2s}(u, v), \quad (1.6)$$

$$= \sum_{s=0}^{\infty} (-1)^s (s+1) \left(\frac{v}{u}\right)^{n+2s} J_{n+2s}(v);$$

$$X_n(u, v) = \frac{1}{2} \left[\frac{v^2}{u} V_{n-1}(u, v) + u V_{n+1}(u, v) \right], \quad (1.7)$$

$$= \sum_{s=0}^{\infty} (-1)^s (n+2s) \left(\frac{u}{v}\right)^{n+2s} J_{n+2s}(v) \quad \text{and}$$

$$Y_n(u, v) = \frac{1}{2} \left[\frac{v^2}{u} U_{n+1}(u, v) + u U_{n-1}(u, v) \right], \quad (1.8)$$

$$= \sum_{s=0}^{\infty} (-1)^s (n+2s) \left(\frac{v}{u}\right)^{n+2s} J_{n+2s}(v).$$

$Z_n(u, v)$ was encountered in the course of this work, and it is discussed in Appendix A. More on details on $W_n(u, v)$, $X_n(u, v)$, and $Y_n(u, v)$ and their origins and applications can be found in [68, 69]. Finally, the polynomials

$$P_{n,2m}(v) = \sum_{s=0}^{2m} (-1)^s J_{n+2}(v) J_{n+2m-s}(v) \quad (1.9)$$

$$Q_{2m} = P_{0,2m}(v) + P_{1,2m}(v) \quad (1.10)$$

will be encountered.

At this point, an important historical disclaimer is required. With the exception perhaps of $Z_n(u, v)$, all functions introduced in this section are due to Lommel, Hopkins, or Wolf. See Watson [63], Gray and Mathews [25], and Wolf [68, 69] for more details. Indeed, the closed-form equations derived herein were made possible, in large part, by results presented in Wolf's 1951 paper on diffraction; the importance of Wolf's results to this work cannot be overstated.

1.10 Scope and Assumptions

This section describes the scope of the proposed work and explains some choices and assumptions that have been made. More details will be discussed as the need arises. This

research focuses on A-mode and B-mode biomedical ultrasonic reflection imaging using pulse-echo techniques. M-mode, pulsed-Doppler, color-flow, tomographic, and more exotic ultrasonic imaging modalities are not discussed. In short, the scope of this research is limited to non-Doppler pulse-echo reflection imaging. Ultrasound experiments were conducted with piston transducers which were assumed to be infinitely baffled. The term *infinitely baffled* means that the piezoelectric membrane of the piston transducer is restrained by an infinitely rigid wall [33,44]. Array transducers are not considered. More will be said about equipment in Chapter 6.

Scalar diffraction theory is assumed throughout. In particular, Rayleigh-Sommerfeld diffraction theory [24] forms the mathematical foundation for all the results derived. Furthermore, an infinitely baffled ideal transducer with infinite bandwidth or Dirac response is assumed in the theoretical development [10]. Homogeneity (as in the homogeneous wave equation of Eq. 1.1) and the first Born approximation, which implies no multiple scattering, are assumed [33]. In short, we assume ideal ultrasonic propagation in a uniform, isotropic, homogeneous and weakly scattering medium which supports only compressional waves [52]. These assumptions concerning ultrasonic diffraction and propagation are ubiquitous in the literature and should cause no alarm.

As was already mentioned numerous times, diffraction can be modeled as a time-varying filter. Practical time-varying filtering requires a joint time-frequency representation that is invertible *and* realizable with undue computational burden. Most joint time-frequency representations in the current literature can be conveniently classified as linear, bilinear/quadratic, or non-linear [28], and only a few meet the requirements just described. Indeed, non-linear representations are generally not invertible, and they were not considered. Bilinear representations were considered but abandoned because they are not easily invertible from a computational or algorithmic perspective.

Ultimately, the short-time Fourier transform was chosen because it is linear and invertible, well-documented [43], and easily interpreted. The short-time Fourier transform is viewed here as a tool, not a subject of study in and of itself. Hence, no tutorial material

on the subject is included. However, references to tutorial material and seminal works on the short-time Fourier transform and short-time Fourier techniques are included.

1.11 Document Organization and Preview

Recall the three theoretical goals of this research. The immediate goal is to derive a closed-form spatially averaged two-way diffraction correction for a focused piston transducer operating in pulsed-mode. The second goal is to unify previously disjoint and limited theory on spatially averaged diffraction corrections for piston transducers with coherent and generalized results. The third goal is to advance the scientific community's understanding of diffraction from a circular aperture, a ubiquitous and fundamental physical problem, with new results and insights. The document is organized to support achievement of these goals.

Chapter 2 reviews relevant literature and gives more background material. Chapter 3 is probably the most important chapter in the document for three reasons. First, it introduces and compares the arccos and Lommel diffraction formulations. Second, Chapter 3 establishes and verifies the Fourier equivalence of the arccos and Lommel diffraction formulations as an approximate Fourier transform pair for both focused and unfocused piston transducers. In short, the two diffraction formulations are connected in a new way thus providing fresh insight into diffraction from a circular aperture. Third, the new results and insights developed in Chapter 3 form the mathematical foundation for a unified theory of spatially averaged diffraction corrections for an infinitely baffled ultrasonic piston transducer operating in pulsed mode.

The unified theory is, in essence, a frequency-domain formalism for spatially averaged diffraction correction. As such, it is a frequency-domain alternative to the well-established time-domain or impulse-response formalism for spatially averaged diffraction correction [10, 52, 59]. The theory is based on the hypothesis that spatial averaging in the time domain is the same as spatial averaging in the frequency domain for any diffraction problem that can be modeled with the Rayleigh-Sommerfeld diffraction integral [24].

One-way spatially averaged diffraction effects are derived in Chapter 4. The insight gained in Chapter 3 leads to a new derivation of closed-form spatially averaged time-domain expressions based on the arccos diffraction formulation [10]. The derivation relates ultrasonic and optical diffraction in a unique way and thus provides a different perspective on diffraction from a circular aperture. In addition to this novel derivation, two new closed-form frequency-domain expressions are derived by spatially averaging the Lommel diffraction formulation.

Numerical results obtained from the time-domain and frequency-domain expressions are analyzed. The Fourier equivalence of the arccos and Lommel diffraction formulations for point receivers predicts that results obtained from the spatially averaged arccos-based results should be approximately equal to results obtained by inverse Fourier transforming the Lommel-based expressions; in short, the two formulations should be equivalent in a Fourier sense. This prediction is verified, and the success of the theory in the case of one-way diffraction with point and finite receivers is cause for optimism that theory will also hold for spatially averaged autoconvolution diffraction.

Spatial averaging of two-way diffraction is considered in Chapter 5. Specifically, a set of equations derived for optical diffraction is applied to the autoconvolution interpretation of two-way diffraction in ultrasound. The equations, which are based on Lommel's treatment of Fresnel diffraction from a circular aperture, are completely general in terms of area and focusing. Results obtained by numerical integration of the arccos diffraction formulation are compared to results obtained from the closed-form Lommel-based equations. As in the one-way case, the Fourier equivalence of the arccos and Lommel diffraction formulations predicts that the two sets of results should be equivalent in a Fourier sense. The prediction is verified.

Thus, Chapters 3–5 show that the Fourier equivalence of the arccos and Lommel diffraction formulations leads to a unified theory of spatially averaged diffraction corrections for an infinitely baffled ultrasonic piston transducer operating in pulsed mode. The theory is unified in the sense that the Fourier equivalence of the two formulations applies to both

one-way and two-way ultrasonic diffraction with piston receivers and reflecting disks of any size. The theory applies to unfocused and focused transducers and is used to derive closed-form results for unfocused one-way diffraction and focused and unfocused autoconvolution diffraction. Although the theory applies to spatially averaged one-way diffraction from a focused piston transducer, no closed-form results are derived for this case.

An aspect of the unified theory, autoconvolution diffraction, is experimentally investigated in Chapter 6. Diffraction corrections are implemented as time-varying filters, and ultrasonic data obtained from laboratory experiments are corrected using a short-time Fourier technique known as the *weighted overlap-add* method. The raw and corrected RF data are analyzed using spectral centroids, and B-mode images are reconstructed from the diffraction-corrected data.

Chapter 7 advances understanding of diffraction from a circular aperture and further unifies and validates the proposed spatially averaged diffraction theory by providing an original quantitative comparison of the mirror-image and autoconvolution interpretations of ultrasonic reflection imaging. Chapter 7 also presents a brief analysis of linear models of ultrasound. The last chapter states conclusions and makes recommendations for further study. It also compares the work presented in this document with work presented elsewhere and, thus, puts this research in perspective. Numerous computational issues arise, and these are discussed where appropriate. Finally, Appendix A contains two lemmas helpful in deriving one-way spatially averaged diffraction effects.

1.12 Criticism and Counter

Those familiar with this area of research may have two obvious and immediate objections to the unified theory proposed herein. The first objection is that the theory applies only to piston transducers which are the exception rather than the rule in ultrasound. The second objection is that the proposed unified theory will suffer from Gibb's phenomenon. These objections must be refuted.

The first objection is refuted with a short five point rebuttal. First, the hypothesis that spatial averaging is the same in the time and frequency domains is general because it holds for any transducer geometry. Second, closed-form spatially averaged solutions for piston transducer are worthwhile in and of themselves and in terms of the theoretical insight gained by deriving them. Third, results describing diffraction from piston transducers are qualitatively and quantitatively useful in describing diffraction from other transducers [3,12]. Fourth, the closed-form solutions derived herein have potential application in other areas, such as acoustics, electromagnetics, and non-destructive testing. Finally, piston transducers remain an economically viable product [46]. Thus, the proposed theory should be of theoretical and practical interest.

Refuting the second objection requires a little explanation. The proposed theory is a frequency-domain formalism based on the Lommel diffraction formulation and, as such, serves as an alternative to the well-established time-domain or impulse-response formalism based on the arccos diffraction formulation [10, 59]. Thus, we are primarily interested in frequency-domain results, particularly for spatially averaged diffraction effects.

To establish the theory, we assume impulse excitation of an infinitely baffled piston transducer that has a Dirac response (Section 1.10). To validate the theory, we inverse Fourier transform frequency-domain results and compare them with results computed using the impulse-response formalism. However, results computed with the impulse-response formalism have finite support in the time domain [10, 59]. Thus, an immediate criticism is that the proposed unified theory will suffer from Gibb's phenomenon [70] because an infinite bandwidth can never be adequately sampled. The criticism is valid for theoretically ideal transducers; however, real transducers are band-limited. Thus, the proposed theory will be of interest and value if it can be easily and accurately computed across bandwidths representative of real transducers. We will show that it can.

Chapter 2

Literature Review

This chapter reviews relevant literature on ultrasonic reflection imaging, diffraction from a circular aperture, the arccos and Lommel diffraction formulations, ultrasonic diffraction, short-time Fourier techniques, and time-varying filters. Literature on other topics, such as linear models of ultrasonic reflection imaging and the mirror-image and autoconvolution interpretations of ultrasound, will be considered in more detail in later chapters. A detailed discussion of how this research differs from previous research would make for difficult reading at this point. So a comparative literature review is postponed until Chapter 8 where one is combined with a discussion of results.

2.1 Ultrasonic Reflection Imaging

Descriptions of ultrasonic reflection imaging are available from many sources. Shung's treatment [57] includes sections on acoustic propagation and diagnostic methods. Macovski devotes two chapters to biomedical ultrasound in his text on medical imaging [40], one each on ultrasonic imaging theory and array transducers. Macovski's development is based on linear system theory and will appeal to electrical engineers, while Shung's is more relevant to mechanical engineers. Thijssen's presentation [61] on ultrasonic reflection imaging focuses on texture analysis and image processing but also provides a good introduction to basic

ultrasound. Finally, the chapter on ultrasound by Bamber and Tristram in [4] covers a broad range of ultrasound topics by emphasizing results and applications rather than mathematical development. Taken together, these four references provide a fairly thorough introduction to ultrasonic reflection imaging and simultaneously point the way to more advanced references.

2.2 Diffraction from a Circular Aperture

During his investigation of optical diffraction from a circular aperture in the late 1800's, E. Lommel developed a mathematical description of diffraction which is called here the *Lommel diffraction formulation* [68]; the description includes two celebrated functions which now bear Lommel's name. After its publication in 1885, the Lommel functions caught the attention of the mathematical community. Much of Lommel's original work was redone by Gray and Mathews [25] in the early 1920's, and Watson [63] investigated Lommel functions from a mathematical standpoint at about the same time as Gray and Mathews. In short, the mathematical community refined the Lommel diffraction formulation.

The ultrasound community appears to have become interested in the Lommel diffraction formulation in the late 1940's when Huntington, *et al.* [30] mentioned it in a paper on ultrasound delay lines and spatially averaged diffraction effects. Eight years later, Seki, *et al.* [56] published a paper on Lommel functions and diffraction effects in the case of monochromatic excitation of a piston transducer which they modeled as a circular aperture. In the early 1950's, the ultrasound community began developing pulse-echo techniques, and the monochromatic Lommel diffraction formulation was applied [47] in this new area of ultrasound for a number of years. What was needed, however, was a closed-form time-domain solution.

This solution was first derived by Oberhettinger in 1961 [44], and it is called here the *arccos diffraction formulation*. His derivation is an analytical one based on Bessel theory and the Laplace transform. A decade later, Stepanishen re-derived the arccos diffraction formulation using arguments from physics and geometry [59]. Both derivations model the

piston transducer as a circular aperture. In 1976, Penttinen and Luukkala [49] derived a focused version of the arccos diffraction formulation. Five years later, Arditi, *et al.* [2] extended Penttinen and Luukkala's work by describing transient fields of concave annular arrays. In that same year, Harris published a comprehensive review of the development of diffraction theory for a pulsed piston transducer [26]; his review includes the work of Oberhettinger, Stepanishen, and others. After the 1980's, research shifted from the arccos diffraction formulation toward spatially averaged diffraction corrections.

2.3 Spatially Averaged Diffraction Corrections

The ultrasound community has been researching spatially averaged diffraction corrections for piston transducers for over 50 years. The early work of Huntington, *et al.* has already been mentioned [30], and research in this area was pursued well into the 1950's. Williams derived one of the first closed-form diffraction corrections for ultrasound [66] in 1951. His derivation, based on one-way diffraction, applies to a receiver centered in the beam of a transmitter and having an area equal to that of the transmitter. In 1958, Bass [5] derived a closed-form result which was slightly more compact than the result derived by Williams.

There was also interest in spatially averaged diffraction effects outside of the ultrasound community. In the same year Williams published his closed-form diffraction correction, Wolf extended Lommel's treatment of Fresnel diffraction and derived expressions "... for the fraction of the total illumination present within certain regions in receiving planes near focus of spherical waves issuing from a circular aperture ... [68]." In short, Wolf used the Lommel diffraction formulation to find the spatially integrated intensity impinging on a disk coaxially located some distance z from the aperture. Wolf placed no restrictions on the area of the illuminated disk, and his results are applicable in spatially averaging both one-way and two-way diffraction effects in ultrasound (Section 1.5).

In the 1960's, the ultrasound community focused its attention on the arccos diffraction formulation and its theoretical and experimental validity as a convolution integral [26].

Work on spatially averaged diffraction corrections resumed in the 1970's when Williams published a paper [67] extending Bass's 1958 closed-form one-way diffraction correction to the case of a receiver having an area different from that of the transmitter. With computers becoming more accessible in the 1970's, researchers began to explore the validity and utility of the closed-form diffraction corrections derived in the previous two decades. For example, Khimunin [32] and Benson and Kiyohara [7] computed one-way diffraction corrections numerically and presented their results in tabular form. In fact, Benson and Kiyohara based their algorithms on Seki's 1956 paper.

In 1974, Rogers and Van Buren [54] simplified Bass's 1958 result by spatially integrating the Lommel diffraction formulation. Four years later, Rhyne [52] derived a closed-form one-way diffraction correction by spatially integrating the arccos diffraction formulation; he presented closed-form results in both the time and frequency domains. The results derived in [54] and [52] are limited to transmitters and receivers having equal areas. In 1981, Harris discussed spatially averaged diffraction corrections for the case of arbitrary velocity distributions [27]. Two years later, Kuc and Regula computed spatially integrated diffraction effects via numerical integration and investigated their impact on spectral estimates [37] based on ultrasonic data. It is critical to note that all the authors mentioned to this point invoked the mirror-image interpretation of two-way diffraction and applied one-way results to two-way diffraction.

In 1983 and 1984, Fink, *et al.* published papers on diffraction effects in pulse-echo measurements. Their work was new in that they addressed the autoconvolution interpretation of two-way diffraction and introduced spectral centroids as a measure of diffraction effects for focused and unfocused piston transducers [19,20]. In 1988, Cassereau, *et al.* [10] generalized Rhyne's one-way results [52] to transmitters and receivers having unequal areas. In the 1990's, Fink and Cardoso [9] derived a closed-form autoconvolution diffraction correction via spatial integration of a joint time-frequency representation. Finally, Chen *et al.* derived a spatially integrated mirror-image diffraction correction based on the Lommel diffraction formulation for the case of a focused piston transducer [11] in 1994.

2.4 Short-Time Fourier Techniques

A *stationary* signal is one with time-independent spectral content; a *non-stationary* signal is one with time-varying spectral content [53]. Traditional Fourier techniques characterize stationary signals in either the time domain or frequency domain; joint time-frequency information is not readily available in either domain. In general, traditional techniques are not well suited to determining the time-varying spectra of non-stationary signals. The theory of joint time-frequency representations was developed to extend the applicability of traditional Fourier techniques to non-stationary signals. Hlawatsch and Boudreaux-Bartels [28] wrote an excellent tutorial on joint time-frequency representations, and, as the authors point out, researchers in signal processing have concocted a plethora of joint time-frequency representations to analyze non-stationary signals.

The joint time-frequency representation that is most relevant to this research is the short-time Fourier transform (STFT), which Gabor proposed in 1946 [28]. Since then, the STFT has been used extensively in speech processing, and researchers in speech processing have developed many useful techniques based on the STFT. The chapter on short-time Fourier analysis in [51] is an older reference but remains one of the best introductions to the subject. More recent work on short-time Fourier transform and related techniques can be found in [43], Lim's 1988 text on advanced signal processing [38], and Oppenheim and Schaffer's text on signal processing [45].

Filtering of stationary signals is relatively straightforward because their spectral content is independent of time. On the other hand, filtering non-stationary signals is generally more difficult because their spectral content varies with time. This type of filtering requires time-varying filters which may be implemented using short-time Fourier techniques. Thus, these techniques find wide application in time-varying filtering.

Since time-varying filters have been researched at least since the 1950's, a great deal of discussion of the theory can be found in the signal processing literature. Bello characterized randomly time-variant linear channels [6] using time-varying filters, and his

work provides a good introduction to the topic. During the 1960's and 1970's, researchers in the speech community made great strides in time-variant filtering specifically because of the STFT and its linearity and invertibility. See Rabiner and Schafer [51], Lim [38], and Oppenheim and Schafer [45] and the numerous references contained therein for more details. The time-varying filtering done in this work is based on the weighted overlap-add method of short-time Fourier analysis/synthesis developed by Crochiere in the late 1970's while he was working with Bell Laboratories [15].

2.5 Short-Time Fourier Techniques in Ultrasound

Short-time Fourier techniques were applied in ultrasound by Salomonsson and Bjökman [55] and Claesson and Salomonsson [13]. In [55], the authors discuss a parametric time-varying network to separate attenuation and texture due to tissue, while in [13] the authors used the STFT to compensate for frequency- and depth-dependent attenuation in ultrasound signals. More recently, Daponte *et al.* [16] compared the STFT with other joint time-frequency representations when measuring the thickness of thin multilayer structures. Outside the biomedical community, Malik applied different joint time-frequency representations, including the STFT, to the problem of ultrasonic non-destructive testing [41].

Much of the ultrasound literature in which the STFT is applied is in the area of Doppler signal processing. A recent example is [62] in which the authors compare Doppler signal analysis techniques in the measurement of velocity, turbulence, and vortices; among the methods investigated was the STFT. Important work on short-time Fourier techniques in ultrasound was done by Altes and Faust [1] and Fink, *et al.* [19,20]. In [1], Altes and Faust used short-time Fourier analysis to provide a unified framework for ultrasonic diagnosis.

2.6 Chapter Summary

This chapter reviewed relevant literature on ultrasonic reflection imaging, diffraction from a circular aperture, the arccos and Lommel diffraction formulations, ultrasonic diffraction,

short-time Fourier techniques, and time-varying filters. A detailed discussion of how this research differs from previous research was not presented. A comparative literature review will be combined with a discussion of results in Chapter 8.

Chapter 3

The Arccos and Lommel Diffraction Formulations: An Approximate Fourier Transform Pair

This chapter establishes and verifies the Fourier equivalence of the arccos and Lommel diffraction formulations as an approximate Fourier transform pair. This relationship is important because it serves as the mathematical foundation for a proposed unified theory of spatially averaged diffraction corrections for ultrasonic piston transducers. Although the development is cast in terms of ultrasonic reflection imaging, the results are applicable to any physical problem involving diffraction from a circular aperture.

First, derivations of the arccos and Lommel diffraction formulations are outlined, and the two formulations are compared. The reader is referred to Oberhettinger [44], Papoulis [48, pp. 329–331], Stepanishen [59] and Harris [26] for complete details on the derivations. Next, the notion of an approximate Fourier transform is introduced, and the two diffraction formulations are unified by rigorously demonstrating their Fourier equivalence as

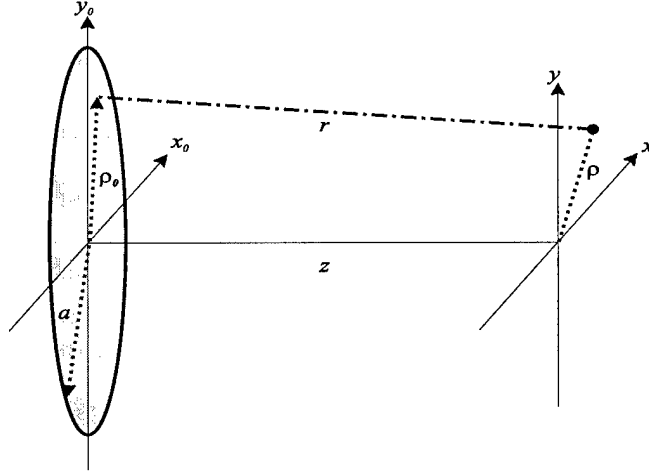


Figure 3.1: Piston transducer and fictitious point receiver.

an approximate Fourier transform pair. The Fourier equivalence is shown for both unfocused and focused piston transducers. The unfocused Lommel diffraction formulation is discussed first.

3.1 The Lommel Diffraction Formulation

Assuming monochromatic excitation of the unfocused transducer in Fig. 3.1, the disturbance $H_1(\rho, z, \omega)$ sensed by a fictitious point receiver located at some off-axis distance $\rho = \sqrt{x^2 + y^2}$ can be written

$$H_1(\rho, z, \omega) = \frac{1}{2\pi} \int_{\sigma_o} f(\sigma_o) \frac{e^{-jkr}}{r} d\sigma_o \quad (3.1)$$

where σ_o is the area of the transmitter (aperture) and r is the distance from an elemental area on the face of the transmitter to the point ρ . The subscript o denotes the source ($z = 0$) plane, while the subscript 1 denotes one-way propagation. The velocity distribution across the face of the transducer is $f(\sigma_o)$ which is unity due to the assumption of spatial uniformity.

The disturbance $H_1(\rho, z, \omega)$ is known in the literature on ultrasound as the *velocity-potential transfer function* [49]. The meaning of the term will become clear in the remainder of the chapter. For now, it is sufficient to note that the term *velocity-potential transfer function* implies the existence of a velocity-potential impulse response [59]. The fundamental relationship between an impulse response and its transfer function as an exact Fourier transform pair is well known, and the relevance of this relationship to this chapter is obvious.

As per convention, the time dependence of $H_1(\rho, z, \omega)$ on $e^{j\omega t}$ is implied. The spatial wave number k is related to temporal frequency ω via $k = \omega/c$. Thus, the dependence of velocity-potential transfer function $H_1(\rho, z, \omega)$ on ω is implicit in two ways.

Eq. 3.1 represents the Rayleigh-Sommerfeld diffraction integral with an obliquity factor of unity [24] and is applicable to a infinitely baffled flat-faced transducer of any geometry [33]. The Fresnel approximation in conjunction with the circular symmetry of a piston transducer allows the velocity-potential transfer function $H_1(\rho, z, \omega)$ in Eq. 3.1 to be estimated:

$$\hat{H}_1(\rho, z, \omega) = \frac{1}{z} e^{-jk(z + \frac{\rho^2}{2z})} \int_0^a e^{-jk\frac{\rho_o^2}{2z}} J_0\left(\frac{k\rho}{z}\rho_o\right) \rho_o d\rho_o \quad (3.2)$$

where $\rho_o = \sqrt{x_o^2 + y_o^2}$ is the off-axis distance at the source plane and $\rho = \sqrt{x^2 + y^2}$ is the off-axis distance at the observation plane [48, p. 330]. The "hat" notation (e. g. \hat{H}_1) signifies that the result is an estimate. Note that $\hat{H}_1(\rho, z, \omega)$ in Eq. 3.2 is closely related to Φ_P in [56] and is $g(\rho, z)$ in [48, Eq. (3-52), p. 330] multiplied by j/k . Eq. 3.2 is the classic description of diffraction from a circular aperture [48].

A prominent and familiar feature of Fresnel diffraction is its interpretation as a convolution involving a quadratic phase term [22, 48]. This feature is obscured in Eq. 3.2. However, if the singularity function,

$$p_a(\rho_o) = \begin{cases} 1, & \rho_o \leq a; \\ 0, & \rho_o > a \end{cases} \quad (3.3)$$

is introduced in the integrand of Eq. 3.2 and the upper limit of integration changed to ∞ ,

then Eq. 3.2 becomes

$$\widehat{H}_1(\rho, z, \omega) = \frac{1}{z} e^{-jk(z + \frac{\rho^2}{2z})} \int_0^\infty p_a(\rho_o) e^{-jk\frac{\rho_o^2}{2z}} J_0\left(\frac{k\rho}{z}\rho_o\right) \rho_o d\rho_o \quad (3.4)$$

which may be interpreted as the Hankel transform of the product of the singularity function $p_a(\rho_o)$ and a quadratic phase term. The convolution theorem for Hankel transforms allows Eq. 3.4 to be rewritten

$$\widehat{H}_1(\rho, z, \omega) = \frac{1}{k} e^{-jk(z + \frac{\rho^2}{2z})} \left[\frac{a}{\rho} J_1\left(\frac{ka\rho}{z}\right) * \frac{1}{j} e^{j\frac{k\rho^2}{2z}} \right] \quad (3.5)$$

where the convolution is with respect to $k\rho/z$. The familiar interpretation of Fresnel diffraction is made explicit in Eq. 3.5.

Eq. 3.2 can be integrated numerically, but a closed-form expression would simplify matters. Eq. 3.2 can be put in closed form via Lommel functions. The closed-form result is

$$\widehat{H}_1(\rho, z, \omega) = \frac{1}{k} e^{-j(kz + \frac{v^2}{2u} + \frac{u}{2})} [U_1(u, v) + jU_2(u, v)] \quad (3.6)$$

where the substitutions $u = ka^2/z$ and $v = ka\rho/z$ result in more compact notation. Eq. 3.6 is the Lommel diffraction formulation for an unfocused piston transducer and is easily programmed because of its closed form. The Lommel functions of two variables, $U_n(u, v)$, were defined in Eq. 1.2.

Seki, *et al.* [56] used a variant of Eq. 3.6 to calculate pressure as a function of depth z and off-axis distance ρ . The pressure p is related to the velocity-potential transfer function in the following manner,

$$p(\rho, z, \omega, t) = \pm \varrho \widehat{H}_1(\rho, z, \omega) \frac{\partial e^{\pm j\omega t}}{\partial t} \quad (3.7)$$

where ϱ is medium density. There is disagreement in the literature on sign convention, and \pm in Eq. 3.7 captures this disagreement. The convention with the positive sign was chosen in this work. Thus, pressure can be obtained from Eq. 3.6 by multiplying by $j\omega\varrho e^{j\omega t}$. Maximum pressures ($e^{j\omega t} = 1$) obtained from Eq. 3.6 are plotted in Fig. 3.2; the plots agree well with those in Seki's 1956 paper.

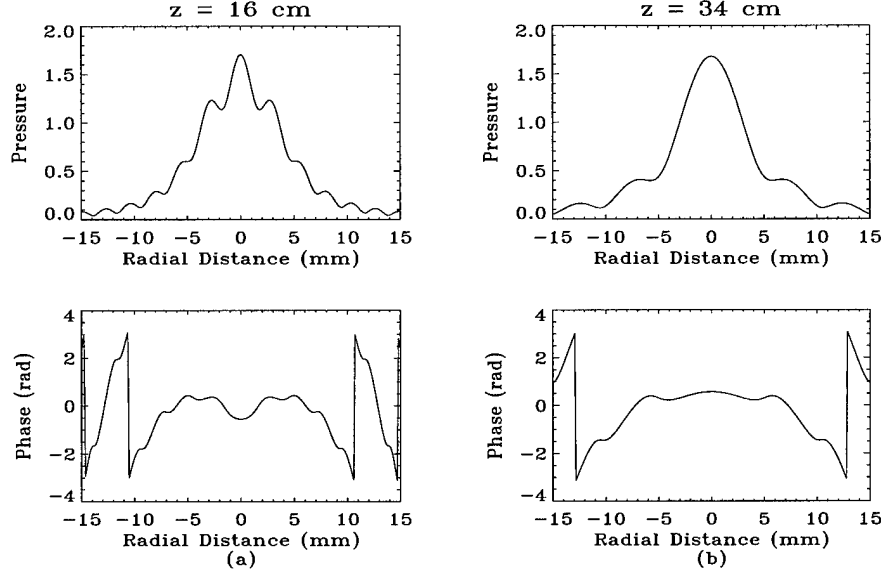


Figure 3.2: Pressures after Seki, *et al.* [56] via Eq. 3.6

Three computational issues deserve mention here. First, the choice of $U_n(u, v)$ or $V_n(u, v)$ in Eq. 1.4 depends on the ratio u/v . Second, $U_n(u, v)$ must be determined with sufficient accuracy; $n \geq 52$ was used in calculating the Bessel function $J_n(x)$ in Eq. 1.2 or Eq. 1.3. Calculating a Bessel function with this high an order may cause underflow on some machines. Third, on-axis ($\rho = 0$) values of Eq. 3.6 can be calculated via appropriate handling of the Lommel functions when $v = 0$ [63, p. 540], or they can be calculated from a separate formula which is easily derived by explicitly integrating Eq. 3.2 when $\rho = 0$. The latter method was used in our computations.

3.2 The Arccos Diffraction Formulation

The arccos diffraction formulation can be derived either analytically [44] or geometrically [59]. A modified version of Oberhettinger's analytical derivation [44] is outlined here because it leads to the realization that the arccos and Lommel diffraction formulations form an approximate Fourier transform pair. Assuming the unfocused transducer in Fig. 3.1 is

excited by an impulse, the velocity-potential impulse response $h_1(\rho, z, t)$ associated with the fictitious point receiver located at ρ can be written

$$\begin{aligned} h_1(\rho, z, t) &= \frac{1}{2\pi} \int_{-\infty}^{\infty} H_1(\rho, z, \omega) e^{j\omega t} d\omega, \\ &= \mathcal{F}^{-1} \{H_1(\rho, z, \omega)\} \end{aligned} \quad (3.8)$$

where \mathcal{F}^{-1} is the inverse Fourier transform. Thus, the velocity-potential impulse response in Eq. 3.8 is the inverse Fourier transform of velocity-potential transfer function $H_1(\rho, z, \omega)$ in Eq. 3.1. The term *velocity-potential impulse response* [59] comes from the fact that the pressure $p(\rho, z, t)$ can be written in terms of a convolution of the piston velocity $u(t)$ with the velocity potential impulse response $h_1(\rho, z, t)$,

$$p(\rho, z, t) = \varrho \frac{\partial}{\partial t} u(t) *_t h_1(\rho, z, t), \quad (3.9)$$

where the convolution is, as indicated, with respect to time. The meaning and significance of the terms *velocity-potential impulse response* and *velocity-potential transfer function* should now be clear.

With a transformation from rectangular to polar coordinates— $x = \rho \cos(\phi)$ and $y = \rho \sin(\phi)$ —the velocity potential transfer function $H_1(\rho, z, \omega)$ in Eq. 3.1 becomes

$$\begin{aligned} H_1(\rho, z, \omega) &= \int_{\phi_o=0}^{2\pi} \int_{\rho_o=0}^a \left\{ [\rho^2 + \rho_o^2 - 2\rho\rho_o \cos(\phi - \phi_o) + z^2]^{-1/2} \times \right. \\ &\quad \left. \exp[-jk(\rho^2 + \rho_o^2 - 2\rho\rho_o \cos(\phi - \phi_o) + z^2)] \right\} \rho_o d\rho_o d\phi_o. \end{aligned} \quad (3.10)$$

After several steps, Oberhettinger obtains exact expressions for $h_1(\rho, z, t)$ for two intervals. For $\rho < a$,

$$h_1(\rho, z, t) = \begin{cases} 0, & ct < z; \\ c, & z < ct < R'; \\ \frac{c}{\pi} \arccos \left[\frac{(ct)^2 - z^2 + \rho^2 - a^2}{2\rho((ct)^2 - z^2)^{1/2}} \right], & R' < ct < R; \\ 0, & ct > R, \end{cases} \quad (3.11)$$

and for $\rho > a$,

$$h_1(\rho, z, t) = \begin{cases} 0, & ct < R'; \\ \frac{c}{\pi} \arccos \left[\frac{(ct)^2 - z^2 + \rho^2 - a^2}{2\rho((ct)^2 - z^2)^{1/2}} \right], & R' < ct < R; \\ 0, & ct > R, \end{cases} \quad (3.12)$$

where $R' = \sqrt{z^2 + (a - \rho)^2}$ and $R = \sqrt{z^2 + (a + \rho)^2}$. Taken together, Eqs. 3.11 and 3.12 represent the arccos diffraction formulation. Interpretations of the arccos diffraction formulation at the spatial singularity $\rho = a$ can be found in the literature [10, 26, 59].

Note that Eq. 3.10 is the Rayleigh-Sommerfeld integral for diffraction from a piston transducer, and it led to the arccos diffraction formulation. On the other hand, Eq. 3.2 is the Fresnel approximation to Eq. 3.10, and Eq. 3.2 led to the Lommel diffraction formulation. Clearly, the arccos and Lommel diffraction formulations are closely related; we will explore this relationship more fully in the next section.

For now, we do well to describe the well-known behavior of the arccos diffraction formulation [59]. Fig. 3.3, which will be discussed in detail later, can be used as a visual aid. For a fixed depth z , the on-axis ($\rho = 0$) velocity-potential impulse response $h_1(\rho, z, t)$ is a rectangular pulse starting at $t = z/c$; its amplitude is c . As ρ increases, the start time of the pulse remains $t = z/c$ but the trailing edge of the pulse moves closer to $t = z/c$. Simultaneously, the fall time of the trailing edge increases, and the trajectory of the fall is governed by the arccos term in Eq. 3.11. In short, the pulse-like nature of the impulse response gradually decays with increasing ρ . For $\rho > a$, the impulse response no longer resembles a rectangular pulse, and its maximum value is something less than c . In addition, its start time is delayed, and the delay is function of ρ .

For a fixed off-axis distance ρ , the velocity potential impulse response $h_1(\rho, z, t)$ has the same general shape at any depth z but is compressed in time as z increases. The relationship can be quantified by expanding R' and R via binomial expansion, subtracting the smaller from the larger, and dividing for different values of z . The result is $h_1(\rho, z, t) = h_1(\rho, z, z_r t/z)$ for large z , where z_r is some appropriately chosen reference

plane [10]. Researchers in wavelet theory might find this an interesting physical problem since time scaling arises in a natural fashion.

3.3 Similarities and Differences

At this point, the Lommel and arccos diffraction formulations may be compared. Section 3.1 showed that the Lommel diffraction formulation is a monochromatic frequency-domain expression based on the Fresnel approximation to the Rayleigh-Sommerfeld integral of scalar diffraction theory. Hence, the derivation of Lommel diffraction formulation permits monochromatic diffraction from a circular aperture to be interpreted as a convolution involving a depth-dependent quadratic phase factor (Eq. 3.5). On the other hand, Section 3.2 showed that the arccos diffraction formulation is a set of polychromatic time-domain expressions based on the exact Rayleigh-Sommerfeld integral (with obliquity factor of unity). The arccos formulation permits impulsive diffraction from a circular aperture to be interpreted in terms of a depth-dependent time-scaling operation. Thus, the two formulations are similar in that they both describe diffraction from a circular aperture, but they differ in derivation (Fresnel vs. Rayleigh-Sommerfeld), realization (frequency vs. time domain) and interpretation (quadratic phase vs. time scaling).

As just mentioned, the Lommel diffraction formulation is based on the Fresnel approximation to the Rayleigh-Sommerfeld diffraction integral. The Fresnel region is often confused with the near field [22], and this confusion may lead to misinterpretation of our results. The following observations [22, 24, 48] are made to clear up the confusion and avoid misinterpretation.

The Rayleigh-Sommerfeld region [22] consists of all points in front of the transducer (aperture). The Fresnel region [48] is that portion of the Rayleigh-Sommerfeld region in which the Fresnel approximation,

$$25(a + \rho)^4 < \lambda z^3 = cz^3/f, \quad (3.13)$$

holds; λ is wavelength and f is frequency in Eq. 3.13. We note that the Fresnel region extends to infinity. The requirement in Eq. 3.13 is overly stringent, and it can be shown [24] that the Fresnel approximation is in fact valid for points nearer the transducer (aperture).

The Fraunhofer region, or far field, is that portion of the Fresnel region where the Fraunhofer approximation holds. Clearly, the Fresnel region contains the far field. We follow Gaskill [22] and regard the near field as the region lying between the transducer and the Fraunhofer region. Thus, the Lommel diffraction formulation and expressions based on it are valid in a good portion of the near field and all of the far field. In short, the Lommel diffraction formulation and expressions based on it are valid over a large portion of the half space in front of the transducer.

One final point concerning near field and far field must be made. The very notion of a near field and far field is predicated on *monochromatic* excitation (Section 1.2). Specifically, the demarcation between the near field and far field for a piston transducer is $Z = a^2/\lambda$. Recall $c = \lambda f$. Thus, if the excitation is pulsed, the notion of a near field and far field becomes complicated because each frequency in the pulse has an associated Z . For the purposes of this work, Z is simply the distance associated with the center frequency of the transducer.

3.4 Fourier Equivalence

The previous section taken at face value leads us to believe that the arccos and Lommel diffraction formulations are, for the most part, quite different. But when placed in the context of Fourier theory, the arccos and Lommel diffraction formulations are more similar than different. Specifically, their differences in terms of realization (time vs. frequency domain) and interpretation (quadratic phase vs. time scaling) become similarities in the context of Fourier theory. Furthermore, the derivation of the arccos diffraction formulation in Section 3.2 pointed to a close relationship between the arccos and Lommel diffraction formulations. Ultimately, their realization in conjugate domains (e. g. time vs. frequency)

indicates a possible relationship as an exact Fourier transform pair. This possible Fourier relationship is made more probable by the fact that the interpretation (time scaling vs. quadratic phase) of the two formulations is related to the Fourier explanation of time-scaling as convolution involving quadratic phase terms [48].

Although the derivations of the arccos and Lommel diffraction formulations pointed to a close relationship between the two formulations, their derivations (Rayleigh-Sommerfeld vs Fresnel) are quite different. Thus, they cannot form an exact Fourier transform pair. Despite this, they may form an "approximate" Fourier transform pair. This section introduces the notion of an approximate Fourier transform pair and rigorously demonstrates the Fourier equivalence of the arccos and Lommel diffraction formulations as an approximate Fourier transform pair.

Consider a function $f(t)$ that has an exact Fourier transform $F(\omega)$. Mathematically,

$$\mathcal{F}\{f(t)\} = F(\omega) \quad \text{and} \quad f(t) = \mathcal{F}^{-1}\{F(\omega)\}, \quad (3.14)$$

where \mathcal{F} and \mathcal{F}^{-1} represent the Fourier transform and inverse Fourier transform operations, respectively. Thus, $f(t)$ and $F(\omega)$ form a Fourier transform pair *exactly*. The notion of an *exact* Fourier time-frequency pair has been recognized in the literature on acoustics and ultrasound for decades [42, 49].

The notion of approximate Fourier transform pair is helpful when derivation of an exact Fourier transform pair is too difficult or when it is sufficient to have a rough idea of the Fourier relationship between $f(t)$ and $F(\omega)$. Mathematically,

$$\mathcal{F}\{f(t)\} \approx \hat{F}(\omega) \quad \text{and} \quad \hat{f}(t) \approx \mathcal{F}^{-1}\{\hat{F}(\omega)\}, \quad (3.15)$$

and it can be concluded that $f(t) \approx \hat{f}(t)$ where $\hat{f}(t)$ and $\hat{F}(\omega)$ are estimates of $f(t)$ and $F(\omega)$, respectively. Thus, $f(t)$ and $\hat{F}(\omega)$ form a Fourier transform pair *approximately*.

Consider again Eq. 3.8, the general form of the arccos diffraction formulation. In this equation, the velocity-potential impulse response $h_1(\rho, z, t)$ is the inverse Fourier

transform of the velocity-potential transfer function $H_1(\rho, z, \omega)$, and the exact form of $H_1(\rho, z, \omega)$ is unknown. However, a closed-form estimate or approximation is known, namely $\hat{H}_1(\rho, z, \omega)$. Thus, we may write

$$\hat{h}_1(\rho, z, t) = \mathcal{F}^{-1} \left\{ \hat{H}_1(\rho, z, \omega) \right\}. \quad (3.16)$$

where $\hat{h}_1(\rho, z, t)$ is an estimate of the impulse response predicted by the arccos diffraction formulation. In short, we claim that the arccos and Lommel diffraction formulations form an approximate Fourier transform pair:

$$\mathcal{F} \{ h_1(\rho, z, t) \} \approx \hat{H}_1(\rho, z, \omega). \quad (3.17)$$

The claim is verified numerically in the next section.

At this point, a discussion of Gibb's phenomenon [70] and its impact on this work is required. Under the stated assumptions (Section 1.10) and for practical geometries, impulse responses computed using the arccos diffraction formulation have compact support in the time domain; consequently, their Fourier transforms have infinite bandwidth in the frequency domain. In practice, the Lommel diffraction formulation can be sampled only over some finite bandwidth; consequently, impulse responses based on the Lommel diffraction formulation will suffer from Gibb's phenomenon.

As a result, we expect that Lommel-based results will fail to capture temporal discontinuities and will simultaneously exhibit ringing in the neighborhood of any temporal discontinuities. The degree of failure and extent of ringing are functions of the sampling rate; higher sampling rates will capture temporal discontinuities more faithfully but simultaneously introduce more ringing. In short, impulse responses based on the Lommel diffraction formulation and Eq. 3.16 can never show exact agreement with those based on the arccos diffraction formulation in Eqs. 3.11 and 3.12.

The complication just discussed is analogous to the complication encountered in filter design where the desired magnitude/phase response is required to have a discontinuity in the frequency domain [70]. In this case, the desired impulse response has infinite temporal

duration. In practice, however, the filter can be sampled only over some finite time duration. Consequently, the realizable filter will exhibit Gibb's phenomenon in the frequency domain. Filter designers resort to windowing to reduce the effects of Gibb's phenomenon. We will do the same when necessary.

3.5 Verification

The Fourier equivalence of the arccos and Lommel diffraction formulations as an approximate Fourier transform pair can be numerically verified by (i) computing discrete Fourier coefficients using Eq. 3.6, (ii) inverse Fourier transforming these coefficients, and (iii) comparing the results against results obtained from the arccos diffraction formulation in Eqs. 3.11 and Eq. 3.12. Computing discrete Fourier coefficients using Eq. 3.6 is justified by the fact that $k = \omega/c$.

The Lommel diffraction formulation (Eq. 3.6) was used in conjunction with Eq. 3.16 to estimate $h_1(\rho, z, t)$ for three off-axis positions at two depths: $z = 3$ cm and $z = 9$ cm. The speed of sound was set at $c = 1540$ m/s, and the diameter of the piston was set at $2a = 13$ mm. We reiterate that the transducer was assumed to have an infinitely broadband or Dirac response, and the excitation was assumed to be an impulse. The sampling frequency was set at $f_S = 36$ MHz; thus, the Nyquist frequency was 18 MHz.

Note the sampling rate is consistent with 2X oversampling of a real 2.25-MHz piston transducer with a cut-off frequency of 4.5 MHz. More will be said about real transducers at the end of this section. Furthermore, $Z = a^2/\lambda \approx 6$ cm for 2.25-MHz monochromatic excitation. Thus, the xy -planes at $z = 3$ cm and $z = 9$ cm can be considered in the near field and far field, respectively, for 2.25-MHz monochromatic excitation of a 13-mm diameter piston transducer.

The results are shown in Fig. 3.3. The off-axis positions are annotated in the figure. The impulse responses for a given ρ are plotted on the same time scale, referenced to $t = z/c$, to emphasize the depth-dependent time scaling discussed in Section 3.2. In all

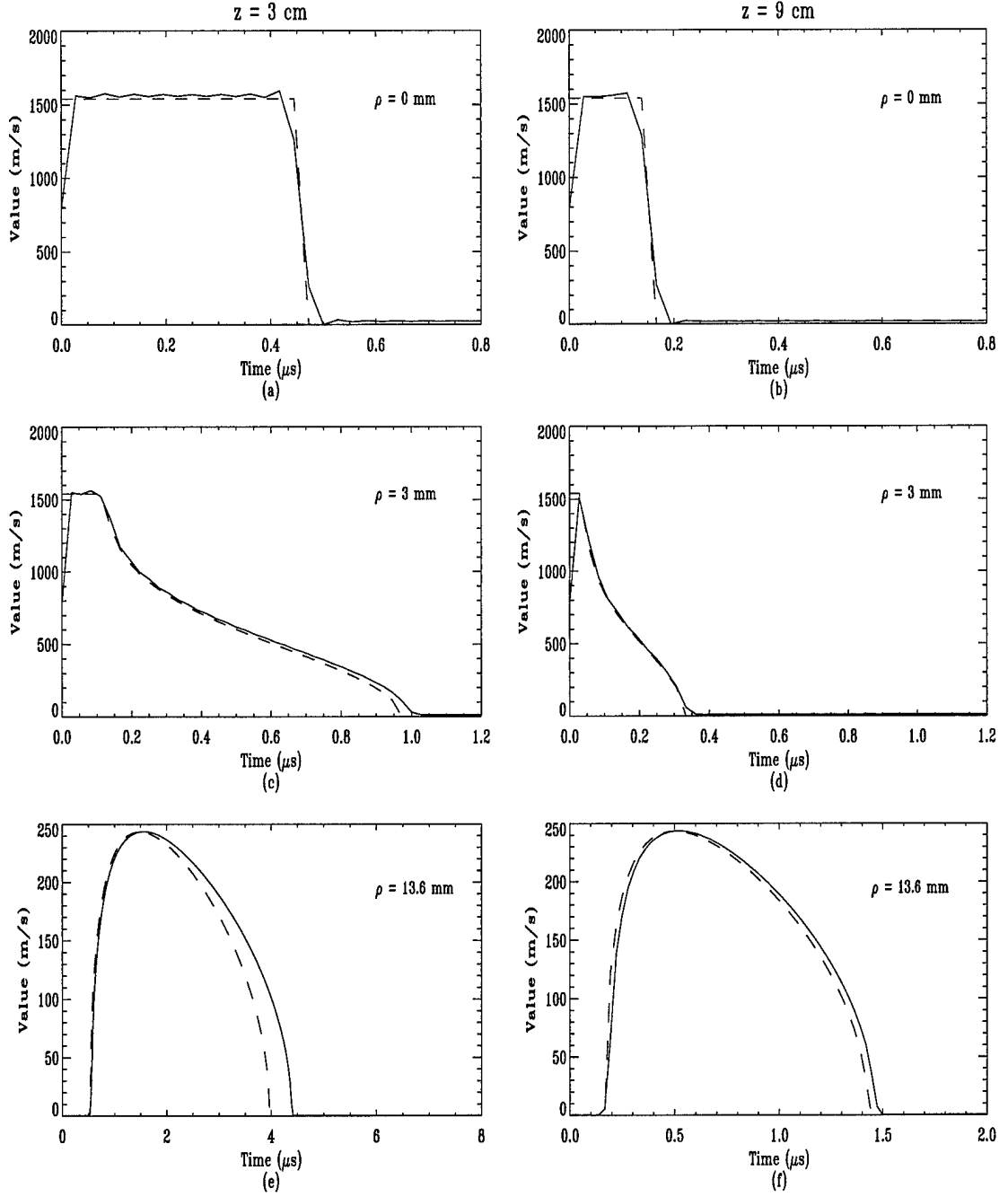


Figure 3.3: One-way point-receiver impulse responses for the Lommel (solid) and arccos (dashed) diffraction formulations.

figures where the two diffraction formulations are compared, Lommel-derived results are plotted with solid lines, while arccos-derived results are plotted with dashed lines. In this work, the arccos diffraction formulation is the gold standard against which the Lommel diffraction formulation is compared.

The plots in Figs. 3.3(a)-(b) show on-axis impulse responses. As was explained earlier, the on-axis impulse response for a piston transducer is a rectangular pulse of amplitude c that gets compressed in time with increasing depth z . The on-axis impulse responses computed with the Lommel diffraction formulation capture this behavior. As a result of Gibb's phenomenon, they do not capture the discontinuities at the beginning and end of each pulse. This was expected.

Since we did not expect exact agreement, we claim that the on-axis impulse responses computed using the Lommel diffraction formulation show satisfactory agreement with the arccos-based results. Figs. 3.3(c)-(d) show impulse responses for $\rho = 3$ mm. With the exception of discontinuities, the Lommel-based results are consistent with the results computed using the arccos diffraction formulation.

The plots in Figs 3.3(e)-(f) show impulse responses for $\rho = 13.6$ mm. Since $\rho > a$, each impulse response will have a maximum amplitude less than c and will start at some time later than $t = z/c$. This behavior is confirmed in the plots. Note that the Lommel diffraction formulation underestimates the time duration of the impulse response for $z = 3$ cm and overestimates it for $z = 9$ cm. This is not surprising because the Lommel diffraction formulation is based on the Fresnel approximation which becomes less accurate with increasing off-axis distance ρ and decreasing depth z .

Overall, the results show satisfactory agreement and confirm the validity of the Fourier equivalence of the arccos and Lommel diffraction formulations as an approximate Fourier transform pair. Clearly, the magnitude and phase responses (not shown) computed using the Lommel diffraction formulation capture the salient features of the arccos diffraction formulation. Thus, no discussion of frequency-domain results is included at this point. Frequency-domain results will be discussed in great detail in the chapters that follow.

3.6 Computational Considerations

Three computational issues have been discussed, and five new ones have yet to be considered. Because they will resurface, these considerations will be referred to as the *five general computational considerations*.

The Fourier transform of a real signal exhibits Hermitian symmetry. Thus, Fourier coefficients need be calculated for positive frequencies only; negative-frequency coefficients are computed by simply conjugating the positive ones. This computational benefit is negated by the second computation consideration, namely the fact that the Lommel diffraction formulation is ill-defined at $\omega = 0$. Because of this, a DC frequency coefficient cannot be calculated directly. This consideration is moot if the DC value is not required. If the DC value is required, it can be indirectly obtained by exploiting the fact that the arccos diffraction formulation is positive semi-definite.

Mathematically, $h_1(\rho, z, t) \geq 0$ for all ρ , z , and t of practical interest. In this work, discrete Fourier coefficients were calculated via Eq. 3.6 and inverse Fourier transformed with an FFT algorithm. The resulting samples were forced to be greater than or equal to zero. In short, $\hat{h}_1(\rho, z, t)$ was forced to be positive semi-definite. These two issues represent a trade-off inherent in any Lommel-based solution.

The third issue is the dimensionality of $k = 2\pi f/c$ in the denominator of Eq. 3.6. Since the coefficients calculated from the Lommel formulation are ultimately sent to an FFT algorithm, continuous or discrete frequencies may be used in the computation of k . Discrete frequencies, which are in a sense dimensionless, were used in our implementation. If the estimated impulse response is to be scaled to a maximum value of unity, the choice is immaterial.

Fourth, as explained earlier, estimated impulse responses will suffer from ringing due to Gibb's phenomenon. If desired, this artifact can be reduced with frequency-domain windowing; a window $w(f) = \text{sinc}(0.25\pi f/f_S)$ was used to produce the results shown in Fig. 3.3. The window is admittedly *ad hoc*, but it produced satisfactory results.

Finally, Eq. 3.6 gives no indication of how many frequency samples are required to estimate the arccos impulse response. For a given off-axis position ρ and sampling frequency $f_s = 0.5/\Delta t$, the minimum number of samples required can be computed via $(R - z)/(c\Delta t)$ or $(R - R')/(c\Delta t)$, whichever is appropriate. Note R and R' are defined in Eqs. 3.11 – 3.12.

A note of caution concludes this section. In comparing the two formulations numerically, accurate bookkeeping of sampling frequency, zero-padding, phase, and dimensional scaling is essential because results are being computed in conjugate domains.

3.7 The Focused Case

The results developed in the previous sections apply to unfocused piston transducers only. They can be extended to focused piston transducers by assuming that focusing introduces a time delay in Eq. 3.6. With this assumption, the Lommel diffraction formulation for a focused piston transducer of radius a is

$$\hat{H}_1(\rho, z, \omega) = \frac{\epsilon}{kz} e^{-j(kz + \frac{k\rho^2}{2z} + \frac{ka^2}{2\epsilon})} \left[U_1 \left(\frac{ka^2}{\epsilon}, \frac{k\rho}{z} \right) + j U_2 \left(\frac{ka^2}{\epsilon}, \frac{k\rho}{z} \right) \right], \quad (3.18)$$

where $1/\epsilon = 1/z - 1/R$, and R is the focal distance of the focused transducer [48]. In the limit as R approaches infinity, the focal length becomes infinite, and the transducer is considered unfocused. Thus, $\lim_{R \rightarrow \infty} \epsilon = z$, and Eq. 3.18 becomes Eq. 3.6 which is the Lommel diffraction formulation for unfocused piston transducers.

Eq. 3.18 was to estimate the velocity-potential impulse response for a focused piston transducer described by Penttinen and Luukkala [49]. The results are shown in Fig. 3.4, and they show good qualitative agreement with Fig. 3 in [49]. All computational issues discussed before apply to Eq. 3.18.

3.8 Chapter Summary

This chapter outlined the derivations of the arccos and Lommel diffraction formulations, two seminal descriptions of diffraction from a circular aperture. The two formulations

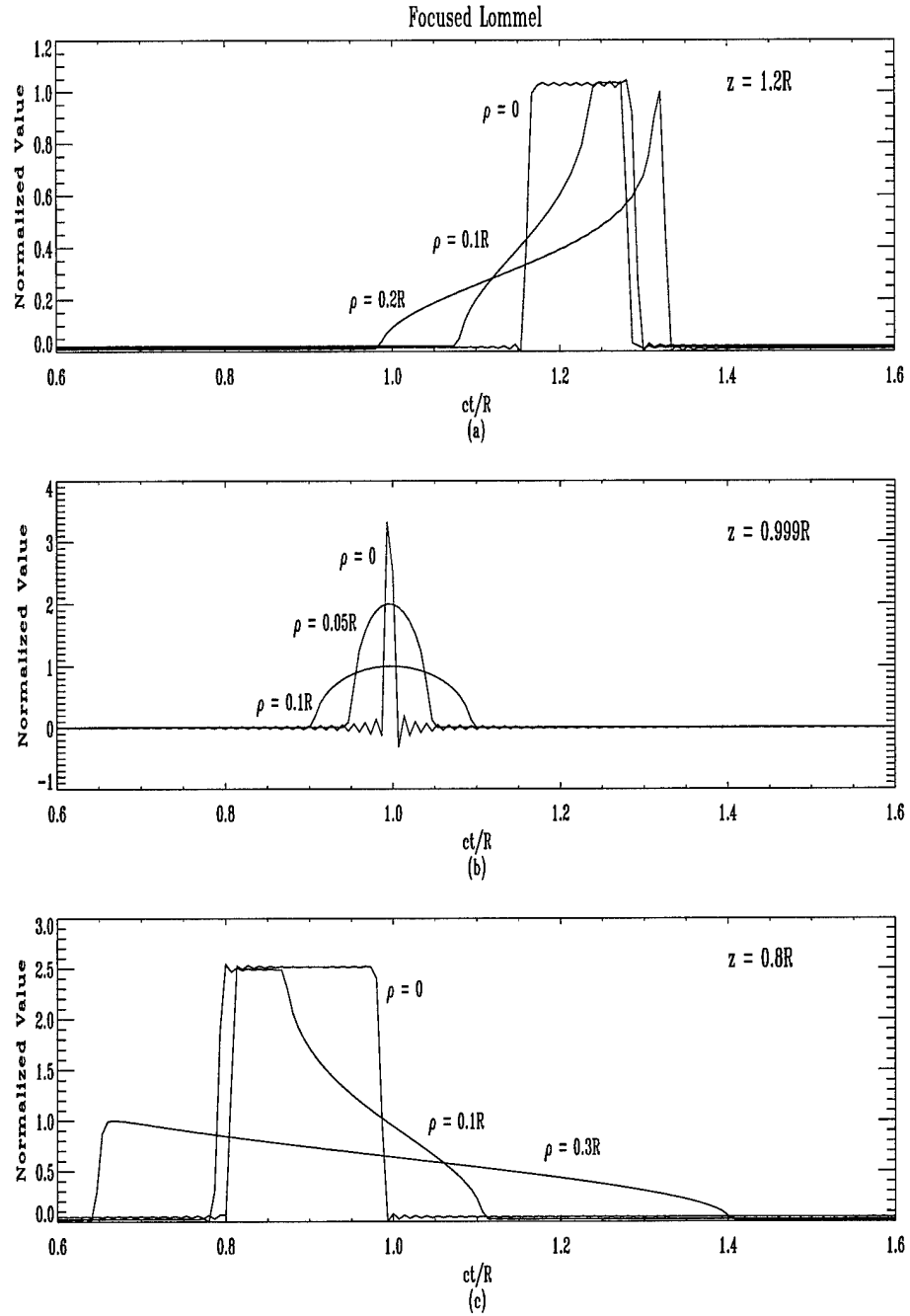


Figure 3.4: Focused impulse responses after Penttinen and Luukkala [49].

were compared and shown to be an approximate Fourier transform pair. Their connection was demonstrated numerically for both focused and unfocused piston transducers. Various computational issues were also discussed. The validity and utility of the theory developed in this chapter is demonstrated in the following chapters.

Chapter 4

Spatially Averaged One-Way Diffraction

The previous chapter established the Fourier equivalence of the arccos and Lommel diffraction formulations as an approximate Fourier transform pair. In this chapter, we exploit this Fourier equivalence in deriving a set of general closed-form frequency-domain expressions describing one-way diffraction for unfocused piston transmitters and receivers. The expressions are general in the sense that the area of the receiver may be less than, equal to, or greater than that of the transmitter. The frequency-domain expressions are derived within the framework of Lommel's treatment of Fresnel diffraction. Additionally, we present a new derivation of a closed-form time-domain description of one-way diffraction for a finite receiver [10]. Results obtained from the time-domain expressions will be compared with those obtained from the frequency-domain expressions. The time-domain expressions are derived first.

4.1 Spatially Averaged Arccos Diffraction Formulation

With c and $J_n(x)$ denoting the speed of sound and an n th-order Bessel function of the first kind, respectively, the velocity-potential impulse response for a unfocused piston transducer

and point receiver in integral form is

$$h_1(\rho, z, t) = \begin{cases} ac \int_0^\infty J_0(\tau \rho) J_1(\tau a) J_0\left(\tau \sqrt{(ct)^2 - z^2}\right) d\tau, & ct > z \\ 0, & ct < z \end{cases} \quad (4.1)$$

and in closed-form is given by Eqs. 3.11 and 3.12 which involve eponymous arccos terms. Eq. 4.1 assumes an unfocused piston transmitter of radius a and a *point* receiver as shown in Fig. 3.1.

As explained in the previous chapter, the integral form and closed form of the arccos diffraction formulation were derived analytically by Oberhettinger [44] in 1961. A decade later, Stepanishen derived the closed-form solution geometrically and interpreted it as an impulse response [59]; thus, the arccos diffraction formulation represents the velocity-potential impulse response for a the special case of a piston transducer and point receiver.

The spatially averaged impulse response in the case of a *finite* piston receiver of radius $b \leq a$ coaxially located some distance z in front of the piston transmitter is

$$\langle h_1(z, t) \rangle_b = \frac{1}{\pi b^2} \left[2\pi \int_0^b h_1(\rho, z, t) \rho d\rho, \right] \quad (4.2)$$

where $\langle \rangle_b$ denotes spatial integration and averaging over a disk of radius b . The situation is depicted in Fig. 4.1 Note the angular integration over 2π has already been completed in Eq. 4.2.

Recall the distinction between spatial averaging and spatial integration. The distinction is important because, as explained in Section 1.5, there is disagreement in the literature on the effects of integration and averaging. Williams states that the transducer output voltage is proportional to the spatially averaged pressure impinging on the transducer face [67], while Harris states that the output voltage is proportional to the spatially averaged pressure [27]. The factor of πb^2 is a small but important difference that becomes moot if results are normalized to a maximum value of unity.

Cassereau, *et al.* derived a remarkably simple expression for $\langle h_1(z, t) \rangle_b$ valid for any b by integrating the closed-form arccos diffraction formulation directly [10]. Their expression

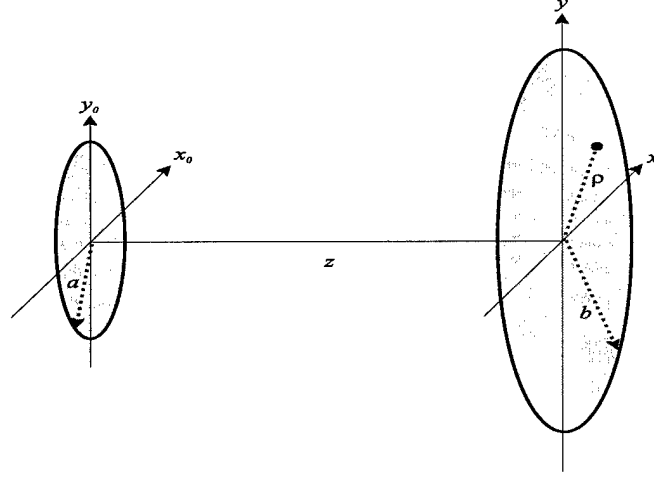


Figure 4.1: Piston transmitter and finite receiver.

can be obtained with an alternative derivation that provides new insight into diffraction from a circular aperture. The derivation consists of spatially averaging the integral form of the arccos diffraction formulation in Eq. 4.1 and interpreting the result as a Fourier-Bessel or Hankel transform,

$$\begin{aligned}
 \langle h_1(z, t) \rangle_b &= \frac{1}{\pi b^2} \left[2\pi a c \int_{\rho=0}^b \int_{\tau=0}^{\infty} J_0(\tau \rho) J_1(\tau a) J_0 \left(\tau \sqrt{(ct)^2 - z^2} \right) \rho d\rho d\tau \right], \\
 &= \frac{1}{\pi b^2} \left[2\pi a b c \int_{\tau=0}^{\infty} \tau^{-1} J_1(\tau b) J_1(\tau a) J_0 \left(\tau \sqrt{(ct)^2 - z^2} \right) d\tau \right], \\
 &= \frac{1}{\pi b^2} \left[2\pi a b c \int_{\tau=0}^{\infty} \tau^{-2} J_1(\tau b) J_1(\tau a) J_0(\gamma \tau) \tau d\tau \right], \\
 &= \frac{c}{\pi b^2} \mathcal{H} \left\{ 2\pi \tau^{-1} b J_1(\tau b) \tau^{-1} a J_1(\tau a) \right\}, \tag{4.3}
 \end{aligned}$$

where $\gamma = \sqrt{(ct)^2 - z^2}$, and \mathcal{H} denotes the Hankel transform with conjugate variables γ and τ . The convolution theorem for Hankel transforms allows Eq. 4.3 to be written

$$\langle h_1(z, t) \rangle_b = \frac{c}{\pi b^2} \text{cyl} \left(\frac{\gamma}{2b} \right) *_{\gamma} \text{cyl} \left(\frac{\gamma}{2a} \right), \tag{4.4}$$

where $\text{cyl}(r)$ is defined in [22]. Gaskill derived a closed-form solution to Eq. 4.4 via graphical

convolution. With $\alpha = (\gamma^2 + a^2 - b^2)/(2\gamma a)$ and $\beta = (\gamma^2 + b^2 - a^2)/(2\gamma b)$, the solution is

$$\langle h_1(z, t) \rangle_b = \begin{cases} c, & \gamma < a - b; \\ \frac{ca^2}{\pi b^2} \left[\cos^{-1}(\alpha) - \alpha \sqrt{1 - \alpha^2} \right] + \\ \quad \frac{c}{\pi} \left[\cos^{-1}(\beta) - \beta \sqrt{1 - \beta^2} \right], & a - b \leq \gamma \leq a + b; \\ 0, & \gamma > a + b. \end{cases} \quad (4.5)$$

With the exception of a multiplicative constant, Eq. 4.5 is similar to a result derived by Cassereau, *et al.* [10]. The time scaling inherent in the limits of Eq. 3.11 and Eq. 3.12 is also inherent in the limits of Eq. 4.5. That is, $\langle h_1(z, t) \rangle_b$ is compressed in time as z increases.

Though derived under the assumption $b \leq a$, Eq. 4.4 is in fact completely general. If $b > a$, the two variables can simply be interchanged in Eq. 4.5. When $a = b$, Eq. 4.5 can be easily manipulated into the closed-form solution derived by Rhyne [52].

Additional insight can be gained by considering Eqs. 4.4–4.5. First, the generality of Eq. 4.5 is due to the commutativity of convolution in Eq. 4.4 which, in this context, may be interpreted as a mathematical manifestation of Helmholtz’s reciprocity theorem [34]. Second, Eq. 4.5 is well known in optics. Gaskill calls it the *cylinder-function cross correlation* [22, pp. 302–304], while Bracewell gives the name *chat* function [8, pp. 187–192] to the special case that results when $b = a$. Bracewell coined this term because the shape of the graph of Eq. 4.5 as a function of γ for $a = b$ resembles a Chinese farmer’s hat. Thus, insights and results developed in optics for Eq. 4.5 may benefit researchers in ultrasound.

Finally, the graph that results from plotting Eq. 4.5 as a function of time t for $b = a$ is strikingly similar to the celebrated *brachistochrone* [14, 23]; compare Fig. 4.2 and Figs. 4.5(a)–(b). Indeed, the form of Eq. 4.5 for the case $b = a$ is similar to the equation for the brachistochrone; Eq. 4.5 for the case $b = a$ is

$$\langle h_1(z, t) \rangle_a = \frac{2c}{\pi} \left[\arccos\left(\frac{\gamma}{2a}\right) - \frac{\gamma}{2a} \sqrt{1 - \frac{\gamma^2}{4a^2}} \right], \quad (4.6)$$

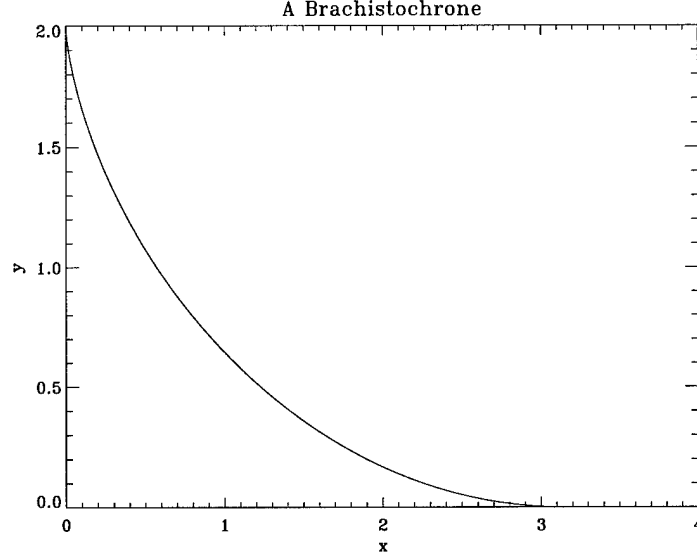


Figure 4.2: A brachistochrone.

and, with the parameterization

$$x = r(\theta - \sin \theta) \quad \text{and} \quad (4.7a)$$

$$y = r(1 + \cos \theta), \quad (4.7b)$$

the equation for the brachistochrone is

$$x = r \arccos \left(\frac{y-r}{r} \right) - r \sqrt{1 - \left(\frac{y-r}{r} \right)^2}. \quad (4.8)$$

Note the similarity between Eq. 4.6 and Eq. 4.8. The graphical and functional similarities just noted are not surprising when one considers the physical origin of and mathematical solution to the brachistochrone problem and diffraction problem. Specifically, both problems can be formulated in terms of Hamilton's physical principle of least action [23]. Thus, both are mathematically amenable to solution via the calculus of variations. More rigorous comparison of these two problems may lead to deeper understanding of diffraction from piston transducers and transducers involving other geometries.

4.2 Spatially Averaged Lommel Diffraction Formulation

A set of closed-form *frequency-domain* expressions describing the spatially averaged one-way diffraction effects for the case of a finite receiver can be obtained by spatially integrating the Lommel diffraction formulation in Eq. 3.6. A spatially averaged closed-form expression will be derived for each of three cases of the radius of the piston receiver: a piston receiver with radius (i) $b < a$, (ii) $b = a$, and (iii) $b > a$. In each case, the transmitter, a piston transducer with radius a , and the receiver are coaxial and separated by a distance z .

Spatial integration of the Lommel diffraction formulation for each case is facilitated by functions defined in Eqs. 1.2–1.10. and mathematical lemmas in [68] and in Appendix A of this document. Spatially integrating and averaging Eq. 3.6 yields

$$\langle \hat{H}_1(z, \omega) \rangle_b = \frac{1}{\pi b^2} \left[2\pi \int_0^b \hat{H}_1(\rho, z, \omega) \rho d\rho \right] \quad (4.9)$$

Note the angular integration from 0 to 2π has been completed.

The integral in Eq. 4.9 can be solved for $b < a$ with the help of results derived by Wolf [68]. Specifically, the $U_n(u, v)$ functions in the integrand are expanded in terms of $V_n(u, v)$ via Eq. 1.4 and integrated using Lemma 9 in [68, p. 548]. The intermediate result is simplified by noting $W_1(u, v) - W_3(u, v) = Y_1(u, v)$ and $2W_2(u, v) = Y_2(u, v)$. With $v_b = kab/z$ and $u = ka^2/z$, the first spatially averaged expression is

$$\langle \hat{H}_1(z, \omega) \rangle_{b < a} = -\frac{2z}{(kb)^2} e^{-j(kz + \frac{u}{2})} \left\{ j \frac{v_b^2}{2u} e^{j\frac{u}{2}} + e^{-j\frac{v_b^2}{2u}} [Y_2(u, v_b) - jY_1(u, v_b)] \right\}. \quad (4.10)$$

Eq. 4.10 is new in the literature on diffraction from an unfocused piston transducer. It is, however, a burdensome expression to compute. Nonetheless, the Y_n functions are highly convergent, and the computational burden may be eased by recursion relations [69].

In the second case, $b = a$, $v_b = u$, and Eq. 4.9 succumbs to a welcome simplification that is a special case of Eq. 4.10. Specifically, $Y_1(u, u) = 0.5uJ_0(u)$ and $Y_2(u, u) = 0.5uJ_1(u)$; thus the expression for the spatially averaged one-way diffraction effects when $b = a$ is

$$\langle \hat{H}_1(z, \omega) \rangle_{b=a} = -\frac{2z}{(kb)^2} e^{-j(kz + \frac{u}{2})} \times \left\{ j \frac{u}{2} e^{j\frac{u}{2}} + e^{-j\frac{u}{2}} \left[\frac{u}{2} J_1(u) - j \frac{u}{2} J_0(u) \right] \right\}. \quad (4.11)$$

Unlike Eq. 4.10, Eq. 4.11 is relatively easy to compute. We remark here that Eq. 4.11 is, with the exception of a multiplicative constant, the same as the result derived by Rogers and Van Buren [54]. Furthermore, Chen, *et al.* derived a similar result for the pressure transfer function of a *focused* transducer; recall pressure and velocity-potential transfer functions differ by the factor $\rho j\omega$ for monochromatic excitation.

The last case when $b > a$ is particularly challenging. The result is derived by splitting the range of integration in Eq. 4.9 into the two intervals: $0 \leq \rho \leq a$ and $a < \rho \leq b$. The problem becomes

$$\begin{aligned} \langle \hat{H}_1(z, \omega) \rangle_b = & -\frac{2z}{(kb)^2} e^{-j(kz + \frac{u}{2})} \times \\ & \left\{ j\frac{u}{2} e^{j\frac{u}{2}} + e^{-j\frac{u}{2}} \left[\frac{u}{2} J_1(u) - j\frac{u}{2} J_0(u) \right] \right\} + \\ & \frac{1}{\pi b^2} \left[2\pi \int_a^b \hat{H}_1(\rho, z, \omega) \rho d\rho \right]. \end{aligned} \quad (4.12)$$

With $u = ka^2/z$, $v = ka\rho/z$, and $v_b = kab/z$, the integral in Eq. 4.12 is

$$\langle \hat{H}_1(z, \omega) \rangle_{u < v \leq v_b} = \frac{2z}{u(kb)^2} e^{-j(kz + \frac{u}{2})} \int_u^{v_b} [U_1(u, v) + jU_2(u, v)] e^{-j\frac{v^2}{2u}} v dv. \quad (4.13)$$

Application of Lemma 2 in Appendix A and some algebra yields

$$\begin{aligned} \langle \hat{H}_1(z, \omega) \rangle_{u < v \leq v_b} = & \frac{2z}{(kb)^2} e^{-j(kz + \frac{u}{2})} \times \\ & \left\{ e^{-j\frac{u}{2}} [2Z_2(u, u) - jZ_1(u, u) + jZ_3(u, u)] + \right. \\ & \left. e^{-j\frac{v_b^2}{2u}} [jZ_1(u, v_b) - jZ_3(u, v_b) - 2Z_2(u, v_b)] \right\}, \end{aligned} \quad (4.14)$$

which may be simplified because $Z_1(u, v) - Z_3(u, v) = X_1(u, v)$ and $2Z_2(u, v) = X_2(u, v)$.

Thus, Eq. 4.14 becomes

$$\begin{aligned} \langle \hat{H}_1(z, \omega) \rangle_{u < v \leq v_b} = & \frac{2z}{(kb)^2} e^{-j(kz + \frac{u}{2})} \times \\ & \left\{ e^{-j\frac{u}{2}} [X_2(u, u) - jX_1(u, u)] + \right. \\ & \left. e^{-j\frac{v_b^2}{2u}} [jX_1(u, v_b) - X_2(u, v_b)] \right\}. \end{aligned} \quad (4.15)$$

Now, $X_1(u, u) = 0.5uJ_0(u)$ and $X_2(u, u) = 0.5uJ_1(u)$, so

$$\begin{aligned} \langle \hat{H}_1(z, \omega) \rangle_{u < v \leq v_b} &= \frac{2z}{(kb)^2} e^{-j(kz + \frac{u}{2})} \times \\ &\quad \left\{ e^{-j\frac{u}{2}} \left[\frac{u}{2} J_1(u) - j\frac{u}{2} J_0(u) \right] + \right. \\ &\quad \left. e^{-j\frac{v_b^2}{2u}} [jX_1(u, v_b) - X_2(u, v_b)] \right\}. \end{aligned} \quad (4.16)$$

Substitution of Eq. 4.16 into Eq. 4.12 and a little algebra produces the third closed-form frequency-domain expression:

$$\langle \hat{H}_1(z, \omega) \rangle_{b > a} = -\frac{2z}{(kb)^2} e^{-j(kz + \frac{u}{2})} \left\{ j\frac{u}{2} e^{j\frac{u}{2}} + e^{-j\frac{v_b^2}{2u}} [X_2(u, v_b) - jX_1(u, v_b)] \right\}. \quad (4.17)$$

Like Eq. 4.10, Eq. 4.17 is new in the literature on diffraction from an unfocused piston transducer. It is, however, a burdensome expression to compute. Nonetheless, the X_n functions are highly convergent, and the burden of computing them may be eased by recursion relations [69]. Finally, we note the symmetry between Eq. 4.17 and Eq. 4.10.

The results just derived are compiled here for convenience:

$$\begin{aligned} \langle \hat{H}_1(z, \omega) \rangle_b &= -\frac{2z}{(kb)^2} e^{-j(kz + \frac{u}{2})} \times \\ &\quad \begin{cases} \left(j\frac{v_b^2}{2u} e^{j\frac{u}{2}} + e^{-j\frac{v_b^2}{2u}} [Y_2(u, v_b) - jY_1(u, v_b)] \right), & b < a; \\ \left(j\frac{u}{2} e^{j\frac{u}{2}} + e^{-j\frac{u}{2}} \left[\frac{u}{2} J_1(u) - j\frac{u}{2} J_0(u) \right] \right), & b = a; \\ \left(j\frac{u}{2} e^{j\frac{u}{2}} + e^{-j\frac{v_b^2}{2u}} [X_2(u, v_b) - jX_1(u, v_b)] \right), & b > a. \end{cases} \end{aligned} \quad (4.18)$$

4.3 Fourier Equivalence Extended to Spatially Averaged One-Way Diffraction

The Fourier equivalence of the arccos and Lommel diffraction formulations can be extended to spatially integrated one-way diffraction. Spatially integrating Eq. 3.8 and subsequently inverse Fourier transforming the result yields

$$\langle h_1(z, t) \rangle_b = \mathcal{F}^{-1} \{ \langle H_1(z, \omega) \rangle_b \} \quad (4.19)$$

and, since $\langle H_1(z, \omega) \rangle_b \approx \langle \hat{H}_1(z, \omega) \rangle_b$, we may also write

$$\langle h_1(z, t) \rangle_b \approx \mathcal{F}^{-1} \left\{ \langle \hat{H}_1(z, \omega) \rangle_b \right\}, \quad (4.20a)$$

$$\langle \hat{h}_1(z, t) \rangle_b = \mathcal{F}^{-1} \left\{ \langle \hat{H}_1(z, \omega) \rangle_b \right\}, \quad \text{and} \quad (4.20b)$$

$$\langle h_1(z, t) \rangle_b \approx \langle \hat{h}_1(z, t) \rangle_b. \quad (4.20c)$$

Theoretically, substituting $k = \omega/c$ in the Eq. 4.18 should allow estimation of the Fourier coefficients of the spatially integrated arccos impulse response for any b . These coefficients can then be inverse Fourier transformed to estimate the spatially averaged arccos impulse response. This reasoning is simply an extension of the Fourier equivalence of the Lommel and arccos diffraction formulations for a point receiver developed in Chapter 3.

Some discussion is required before computing and comparing spatially averaged impulse responses. First, Eq. 4.5 is a closed-form time-domain expression for the spatially averaged arccos diffraction formulation. It will serve as the gold standard in this research.

Second, impulse responses computed using Eq. 4.5 will have compact support in the time domain; consequently, their Fourier transforms have infinite bandwidth in the frequency domain. Like the Lommel diffraction formulation (Eq. 3.6), Eq. 4.18 must be sampled over some finite bandwidth. Consequently, impulse responses based on Eq. 4.18 will suffer from Gibb's phenomenon, and the comments made about impulse responses based on the Lommel diffraction formulation (Sections 3.4–3.5) apply here. Nonetheless, useful results will be obtained.

4.4 Verification

The Fourier equivalence of the arccos and Lommel diffraction formulations as an approximate Fourier transform pair predicts that Eq. 4.18 and Eq. 4.20 may be used to estimate the one-way spatially averaged impulse response associated with the arccos diffraction formulation. Eq. 4.18 was used in this fashion and the results obtained plotted against results computed using the spatially averaged arccos diffraction formulation of Eq. 4.5. Fig. 4.3

through Fig. 4.7 show the plots. Five values of b noted in the figures were used. Only Fig. 4.5 is discussed in detail. Concise comments pertaining to Figs. 4.3–4.4 and Figs. 4.6–4.7 follow the discussion of Fig 4.5.

Figs. 4.5(a)–(b) show spatially integrated one-way impulse responses estimated via Eq. 4.11 (solid lines) and spatially integrated one-way impulse responses calculated by using Eq. 4.5 (dashed lines). The impulse responses were calculated for $b = a$ at two depths: $z = 3$ cm and $z = 9$. The speed of sound was set at $c = 1540$ m/s, and the diameter of the piston was set at $2a = 13$ mm. The transducer was assumed to have an infinitely broadband response, and the excitation was assumed to be an impulse. The sampling frequency was set at $f_s = 36$ MHz; thus, the Nyquist frequency was 18 MHz.

With the exception of discontinuities, the impulse responses based on Eq. 4.11 are consistent with the results computed using Eq. 4.5 and results computed by Kuc and Regula [37]. The five general computational issues discussed in Section 3.6 apply here; the window $w(f)$ was used in computing the Lommel-based impulse responses. Thus, ringing due to Gibb’s phenomenon is reduced in the plots, and the impulse responses show satisfactory agreement. It is also important to reiterate the ease with which Eq. 4.11 can be computed

Figs. 4.5(b)–(c) and Figs. 4.5(d)–(e) show the squared magnitude responses (dB) and the phase responses associated with the impulse responses in Fig. 4.5(a) and Fig. 4.5(b), respectively. Taking an optimistic point of view, we can say the magnitude responses show satisfactory agreement, particularly at the lower frequencies. Indeed, better agreement can be had at higher frequencies if the sampling frequency is increased, but the cost is more samples. The dotted lines shown in the magnitude plots will be discussed later.

The phase responses do not agree as favorably. This is not surprising when one considers the physical origins of the results being compared. Specifically, the arccos-derived results are based on the Rayleigh-Sommerfeld diffraction integral, while the Lommel-derived results are based on the Fresnel diffraction integral. Hence, the two diffraction integrals differ primarily in terms of their phase [22]. This in conjunction with Gibb’s phenomenon helps

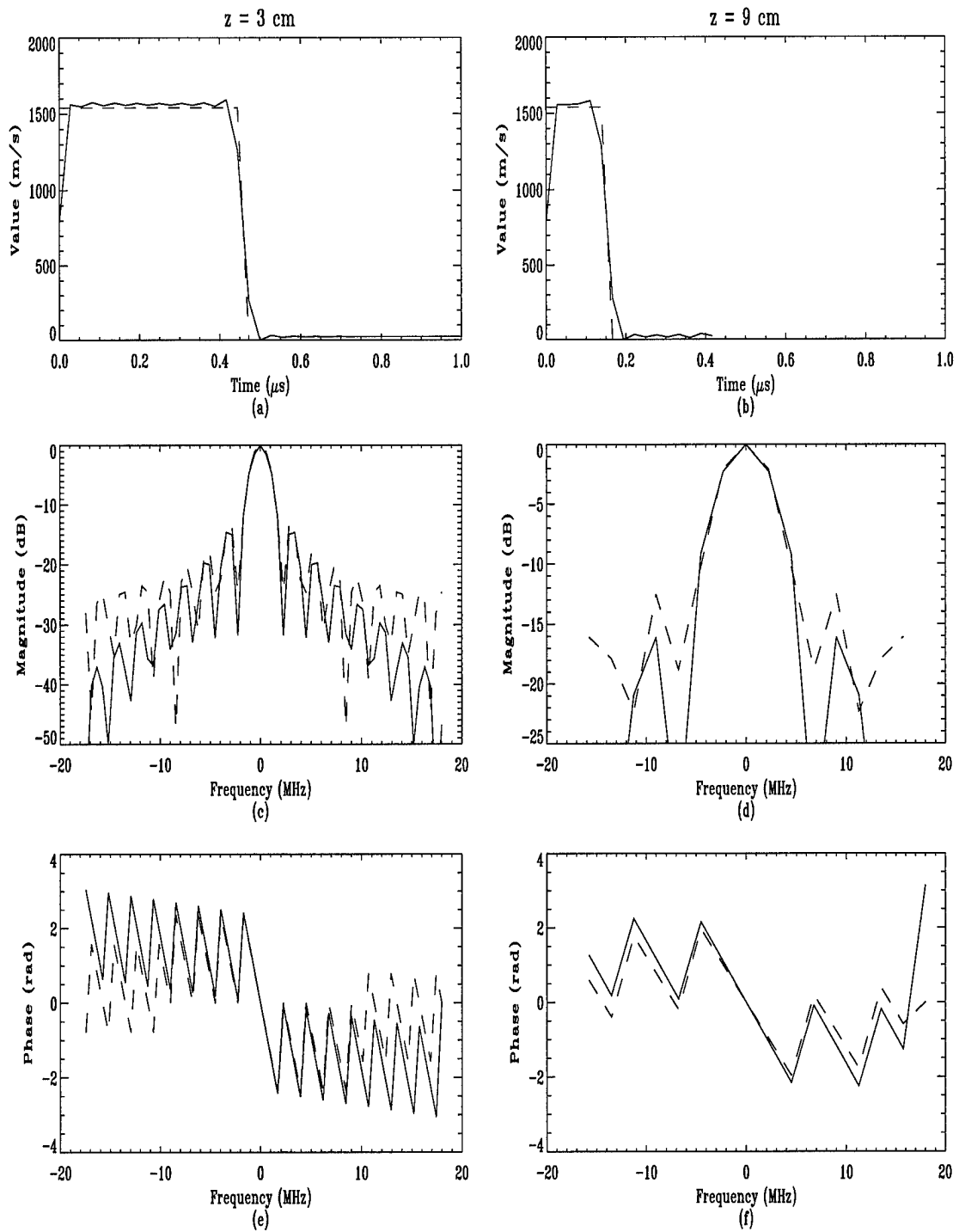


Figure 4.3: One-way spatially averaged impulse responses for the Lommel (solid) and arccos (dashed) diffraction formulations: $b = a/1000$.

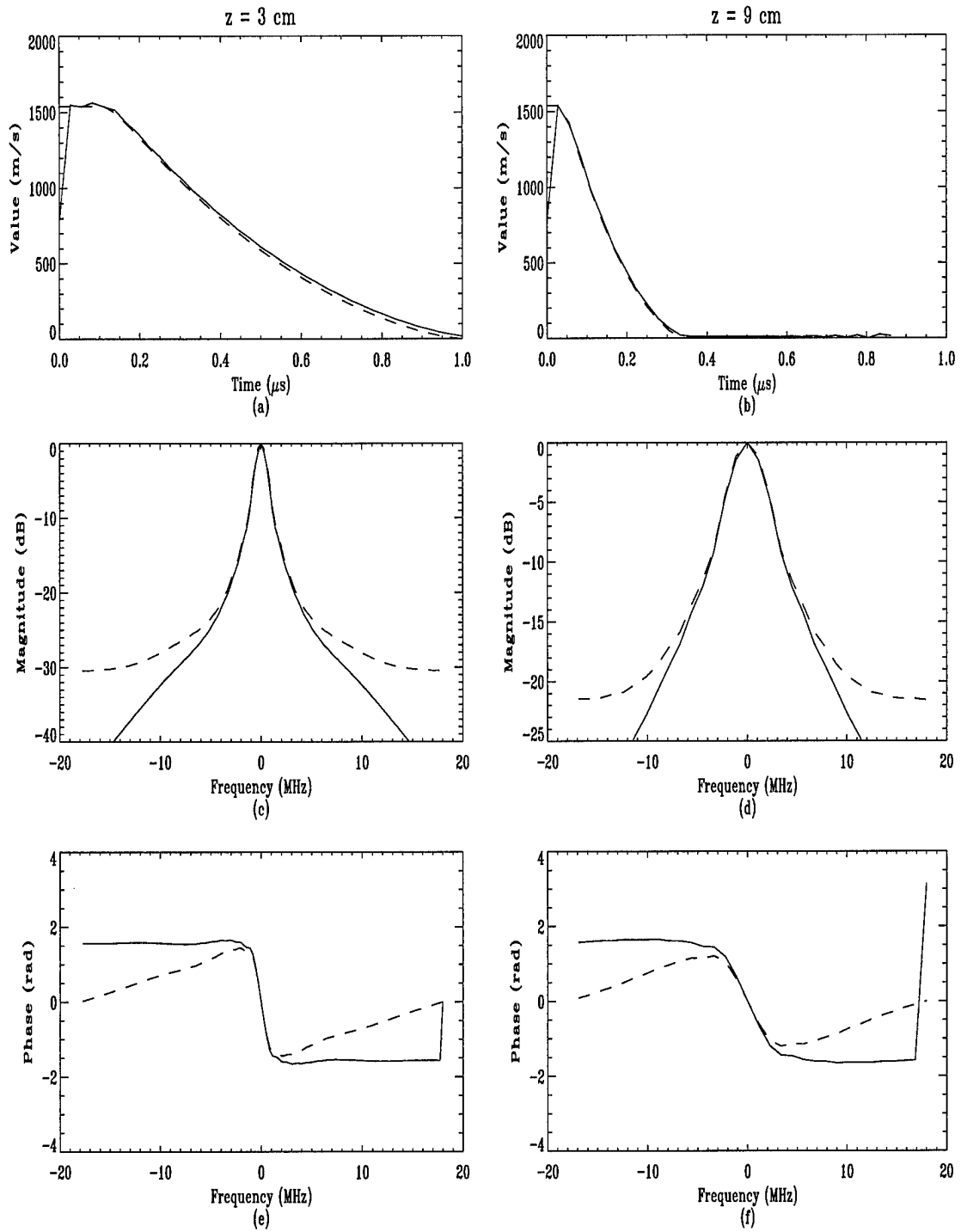


Figure 4.4: One-way spatially averaged impulse responses for the Lommel (solid) and arccos (dashed) diffraction formulations: $b = a/2$.

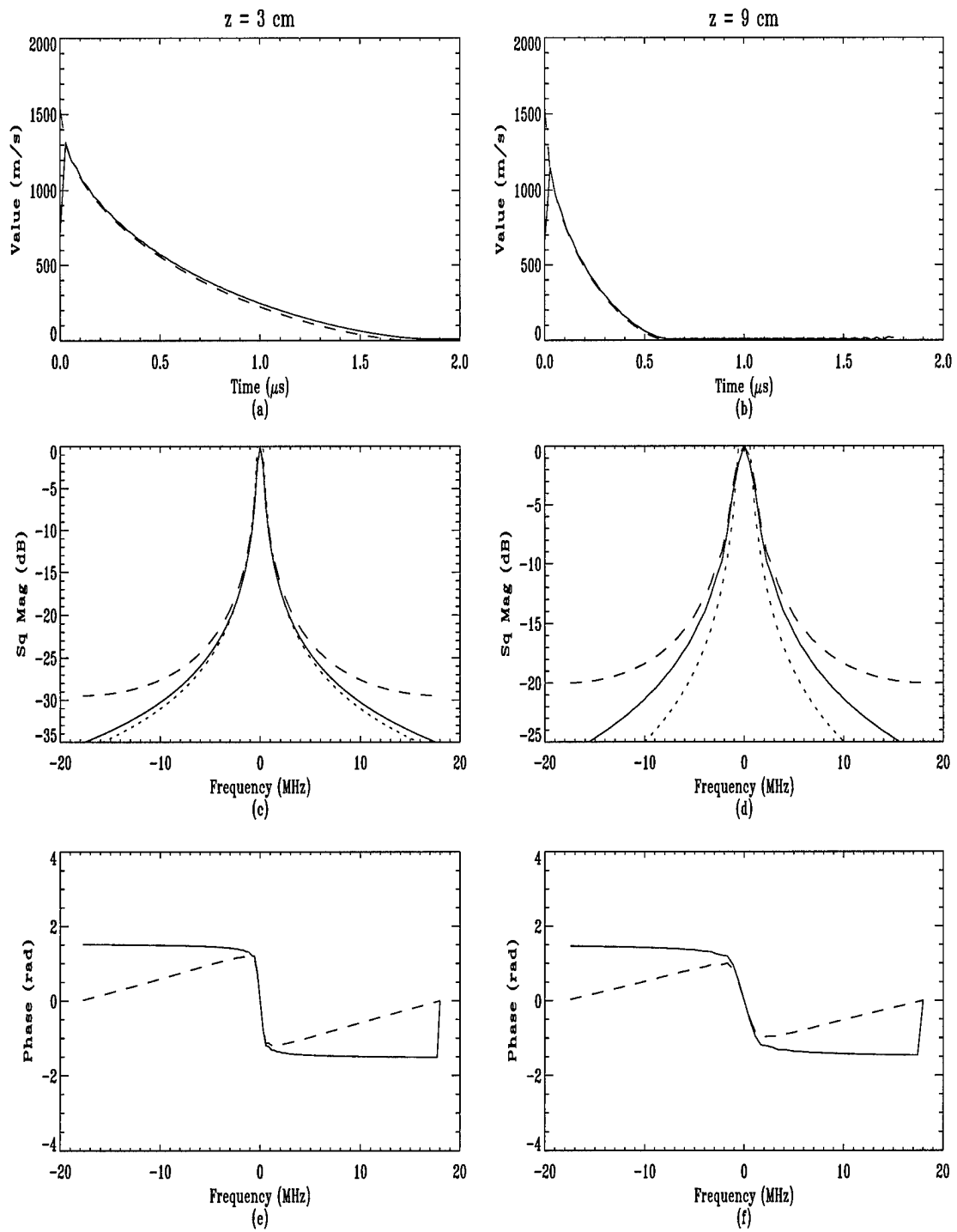


Figure 4.5: One-way spatially averaged impulse responses for the Lommel (solid) and arccos (dashed) diffraction formulations: $b = a$.

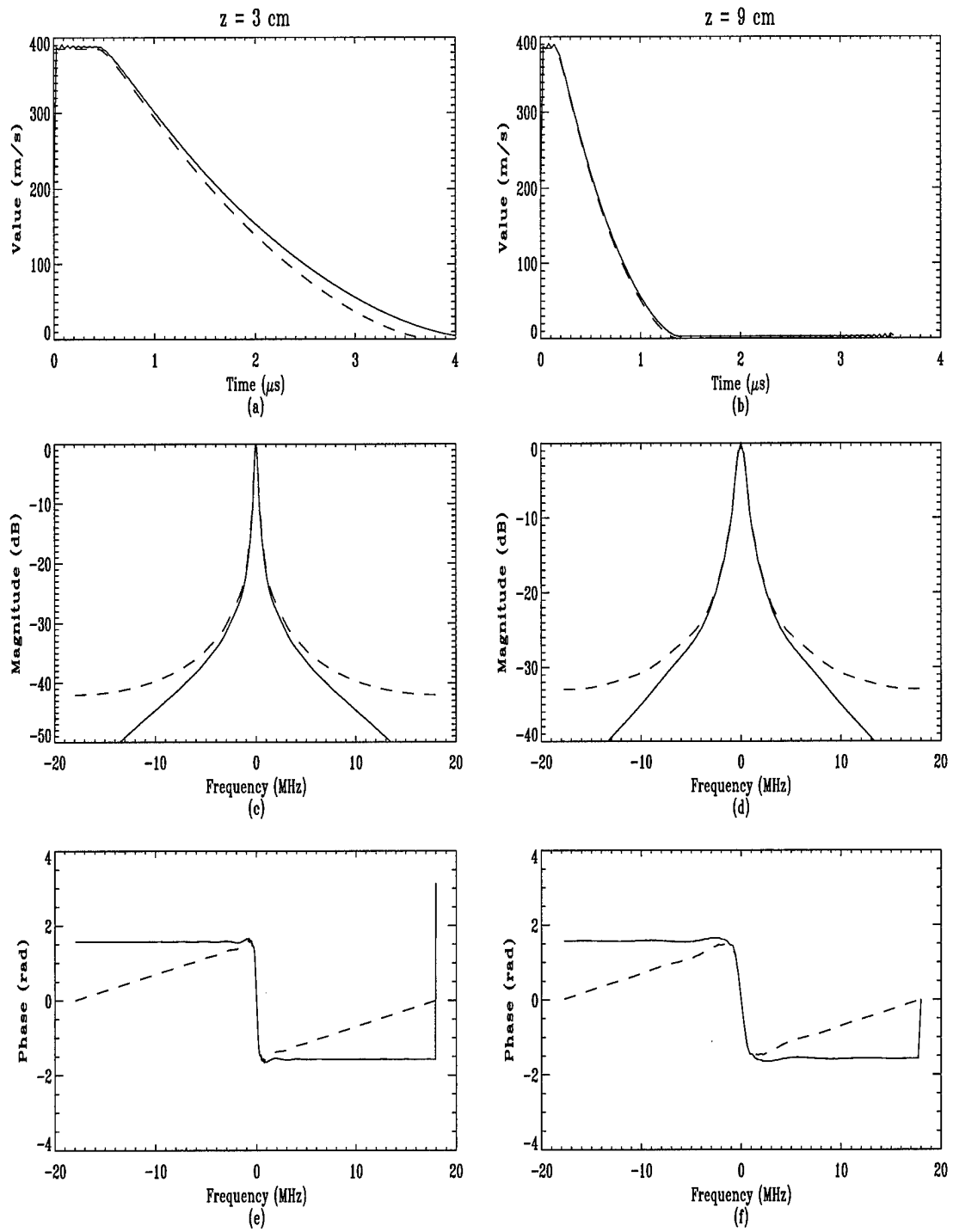


Figure 4.6: One-way spatially averaged impulse responses for the Lommel (solid) and arccos (dashed) diffraction formulations: $b = 2a$.

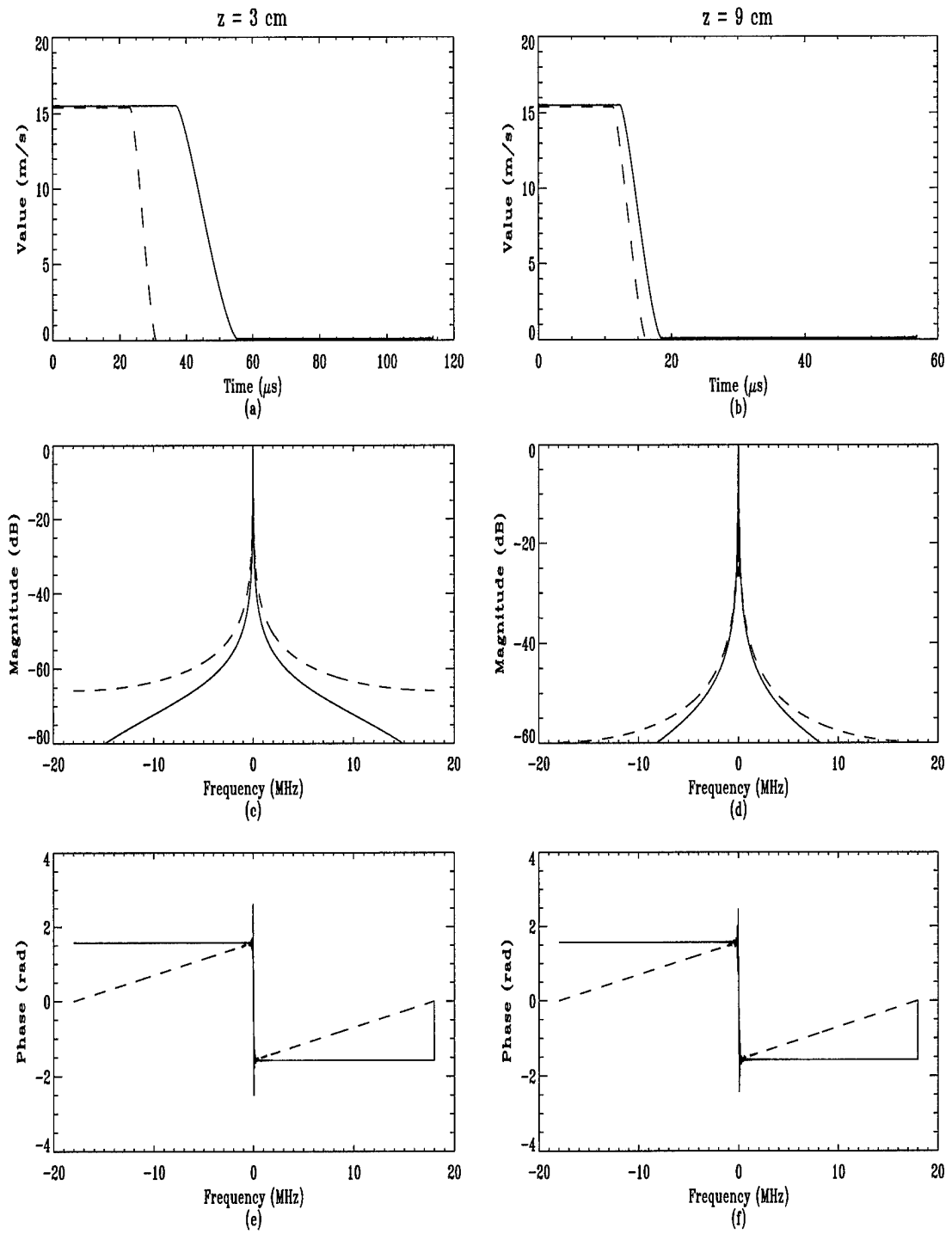


Figure 4.7: One-way spatially averaged impulse responses for the Lommel (solid) and arccos (dashed) diffraction formulations: $b = 10a$.

explain the phase differences exhibited in the plots. Reasons for the spectral discontinuity at the Nyquist frequency are not fully understood.

It is crucial to note, however, that Eq. 4.11 was derived under the assumption of an ideal piston transducer with a Dirac response. Thus, Eq. 4.11 is completely general in terms of frequency. Real transducers, however, are bandlimited. This observation also holds for Eq. 4.10 and Eq. 4.17 and bodes well for the unified theory being proposed.

For example, let's consider a real 2.25-MHz unfocused piston transducer with diameter $2a = 13$ mm. A typical bandwidth for such a transducer is 2 to 4 MHz centered at 2.25 MHz. Clearly, the results shown in Fig. 4.5 apply to the real transducer just described. Indeed, they apply quite well, particularly in a magnitude sense, with just 2X oversampling. Thus, if a diffraction correction were desired for this transducer, Eq. 4.11 could be used to calculate an inverse filter directly in the frequency-domain. Furthermore, higher sampling rates could be used, and the results applied to real transducers operating at a frequencies higher than 2.25 MHz.

Of course, Eq. 4.5 could be used to implement the diffraction correction as a time deconvolution [10]. In fact, Eq. 4.5 is more general than Eq. 4.11, but an FFT is required if frequency-domain results are desired. On the other hand, Eq. 4.11 can be calculated directly in the frequency domain across any bandwidth of interest. Clearly though, Eq. 4.5 is superior if an impulse response is desired. Nonetheless, we have demonstrated the utility of the proposed unified theory for spatially averaged one-way diffraction.

Figs. 4.3–4.4 and Figs. 4.6–4.7 show results for cases when $b \neq a$. With the exception of discontinuities, the results show remarkable qualitative and quantitative agreement, and the discussion of results obtained for $b = a$ apply.

Indeed, the spatially averaged results for $b = a/1000$ shown in Figs. 4.3(a)–(b) are consistent with the results predicted by point-receiver theory [59]. In particular, the case $b = a/1000$ approximates the case of an on-axis ($\rho = 0$) point receiver, and Eq. 3.11 predicts that the velocity-potential impulse response $h_1(\rho, z, t)$ for this case should resemble a rectangular pulse. Spatially averaged impulse responses $\langle \hat{h}_1(z, t) \rangle_b$ computed with Eq. 4.10

for $b = a/1000$ are consistent with the point-receiver theory. The temporal duration of the Lommel-based impulse responses differ from the arccos-based impulse responses for $b > a$ because Eq. 4.18 is based on the Fresnel approximation while Eq. 4.5 is based on the Rayleigh-Sommerfeld diffraction integral.

Finally, the results shown in Fig. 4.5 place the difference between spatial averaging and spatial integration [27,67] in new perspective. The spatially averaged results shown in the figure are consistent in every respect with the theory of one-way diffraction for a point receiver presented in the previous chapter. See in particular Fig. 3.3 (a-b) and note the amplitude of the pulses. Spatially integrated results would differ by a factor of πb^2 .

4.5 Computational Considerations

The computational issues discussed in Chapter 3 apply here. Analog frequency was used to compute Eq. 4.18 and the results multiplied by Δf prior to inverse Fourier transforming. Finally, the highest-order Bessel function used in computations of X_2 and Y_2 was $J_{63}(x)$.

4.6 Chapter Summary

Closed-form time-domain and frequency-domain expressions applicable to unfocused one-way diffraction with a finite receiver of any radius were derived. The time-domain expressions were derived by interpreting a spatially averaged version of the integral form of the arccos diffraction formulation as a Hankel transform and borrowing results derived by Gaskill [22]. The time-domain results turned out to be the same as results derived by Cassereau, *et al.* [10], but the derivation was different. On the other hand, the frequency-domain results were derived by direct spatial integration of the Lommel diffraction formulation.

The comparison of results obtained from the time- and frequency-domain expressions verified the theoretical prediction that the Fourier equivalence of the arccos and Lommel diffraction formulations could be extended to spatially averaged one-way diffraction.

The results showed remarkable agreement for $b \approx a$ and began to disagree with $b > a$. However, this disagreement was nicely explained by the theory. Specifically, the time-domain expressions are more general, in terms of ρ and z , than the frequency-domain expressions because the former expressions are based on Rayleigh-Sommerfeld diffraction while the latter are based on the Fresnel approximation to Rayleigh-Sommerfeld diffraction. Overall, the results obtained in this chapter cause us to be optimistic that the Fourier equivalence of the arccos and Lommel diffraction formulations can be extended to the autoconvolution interpretation of two-way diffraction. Finally, the one-way results derived in this chapter can be applied to the mirror-image interpretation of two-way diffraction simply by doubling z in Eq. 4.5 and Eq. 4.18.

Chapter 5

Spatially Averaged Two-Way Diffraction

Chapter 3 established the Fourier equivalence of the arccos and Lommel diffraction formulations for one-way diffraction with a point receiver, and Chapter 4 extended this Fourier equivalence to spatially averaged one-way diffraction. This chapter explores the possibility of extending the theory of approximate Fourier equivalence to a spatially averaged version of the autoconvolution interpretation of two-way diffraction. The mirror-image interpretation of two-way diffraction is trivial (Section 1.4 and Section 4.6) and not discussed here.

5.1 Spatially Averaged Arccos Diffraction Formulation

A linear model of reflection imaging is the mathematical starting point. The model developed by Hunt, *et al.* [29] will serve nicely. Adapted to our purposes, it is

$$v_R(\rho, z, t) = \left[\rho \frac{\partial^2 v_T(t)}{\partial t^2} * g_T(t) * s(t) * g_R(t) \right] * h_T(\rho, z, t) * h_R(\rho, z, t) \quad (5.1)$$

where the subscripts T and R denote transmit and receive, respectively, $v_R(t)$ is the voltage at the output of the receiver, and $v_T(t)$ is the excitation voltage. The transmit and receive responses of the transducer are $g_T(t)$ and $g_R(t)$, respectively, and are assumed to be delta

functions (Section 1.10). The impulse response $h(\rho, z, t)$ represents the propagation effects, and $s(t)$ is the impulse response for a point scatterer. The convolutions are performed over time t . Discussion about the order and placement of time derivatives and other idiosyncrasies of two-way ultrasound models is postponed until Chapter 7. See Jensen [31] or Cassereau, *et al.* [10] for more discussion on linear models of ultrasound.

To derive a closed-form solution for spatially averaged autoconvolution diffraction, it will be necessary to model $v_T(t)$ and $s(t)$ as delta functions and assume the transmit and receive propagation effects are due to diffraction only. In short, frequency-dependent scattering and frequency-dependent attenuation not included in the current derivation. These effects can be taken into account once diffraction effects in Eq. 5.1 have been filtered out. Attention may now be focused on the convolution outside the brackets in Eq. 5.1.

Consider Fig. 3.1 in terms of Eq. 5.1 and assume a point scatterer at some off-axis distance ρ . Since the convolution of $h_T(\rho, z, t)$ and $h_R(\rho, z, t)$ has been assumed to involve diffraction only, Helmholtz's reciprocity theorem in conjunction with Hyugen's principle [34] can be used to write

$$h_2(\rho, z, t) = h_1(\rho, z, t) * h_1(\rho, z, t) \quad (5.2)$$

where the subscripts 1 and 2 denote one-way and two-way diffraction, respectively. Thus, the two-way impulse response for the case of a point scatterer is an autoconvolution of the one-way velocity-potential impulse response for that same point scatterer. Fink interpreted two-way diffraction this way in Eq. 12 of [18]. Eq. 5.2 is the autoconvolution interpretation of two-way diffraction.

Note Eq. 5.2 is valid for a point scatterer only. Spatial averaging is required to estimate the effects of two-way diffraction for reflection from a plate as shown in Fig. 5.1. Note that Fig. 4.1 and Fig. 5.1 differ only in interpretation. The disk is interpreted as a *receiving* disk in the former and as a *reflecting* disk in the latter. As explained in Section 1.5, spatial integration over a volume is more realistic but more difficult, and a plane is assumed for mathematical simplicity. The averaging is done by dividing by πa^2 because

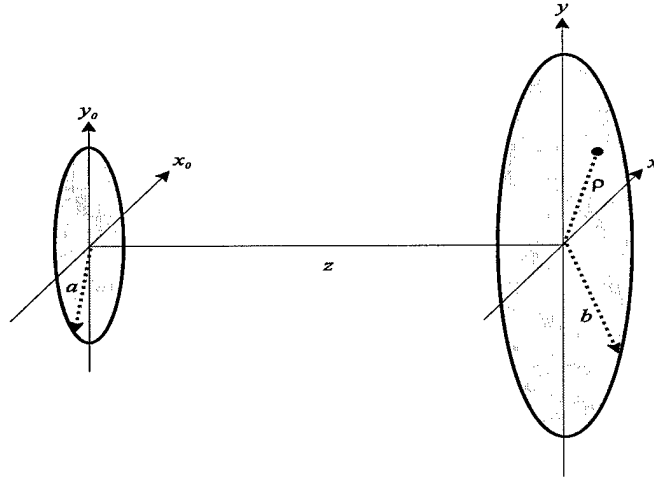


Figure 5.1: Piston transducer and reflecting disk.

the transducer acts as both transmitter and receiver.

The reflecting plane can be any shape but is assumed to be a disk for mathematical tractability. Spatially integrating Eq. 5.2 over the surface of the reflecting disk and dividing by the receiver area yields

$$\langle h_2(z, t) \rangle_b = \frac{1}{\pi a^2} \left[2\pi \int_0^b h_1(\rho, z, t) * h_1(\rho, z, t) \rho d\rho \right]. \quad (5.3)$$

Note the angular integration from 0 to 2π has been completed. Unfortunately, Eq. 5.3 is simply too complicated to solve in closed form. Other tactics must be employed.

5.2 Spatially Averaged Lommel Diffraction Formulation

Our initial attack on a spatially averaged form of autoconvolution diffraction was turned back by an extraordinarily difficult time-domain integral (Eq. 5.3). A counter-attack in the frequency domain will lead to a limited but nonetheless satisfactory and respectable victory. In this section, it will be shown that magnitude-only expressions based on Wolf's treatment [68] of monochromatic optical diffraction can be adapted to ultrasonic piston transducers operating in pulsed mode. The assumption of minimum phase will

enable approximation of a phase response which, in turn, will allow easy estimation of the spatially averaged two-way impulse for autoconvolution diffraction.

The Fourier transform of Eq. 5.3 is

$$\langle H_2(z, \omega) \rangle_b = \frac{1}{\pi a^2} \left[2\pi \int_0^b H_1(\rho, z, \omega) H_1(\rho, z, \omega) \rho d\rho \right]. \quad (5.4)$$

Furthermore, we invoke the Fourier equivalence of the arccos and Lommel diffraction formulations (Chapter 3) and substitute the focused Lommel diffraction formulation $\hat{H}_1(\rho, z, \omega)$ (Eq. 3.18) for $H_1(\rho, z, \omega)$.

The integral that results from substituting $\hat{H}_1(\rho, z, \omega)$ for $H_1(\rho, z, \omega)$ in Eq. 5.4 is still complicated because of the implicit demand to retain the phase of the two-way transfer function in Eq. 5.4. Recall that phase is required to compute an impulse response via an inverse Fourier transform. If the demand for phase information is dropped, Eq. 5.4 in magnitude-squared form becomes

$$\left| \langle \hat{H}_2(z, \omega) \rangle_b \right|^2 = \left| \frac{1}{\pi a^2} \left[2\pi \int_0^b \hat{H}_1(\rho, z, \omega) \hat{H}_1(\rho, z, \omega) \rho d\rho \right] \right|^2, \quad (5.5)$$

and the Cauchy-Schwarz inequality for integrals permits us to write

$$\left| \frac{1}{\pi a^2} \left[\int_0^b \hat{H}_1^2(\rho, z, \omega) \rho d\rho \right] \right|^2 \leq \left(\frac{1}{\pi a^2} \left[2\pi \int_0^b |\hat{H}_1(\rho, z, \omega)|^2 \rho d\rho \right] \right)^2. \quad (5.6)$$

The Cauchy-Schwarz inequality also indicates that equality in Eq. 5.6 *does not* hold; so

$$\left| \langle \hat{H}_2(z, \omega) \rangle_b \right|^2 < \left(\frac{1}{\pi a^2} \left[2\pi \int_0^b |\hat{H}_1(\rho, z, \omega)|^2 \rho d\rho \right] \right)^2. \quad (5.7)$$

Taking the square root of Eq. 5.7 yields

$$\left| \langle \hat{H}_2(z, \omega) \rangle_b \right| < \frac{1}{\pi a^2} \left[2\pi \int_0^b |\hat{H}_1(\rho, z, \omega)|^2 \rho d\rho \right]. \quad (5.8)$$

Eq. 5.8 provides an upper bound for the magnitude response associated with the spatially averaged autoconvolution impulse response.

This upper bound can be interpreted mathematically by letting

$$f(\rho, z, t) = h_1(\rho, z, t) \star h_1(\rho, z, t), \quad (5.9)$$

where \star denotes correlation over time t , and $f(\rho, z, t)$ is the autocorrelation of the one-way diffraction impulse response $h_1(\rho, z, t)$. Spatially averaging $f(\rho, z, t)$ and taking its Fourier transform yields

$$\mathcal{F} \left\{ \frac{1}{\pi a^2} \left[2\pi \int_0^b h_1(\rho, z, t) \star h_1(\rho, z, t) \rho d\rho \right] \right\} \approx \frac{1}{\pi a^2} \left[2\pi \int_0^b |\hat{H}_1(\rho, z, \omega)|^2 \rho d\rho \right], \quad (5.10)$$

where the Fourier equivalence of the arccos and Lommel diffraction formulations has been invoked. Note that the right-hand sides of Eq. 5.8 and Eq. 5.10 are equal. Thus, the magnitude of the spatially averaged *autoconvolution* impulse response is strictly less than the magnitude of the spatially averaged *autocorrelation* impulse response.

With this insight in mind, we make the *ad hoc* assumption that the magnitude of the spatially averaged autoconvolution impulse response is approximately equal to the magnitude of the spatially averaged autocorrelation impulse response:

$$|\langle \hat{H}_2(z, \omega) \rangle_b| \approx \frac{1}{\pi a^2} \left[2\pi \int_0^b |\hat{H}_1(\rho, z, \omega)|^2 \rho d\rho \right]. \quad (5.11)$$

Our results will justify the assumption.

With $u = ka^2/|\epsilon|$, $v = ka\rho/z$, and $v_b = kab/z$, Eq. 5.11 becomes

$$|\langle \hat{H}_2(z, \omega) \rangle_b| \approx \frac{1}{k^2} \left\{ \frac{2}{u^2} \int_0^{v_b} [U_1^2(u, v) + U_2^2(u, v)] v dv \right\}. \quad (5.12)$$

Wolf solved the braced integral in Eq. 5.12 for $v_b < u$, $v_b = u$, and $v_b > u$ [68]. Thus, the *ad hoc* assumption in Eq. 5.11 allows us to borrow Wolf's results for optical diffraction and apply them to a spatially averaged form of the autoconvolution diffraction. The results for the three regions are for $b < a$,

$$\begin{aligned} |\langle \hat{H}_2(z, \omega) \rangle_b| \approx \frac{1}{k^2} \left(\left(\frac{v_b}{u} \right)^2 \left[1 + \sum_{s=0}^{\infty} \frac{(-1)^s}{2s+1} \left(\frac{v_b}{u} \right)^{2s} Q_{2s}(v_b) \right] \right. \\ \left. - \frac{4}{u} \left[Y_1(u, v_b) \cos \left(\frac{u}{2} + \frac{v_b}{2u} \right) + Y_2(u, v_b) \sin \left(\frac{u}{2} + \frac{v_b}{2u} \right) \right] \right), \quad (5.13) \end{aligned}$$

for $b = a$,

$$\langle \hat{H}_2(z, \omega) \rangle_b \approx \frac{1}{k^2} \left(1 - J_0(u) \cos(u) - J_1(u) \sin(u) \right), \quad (5.14)$$

and for $b > a$,

$$\langle \hat{H}_2(z, \omega) \rangle_b \approx \frac{1}{k^2} \left(1 - \sum_{s=0}^{\infty} \frac{(-1)^s}{2s+1} \left(\frac{u}{v_b} \right)^{2s} Q_{2s}(v_b) \right). \quad (5.15)$$

These results reduce to the case of an unfocused transducer in the limit as $f \rightarrow \infty$ since $\lim_{f \rightarrow \infty} \epsilon = z$.

5.3 Extending Fourier Equivalence with Minimum Phase

We should be able to apply the theory of approximate Fourier equivalence to spatially averaged autoconvolution diffraction. However, Eqs. 5.13-5.15 contain no phase information; thus, the inverse Fourier transform will be insufficient when it comes to computing a spatially averaged autoconvolution impulse response. The concept of minimum phase [51] will help overcome this problem.

In simplistic terms, a minimum-phase system is one that is causal and stable; see Rabiner and Schafer [51] for details and definitions. A general property of a minimum-phase system is that its phase response can be calculated from its magnitude response and vice versa. Since the autoconvolution of $h_1(\rho, z, t)$ is both causal and stable, the minimum-phase solution is assumed. The minimum-phase assumption is not without precedent in ultrasound. See, for example, Kuc's paper on modeling acoustic attenuation [36]. Thus,

$$\langle \hat{h}_2(z, t) \rangle_b = \mathcal{F}^{-1} \left\{ \left| \langle \hat{H}_2(z, \omega) \rangle_b \right| e^{\pm j\phi(\omega)} \right\} \quad (5.16)$$

where the minimum phase $\phi(\omega)$ is the Hilbert transform of $\ln(|\langle \hat{H}_2(z, \omega) \rangle_b|)$. The choice of sign in Eq. 5.16 depends on the depth z and accounts for the time reversal of the focused arccos diffraction formulation when $z > R$ [2]; recall R is the focal length (Section 3.7). No such time reversal occurs in the unfocused case, and the sign of the phase is chosen based on the sign convention of the FFT being used. Recall Eq. 5.16 is based on Eq. 3.18 which, as explained in Section 3.7, holds for focused and unfocused transducers; thus Eq. 5.16 theoretically holds for both focused and unfocused piston transducers.

5.4 Verification

Results obtained from Eq. 5.16 were plotted against results computed via numerical integration of the arccos diffraction formulation. Figs. 5.2–5.5 illustrate the results. All results were normalized to a maximum value of unity for reasons which will be discussed in Section 5.5.

Before discussing the results, we should note well that Eq. 5.16 is an assumption in an approximation wrapped in estimation. Specifically, we have made the *ad hoc* assumption that the magnitude of $\langle \hat{H}_2(z, \omega) \rangle_b$ is approximately equal to its upper bound as calculated by the Cauchy-Schwarz inequality (Eq. 5.11). Additionally, $\langle \hat{H}_2(z, \omega) \rangle_b$ is based on the Fresnel approximation. Finally, the phase response of $\langle \hat{h}_2(z, \omega) \rangle_b$ is estimated using the minimum-phase assumption, and the DC value of $\langle \hat{h}_2(z, t) \rangle_b$ is estimated by the method described in Section 3.6. Thus, if the normalized results shown in the figures are in reasonable agreement, we should declare victory and not necessarily quibble about how the battle was fought.

The data plotted in the figures were computed for an *unfocused* piston transmitter with diameter $2a = 13$ mm and a reflecting disk with radius b . Four different values of b were used, and these are noted in the figures. As in the one-way case, the impulse responses were calculated for two depths: $z = 3$ cm and $z = 9$ cm. The speed of sound was set at $c = 1540$ m/s, and the transducer was assumed to have an infinitely broadband response. The excitation was assumed to be an impulse. The sampling frequency was set at $f_S = 36$ MHz; thus, the Nyquist frequency was 18 MHz. Only Fig. 5.4 is discussed in detail. Concise comments pertaining to the Figs. 5.2–5.3 and Fig. 5.5 follow the discussion of Fig 5.4.

Figs. 5.4(a)–(b) show two-way spatially averaged impulse responses estimated via Eq. 5.16 (solid lines) and spatially averaged two-way impulse responses calculated by numerical integration of Eq. 5.3 (dashed lines). The results computed using Eq. 5.16 differ only slightly from the results computed by numerically integrating the autoconvolution of the arccos formulation, but otherwise the Lommel-based results capture the salient features computed by numerical integration, particularly time-compression with increasing depth. These results justify the assumptions discussed at the beginning of this section.

Figs. 5.4(c)–(d) show the squared magnitude responses (dB) associated with the impulse responses in Fig. 5.4(a) and Fig. 5.4(b), respectively. The magnitude responses show excellent agreement over a wide range of frequencies. As in the one-way case, better agreement can be had at higher frequencies if the sampling frequency is increased, but again the cost is more samples. The ease of computing the magnitude response with Eq. 5.14 must be emphasized; numerical integration and do-loops are not required. Furthermore, computation can be done directly in the frequency domain. The dotted lines in the plots will be discussed in Section 7.2.

Figs. 5.4(e)–(f) show the phase responses associated with the impulse responses in Fig. 5.4(a) and Fig. 5.4(b), respectively. The results show satisfactory agreement, but the computation of each phase response required a Hilbert transform. However, the Hilbert transform is a routine computation in signal processing which can be implemented fairly easily [70]. Finally, as in the one-way case, it is crucial to note Eqs. 5.13–5.15 were derived under the assumption of an ideal piston transducer with a Dirac response. As a result, Eqs. 5.13–5.16 are completely general in terms of frequency. But real transducers are bandlimited.

As in the one-way case, let's consider a real 2.25-MHz unfocused piston transducer with diameter $2a = 13$ mm. A typical bandwidth for such a transducer is 2 to 4 MHz centered at 2.25 MHz. Clearly, the results shown Fig. 5.4 apply to this real transducer. Indeed, they apply quite well, particularly in a magnitude sense, with only 2X oversampling. Thus, if a spatially averaged autoconvolution diffraction correction were desired for this transducer, Eq. 5.14 could be used to calculate an inverse filter directly in the frequency domain. Furthermore, higher sampling rates could be used, and the results applied to real transducers operating at higher frequencies than 2.25 MHz. Thus, we have again demonstrated the utility of the proposed unified theory for spatially averaged diffraction correction.

Figs. 5.2–5.3 and Fig. 5.5 show results for $b \neq a$. Overall, the normalized results show quite satisfactory results given the stated approximations. Indeed, the spatially

averaged results for $b = a/1000$ in Fig. 5.2 are consistent with the results predicted by point-receiver theory [60]. In particular, the case $b = a/1000$ approximates the case of an on-axis ($\rho = 0$) point scatterer, and Eq. 5.2 predicts that $h_2(\rho, z, t)$ for this case should be triangular in shape as a result of convolving two rectangular pulses. Spatially averaged impulse responses $\langle \hat{h}_z(z, t) \rangle_b$ computed with Eq. 5.13 for $b = a/1000$ are consistent with the point-receiver theory.

Agreement between the two sets of results begins to break down with $b > a$ (Fig. 5.5). The behavior of Lommel-based results for $b > a$ has been noted in Section 3.5 and Section 4.4 and is not surprising since the Lommel diffraction formulation is based on the Fresnel approximation. Furthermore, the minimum-phase assumption may break down for $b > a$. Thus, we did not bother computing results for any $b > 2a$.

5.5 Computational Considerations

The five general computational issues discussed in Chapter 3 apply here; however, two caveats are needed. First, the time duration of the two-way impulse response must be increased to account for the temporal effects of autoconvolution; this can be handled by sufficient zero-padding. Second frequency-domain windowing was not used with Eq. 5.16 to produce the plots in Figs. 5.2–5.5 because there are no dramatic discontinuities evident in the impulse responses. Thus, Gibb’s phenomenon was not as pronounced as in the one-way case, and windowing was not required. This is not surprising because autoconvolution, in general, removes discontinuities [48, pp. 78–81].

Three new computational issues applicable only to spatially averaged autoconvolution diffraction require discussion. First, the arccos-based and Lommel-based impulse responses were normalized to unit amplitude because the scaling of $\langle h_2(z, t) \rangle_b$ remains an open question. The second computational consideration involves the assumption of minimum phase and demands more lengthy discussion. As noted earlier, the choice of sign in the minimum phase of Eq. 5.16 depends on the depth z and accounts for the time reversal

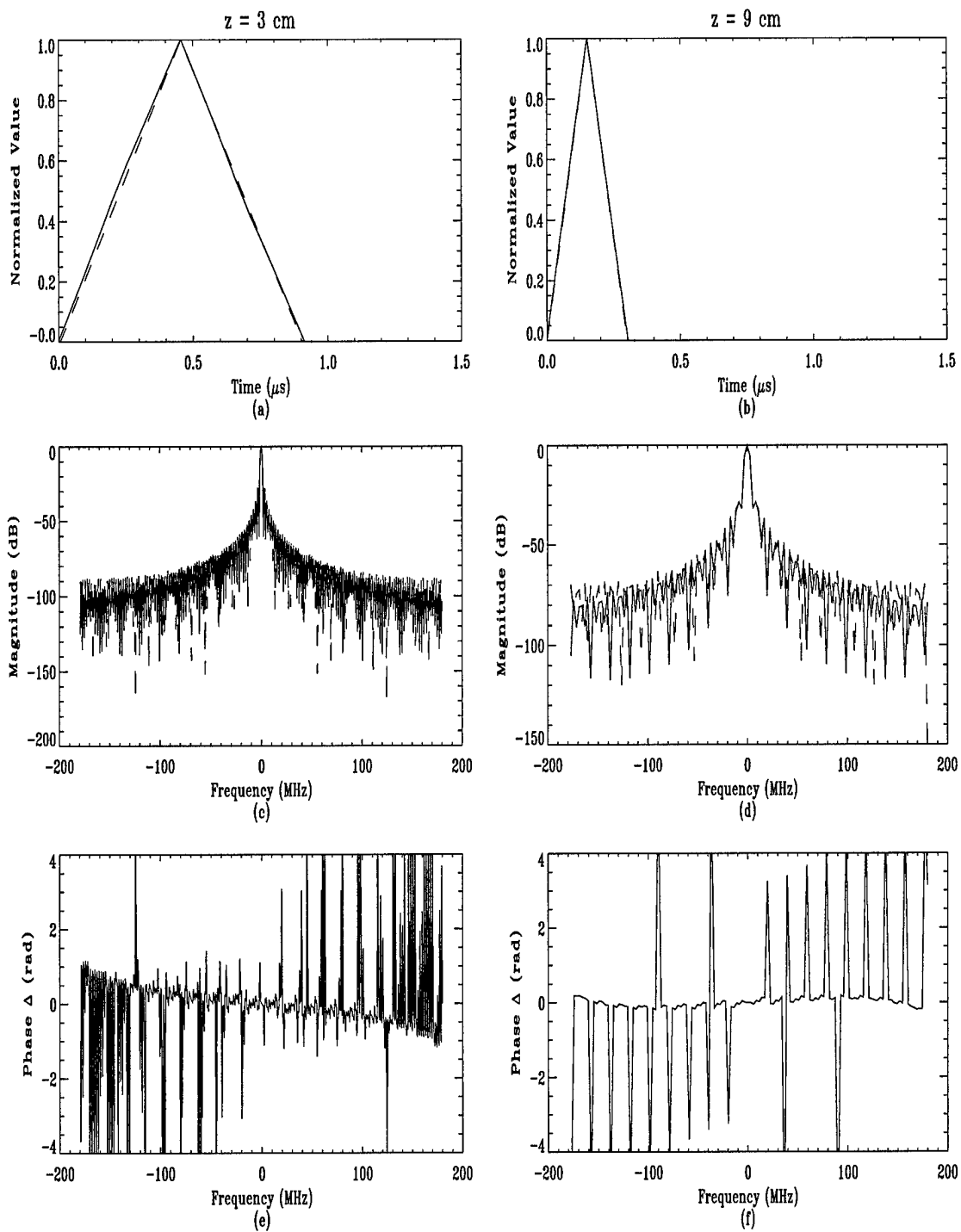


Figure 5.2: Two-way spatially averaged impulse responses for the Lommel (solid) and arccos (dashed) diffraction formulations: $b = a/1000$

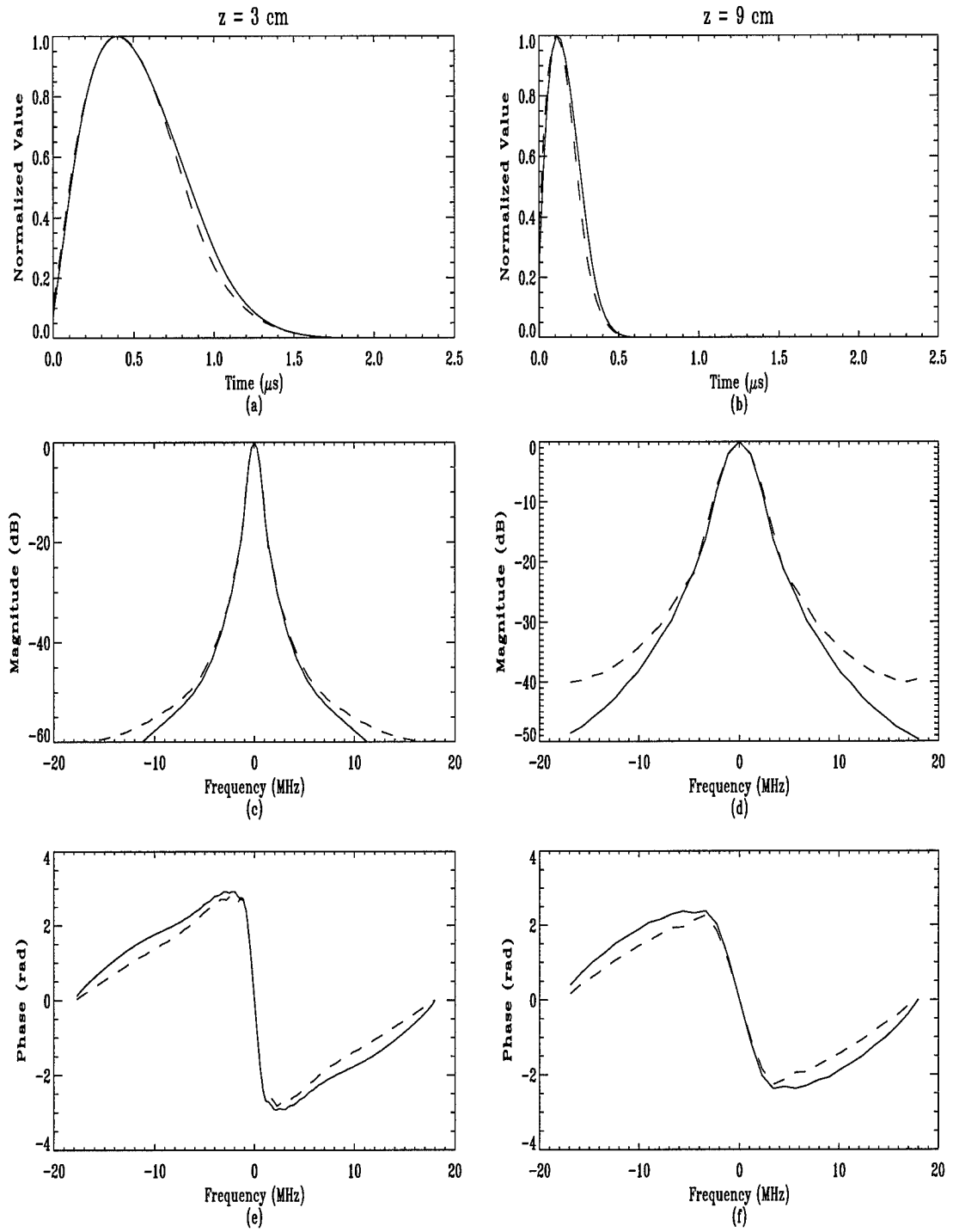


Figure 5.3: Two-way spatially averaged impulse responses for the Lommel (solid) and arccos (dashed) diffraction formulations: $b = a/2$

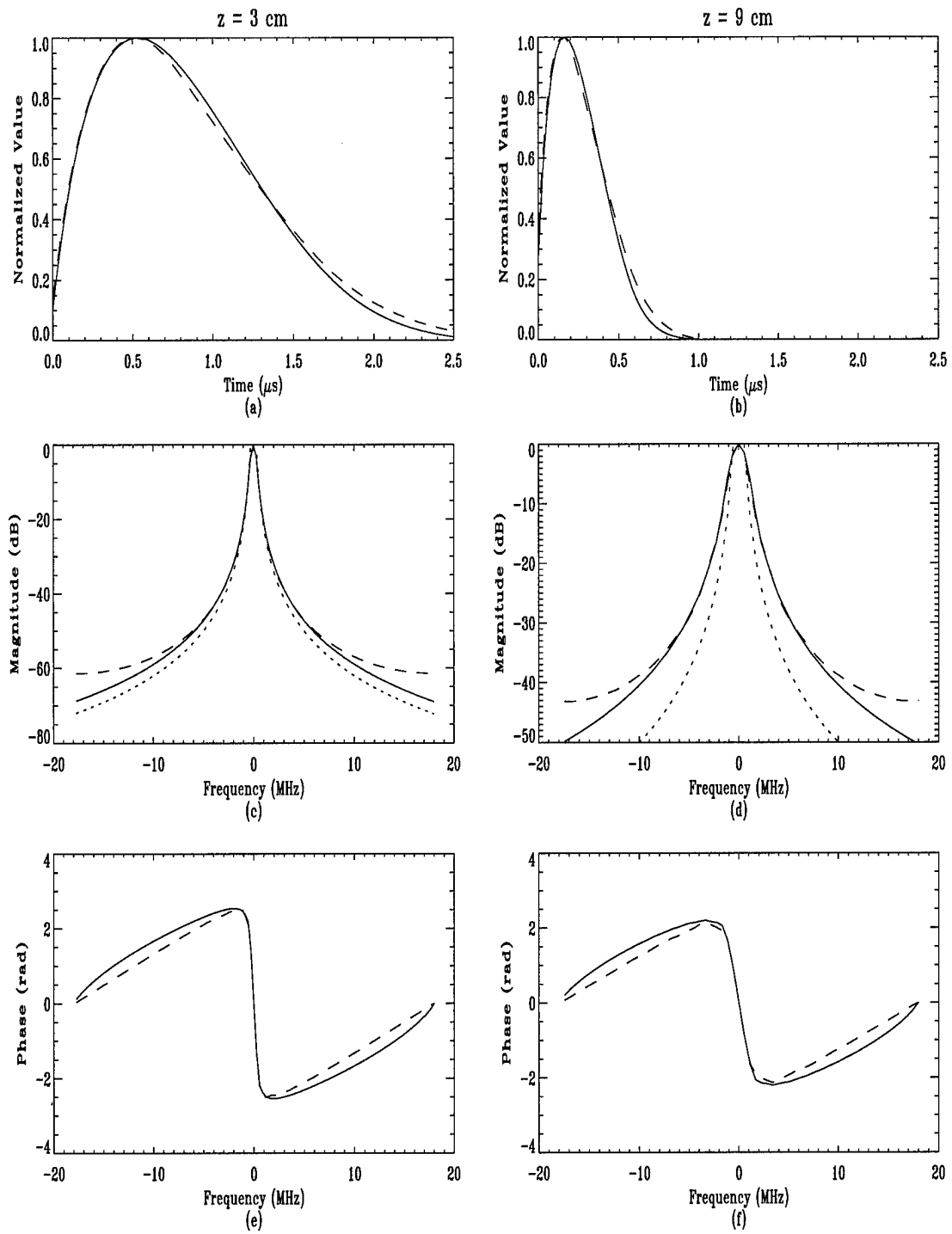


Figure 5.4: Two-way spatially averaged impulse responses for the Lommel (solid) and arccos (dashed) diffraction formulations: $b = a$

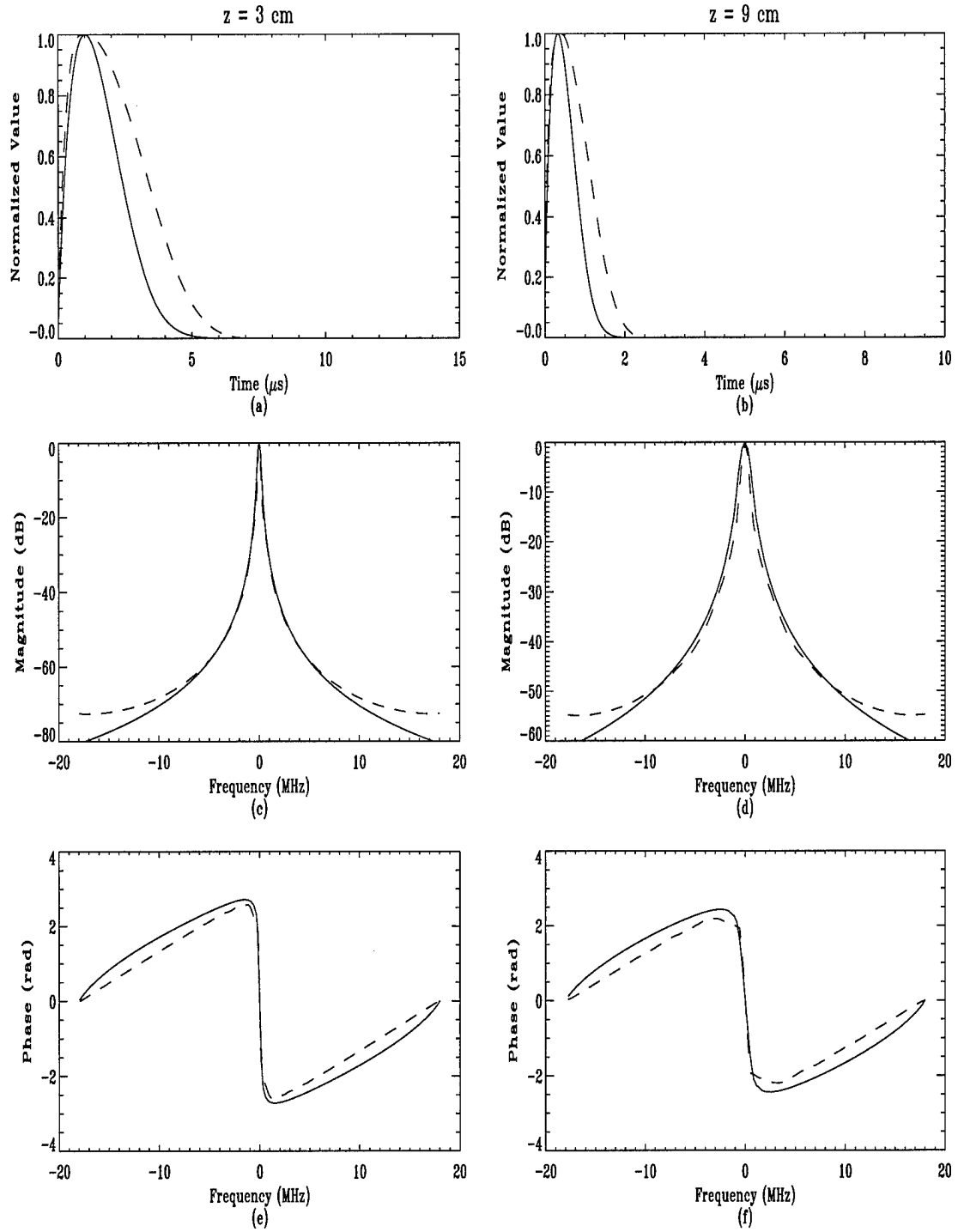


Figure 5.5: Two-way spatially averaged impulse responses for the Lommel (solid) and arccos (dashed) diffraction formulations: $b = 2a$

of the focused arccos diffraction formulation when $z > R$. No such time reversal occurs in the unfocused case phase, and the sign is chosen based on the sign convention of the FFT. Incorrect choice of sign results in a time-reversed impulse response.

The minimum phase assumption also produced some unexpected results. Specifically, the spatially averaged autoconvolution impulse response is expected to be positive semi-definite because $h_1(\rho, z, t)$ is positive semi-definite. However, the phase response calculated via the minimum-phase assumption sometimes caused the impulse response to be 180 degrees out of phase with the theoretically predicted value. This condition can be easily tested for and corrected algorithmically. Finally, considerable over-sampling in the frequency domain, particularly for $b \ll a$, may be required to obtain meaningful autoconvolution impulse responses from Eq. 5.16.

5.6 Chapter Summary

This chapter has shown that a set of equations derived by Wolf in 1951 for optical diffraction can be applied to spatially averaged autoconvolution diffraction for both focused and unfocused piston transducers operating in pulsed mode. Wolf's expressions are based on Lommel's treatment of Fresnel diffraction and are magnitude-only expressions; minimum phase was assumed in order to estimate the phase response. Results computed with the Lommel-based expressions were compared to results obtained from numerical integration of the arccos diffraction formulation. Given the number of approximations and assumptions involved, the normalized results showed excellent agreement. Autoconvolution diffraction was validated, in terms of magnitude *and* phase, for the unfocused case only, but it should hold for focused transducers. This claim is verified in a magnitude-only sense in Chapter 7.

Chapter 6

Experimental Investigation

The discussion up to this point has focused on developing and verifying a unified theory of spatially averaged diffraction corrections. In this chapter, an aspect of the unified diffraction theory is investigated experimentally. Specifically, autoconvolution diffraction corrections will be implemented with time-varying filters, and diffraction-corrected B-mode images will be reconstructed using a short-time Fourier technique. The raw and diffraction-corrected images will be compared in a qualitative sense. Differences between raw and corrected RF data will be quantitatively analyzed via spectral centroids (Section 1.6).

At this point it is necessary to reiterate the three points discussed in Section 1.7. First, the experiments were not designed to verify the theory in any authoritative fashion. Rather, they were designed to gauge the feasibility of the proposed autoconvolution diffraction correction. Second, the diffraction-corrected images are an important contribution of this work. Although the differences between the raw and diffraction-corrected images are subtle, they reveal that diffraction correction appears to affect RF data more than it does envelope-detected data. ***Finally, and most importantly, the experiments are not to be considered, in any way, clinical validation of the proposed diffraction corrections.***

It is also important to note that the autoconvolution diffraction corrections are based on Eq. 5.16 which was verified in terms of magnitude and phase for unfocused piston

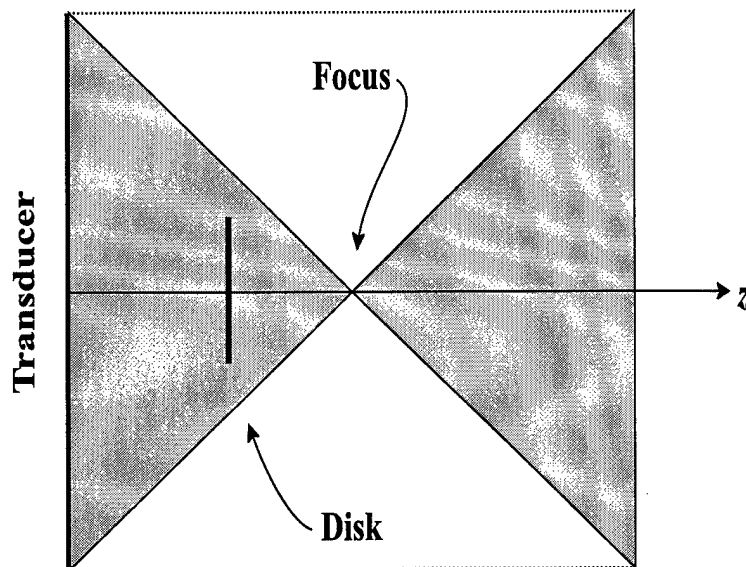


Figure 6.1: Reflecting disk in main beam.

transducers only. Hence, both magnitude and phase responses were computed and applied for unfocused corrections while only magnitude responses were computed and applied for focused corrections.

6.1 A Computational Consideration

Chapter 5 showed that effects due to autoconvolution diffraction depend on b , the radius of the reflecting disk. This, coupled with the fact that b is theoretically unrestricted, raises a new computational issue. Specifically, to the extent that Eqs. 5.13–5.15 and 5.16 model reality accurately, what b should be used in practice? An imprecise but intuitively appealing answer can be had if we consider Fig. 6.1 in terms of conservation of energy. The figure shows a reflecting disk located in the beam of a focused transducer.

Since no attenuation mechanism has been included in the theory, the total acoustic energy is constant for all z , but the energy density is not. Loosely speaking, the energy gets more concentrated at the focus. Since the energy density is not constant, the radius b of

the reflecting disk determines the amount of energy that is reflected back to the transducer. The extremes are $b = 0$ and $b \rightarrow \infty$; the former implies the transducer receives no reflected energy, while the latter implies the transducer receives all the reflected energy. For some finite b (say $0 < b < a$ as shown in the figure), the reflected energy varies as a function of z with maximum energy being reflected when the disk is located at the focus. The reflected energy decreases as the disk is moved away from the focus.

In practice, b will probably have to be varied as a function of depth z . For the purposes of this work, we simply fixed b at $0.516a$ for unfocused transducers and at $K_f a$ for focused transducers where K_f is the focusing factor; the focusing factor is approximately 0.2, 0.5, and 0.8 for short-, medium-, and long-focus transducers, respectively [35,46]. This discussion will be continued in Section 7.2.2.

6.2 Equipment, Parameters, and Processing

Unfocused diffraction corrections based on Eq. 5.16 and focused diffraction corrections based on the magnitude of Eq. 5.16 were applied to RF echo data obtained from a variety of piston transducers operating in pulsed mode. The RF data were obtained using the equipment shown in Fig. 6.2. A Panametrics model 5052PR pulser/receiver provided transducer excitation and initial amplification of the RF echo data. Data of interest were segmented with a Panametrics model 5052G gate. Additional amplification was provided by a RITEC model BR-640 broadband receiver, and the RF data was digitized to 8-bit resolution by a Data Precision 6100B universal waveform analyzer. The RF data were subsequently downloaded to a personal computer (PC). A stepper motor (not shown) was used to move the transducer.

All subsequent signal processing was done on the PC. Specifically, a diffraction filter was calculated using Eq. 5.16 for the bandwidth of interest. Next, the filter was normalized by its maximum value, and the corresponding inverse filter was calculated. The resulting diffraction correction was implemented as a time-varying filter via a short-time

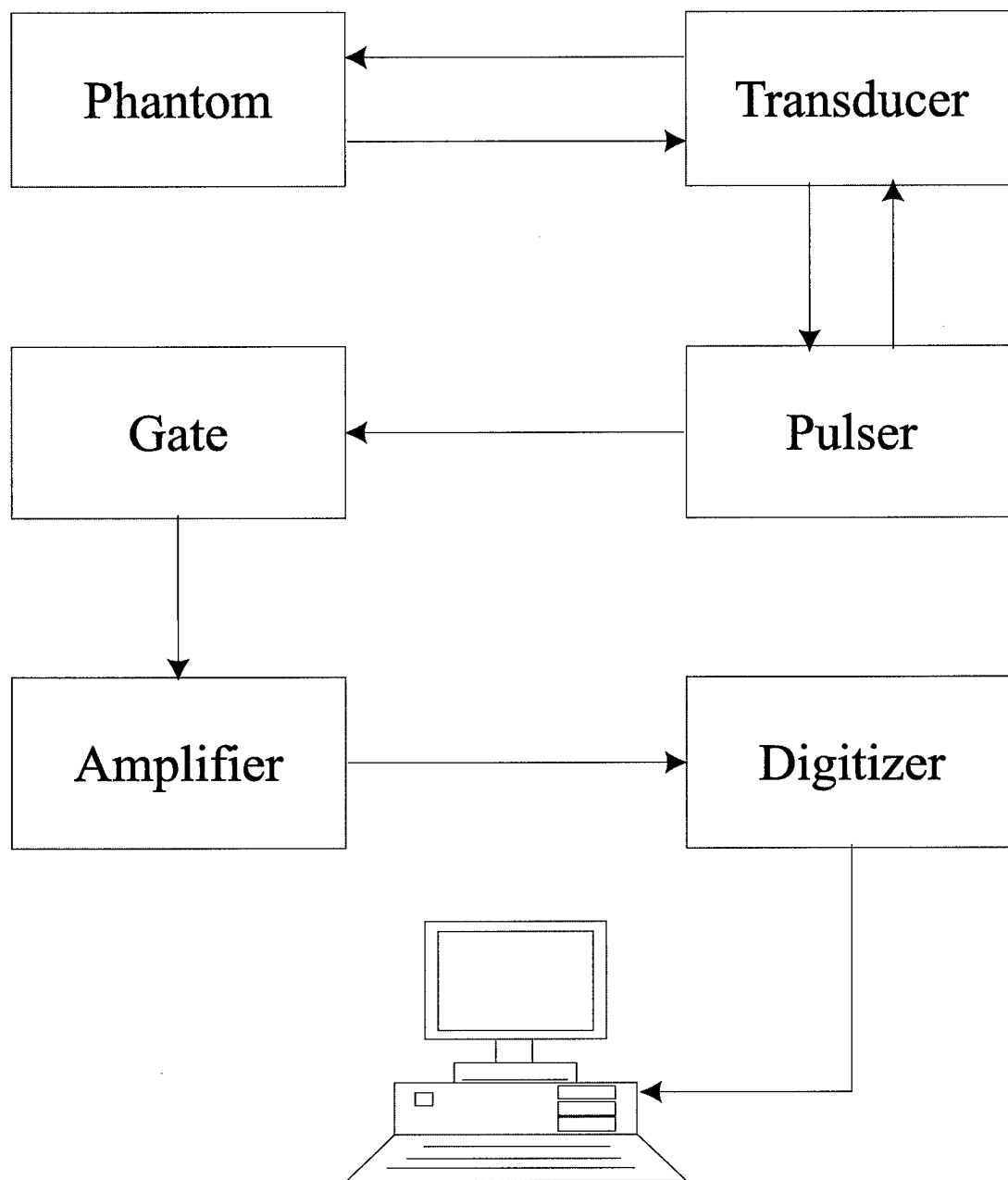


Figure 6.2: Experimental set-up.

Fourier technique known as the *weighted overlap-add* (WOLA) method [15]. Fig. 6.3 depicts the WOLA processing used in this work.

The following short-time Fourier parameters (see [51] for parameter definitions) were used: hop length of 4 samples, 256 filter coefficients from DC to the Nyquist frequency, and a window length of 31 samples zero-padded to 256 samples. A Hamming window was used in analysis, while the synthesis window was rectangular. The bandwidth of interest was defined as $f_c \pm f_c/2$, where f_c is the center frequency of the transducer. The RF sampling rate of the Data Precision 6100B was set at 40 nanoseconds and 20 nanoseconds for $f_c \leq 2.25$ MHz and $f_c > 2.25$ MHz, respectively. The sampling rate was later reduced by a factor of two in software. In each experiment, the transducer was perpendicular to the target, the distance between scans or lateral sampling rate was 0.3 mm, and no averaging was done in either the axial or lateral direction.

6.3 Experiments and Results

Results obtained from ten imaging experiments along with relevant imaging parameters are shown in Figs. 6.5–6.29 which are grouped at the end of the chapter for convenience. Figures containing gray-scale images obtained with *unfocused* transducers are followed by two figures which indicate the magnitude and phase filtering done to obtain the diffraction-corrected data. Figures containing gray-scale images obtained with *focused* transducers are followed by one figure which indicates the magnitude filtering done to obtain the diffraction-corrected data.

The format of the figures containing gray-scale images is as follows. The gray-scale images labeled (a) in the figures show B-mode images constructed from raw RF data. The images in Fig. 6.5(a) and Fig. 6.8(a) show a specimen of unfixed cancerous human breast tissue in water on a sponge (100 A-lines). The images in Fig. 6.11(a), Fig. 6.14(a), Fig. 6.16(a), and Fig. 6.19(a) show a specimen of unfixed pig liver in water on a sponge (50 A-lines). The images in Fig. 6.21(a), Fig. 6.23(a), and Fig. 6.25(a) show disks in an ATS

WOLA Diffraction Correction of i -th A-line

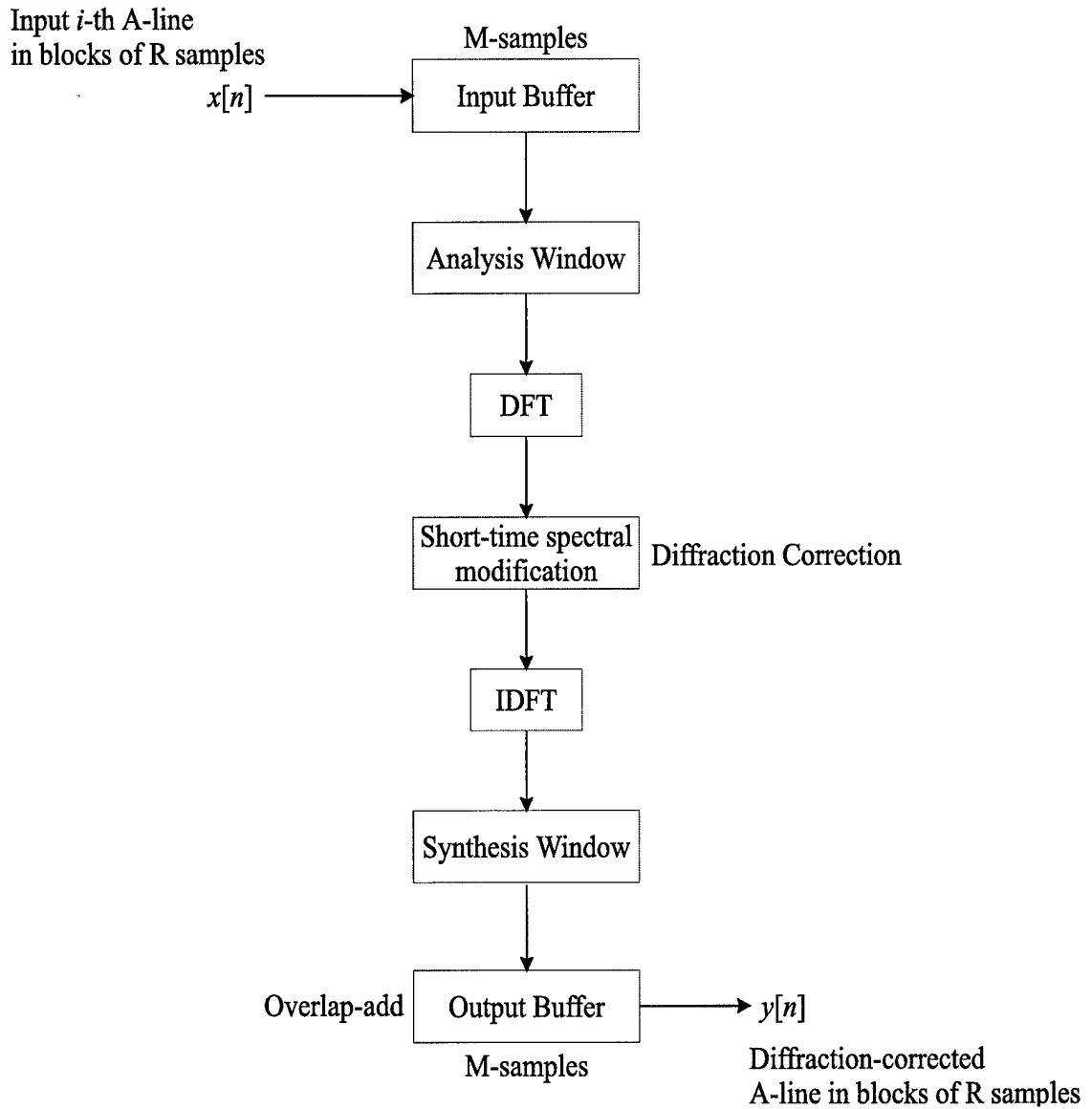


Figure 6.3: Short-time Fourier processing of A-lines.

Laboratories Model 539 attenuating phantom (60 A-lines). The wire-target data shown in Fig. 6.27(a) was taken from a standard AIUM wire phantom (24 A-lines with a 0.8 mm lateral sampling rate). The gray-scale images labeled (b) show B-mode images constructed from diffraction-corrected RF data. *No clinical data on the tissue or liver samples is provided because the experiments were not designed to demonstrate or validate the clinical efficacy of the proposed diffraction corrections.*

The plots labeled (c) and (d) in the figures containing gray-scale images are the FFT's of the middle A-line from the raw and corrected RF data, respectively. The FFT data were smoothed *after* log scaling to dB; hence, the maximum value is not 0 dB. The centroid plots labeled (e) and (f) in the figures with gray-scale images were made by calculating, via short-time Fourier transform, the spectral centroid of the middle A-line from the raw and corrected RF data, respectively. The centroid plots are annotated with the mean μ and variance σ computed from the respective centroid record. Recall that the spectral centroid measures the mean frequency of a signal (Section 1.6).

The figures immediately following the figures containing gray-scale images show the magnitude response and, for unfocused transducers, the phase response of the diffraction correction. The responses are plotted as a function of frequency in the column on the left, while they are plotted as a function of depth in the column on the right.

6.4 Discussion of Results

Diffraction correction affected the data in three ways. First, it performed a kind of depth-dependent time-gain correction which can be seen by comparing the raw and filtered gray-scale images. This claim is more forcefully illustrated in Fig. 6.4 which compares raw (solid) and diffraction-corrected (dotted) envelope data for two of the ten imaging experiments. The first two plots labeled (a) and (b) in Fig. 6.4 show single envelope-detected A-lines from the breast-tissue data (Fig. 6.8) and from the disk data (Fig. 6.21). The bottom two plots labeled (c) and (d) in Fig. 6.4 show the sum of all the envelope-detected A-lines for the two

sets of data; they are, in a sense, projections. The depth-dependent time-gain correction in the disk data is more pronounced when compared to the breast-tissue data because the disk data were taken with a lower-frequency transducer which exhibited more high-frequency attenuation due to diffraction.

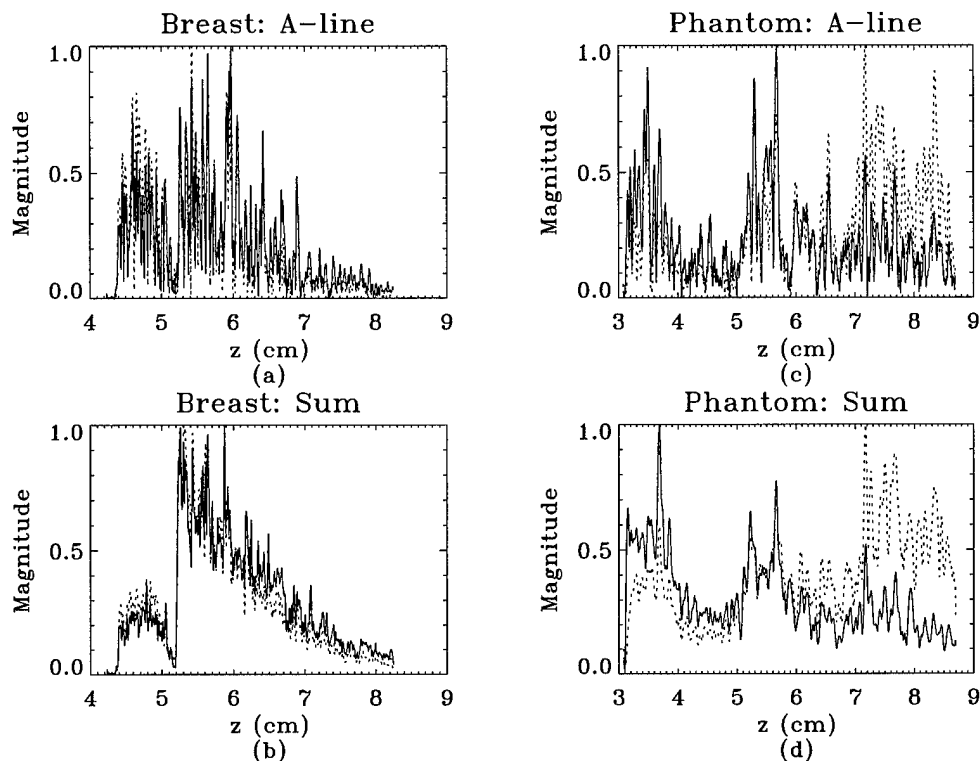


Figure 6.4: Raw (solid) and diffraction-corrected (dotted) envelope data.

Second, the diffraction correction is, in a spectral sense, a depth-dependent high-frequency amplifier. Compare the raw and diffraction-corrected gray-scale images. Qualitatively speaking, the diffraction-corrected images look crisper or sharper than the raw images. Additionally, compare the raw and filtered FFT's shown in the figures containing gray-scale images. Clearly, the high-frequency information contained in the useable bandwidth the diffraction-corrected data has a larger magnitude than the high-frequency information contained in the useable bandwidth of the raw data. Third, the diffraction

correction appears to reduce the variance of the spectral centroid. The variance reduction is more noticeable for focused transducers than for unfocused, but a quantifiable reduction has been achieved for all cases except one (Fig. 6.11).

6.5 Chapter Summary

This chapter experimentally investigated an aspect of the unified diffraction theory developed in previous chapters. Specifically, autoconvolution diffraction corrections were implemented with time-varying filters, and diffraction-corrected B-mode images were reconstructed using a short-time Fourier analysis/synthesis algorithm known as the weighted overlap-add (WOLA) method. The raw and diffraction-corrected images were compared only qualitatively. Differences between raw and corrected RF data were quantitatively analyzed via spectral centroids, a measure of average frequency. The experimental results prove that, at worst, the proposed diffraction correction does no harm and, at best, it removes spectral bias and appears to improve image quality.

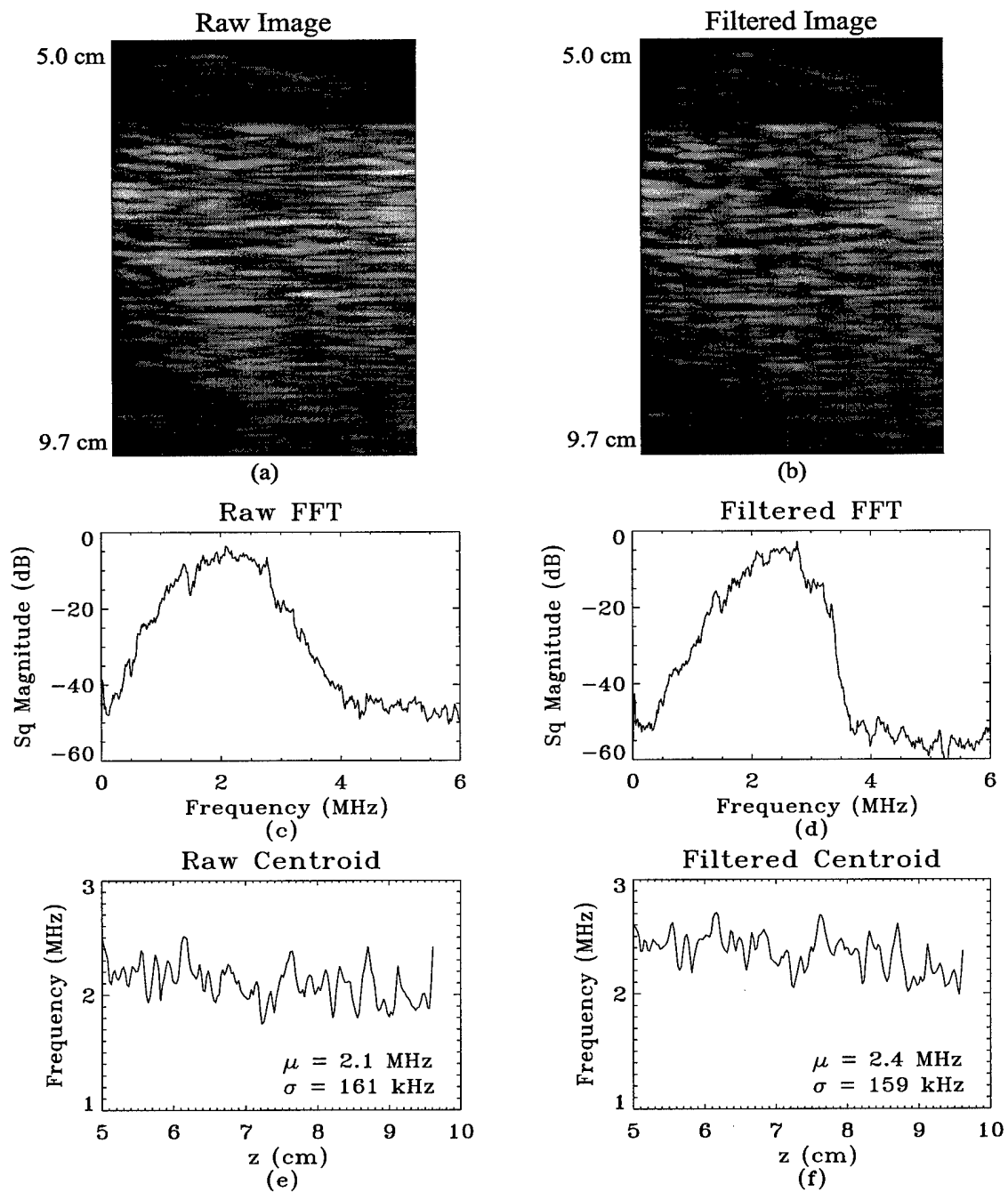


Figure 6.5: Breast on sponge — 2.25 MHz unfocused ($2a = 13$ mm).

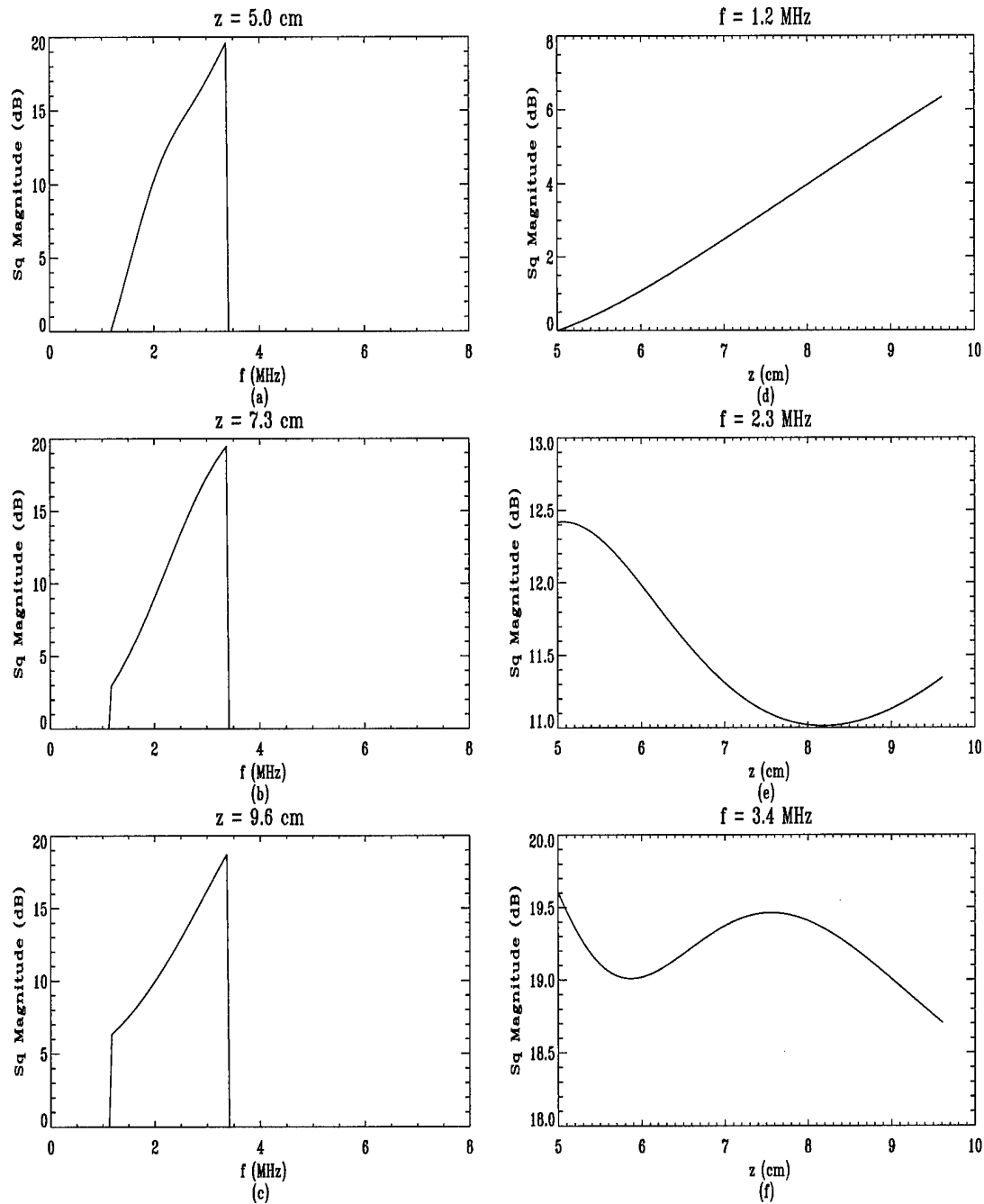


Figure 6.6: Magnitude response — 2.25 MHz unfocused ($2a = 13$ mm).

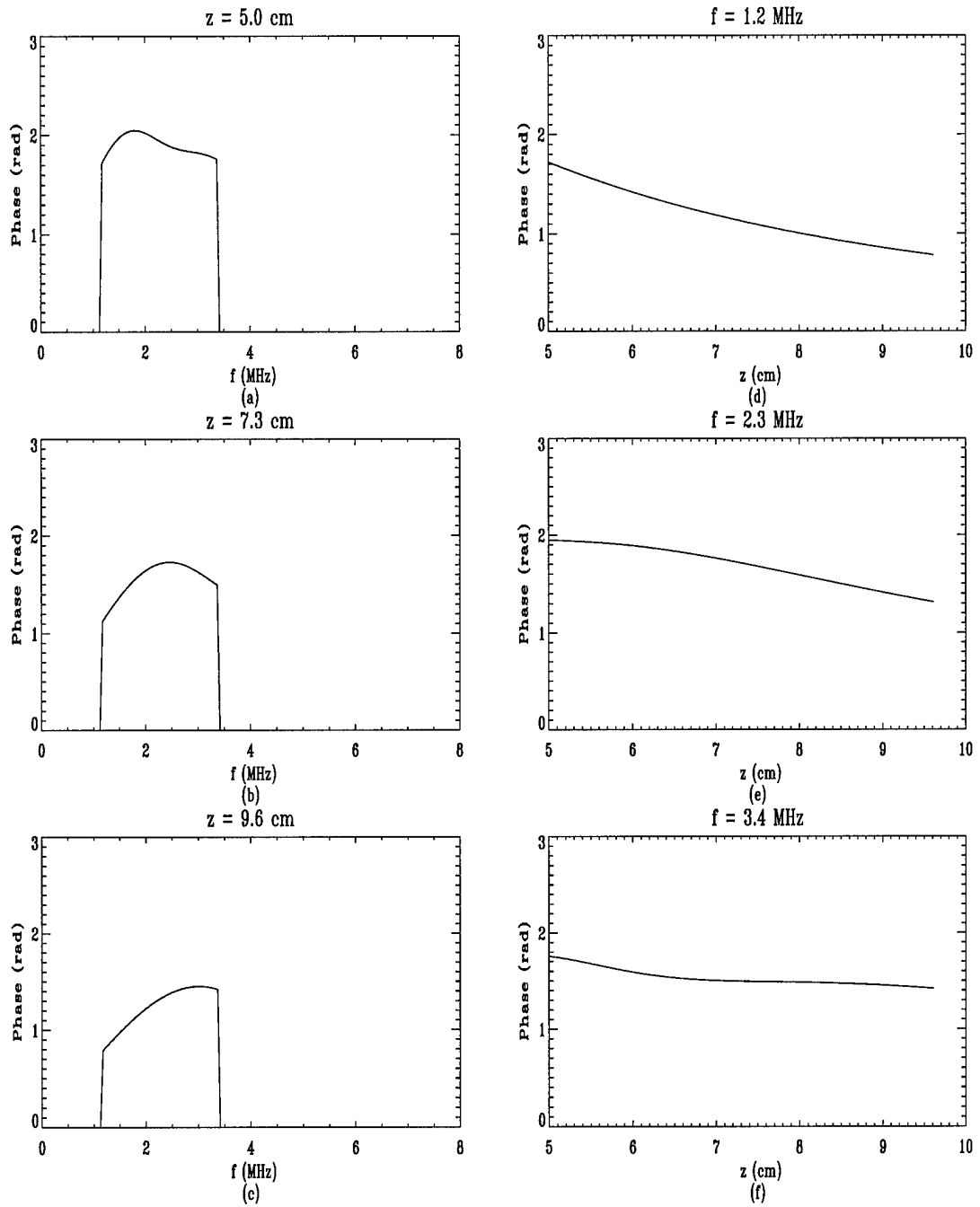


Figure 6.7: Phase response — 2.25 MHz unfocused ($2a = 13$ mm).

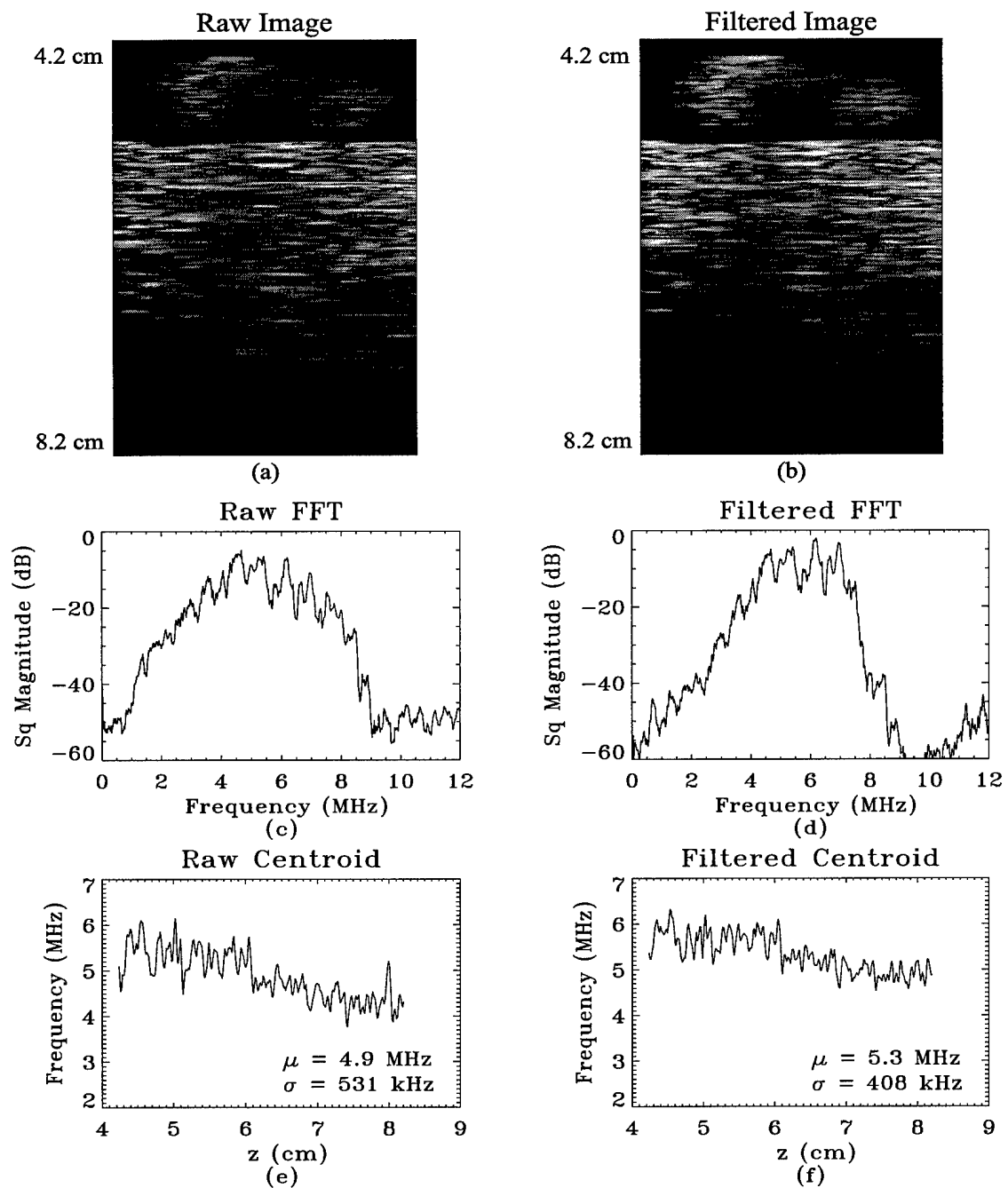


Figure 6.8: Breast on sponge — 5.0 MHz unfocused ($2a = 9.53$ mm).

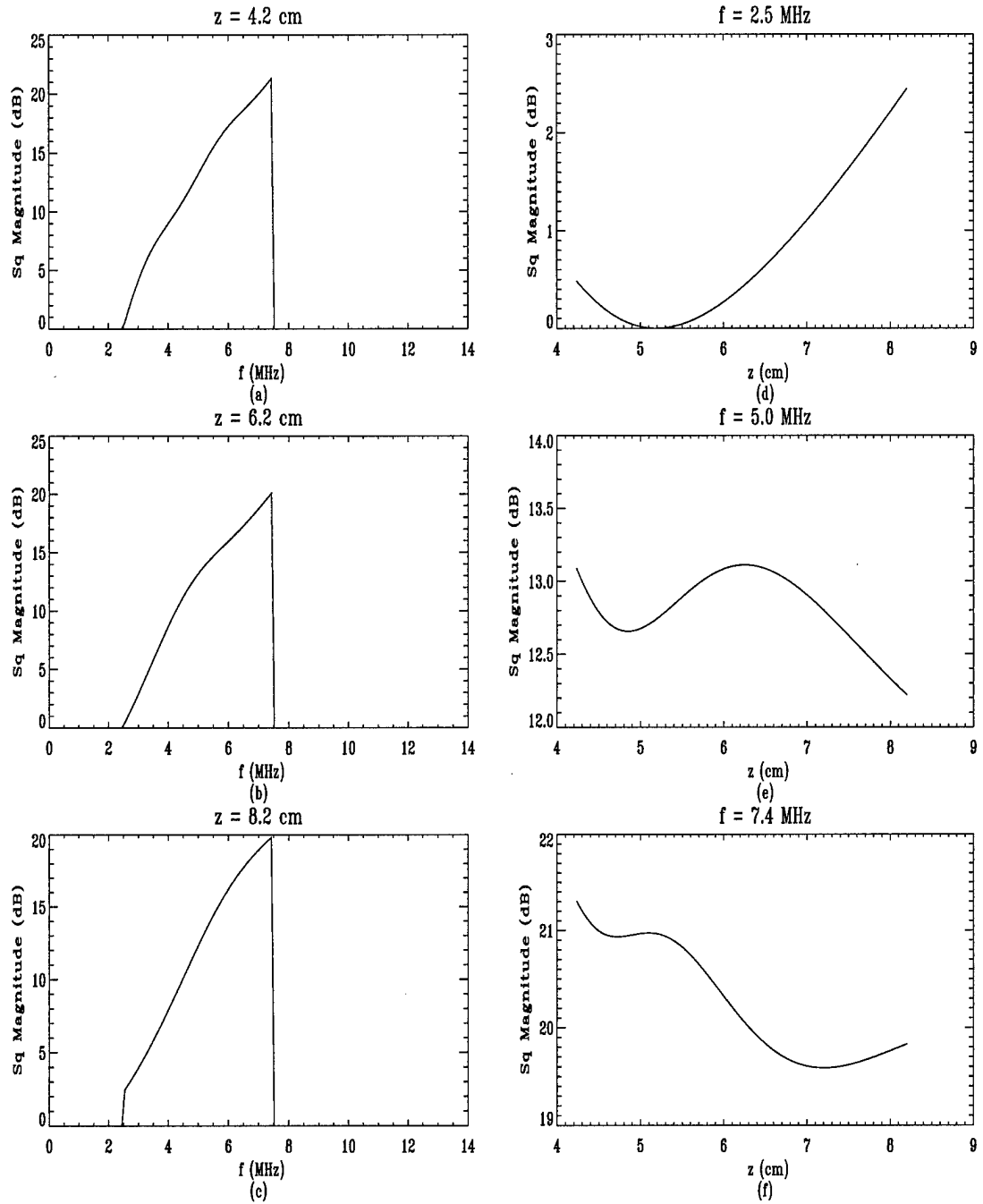


Figure 6.9: Magnitude response — 5.0 MHz unfocused ($2a = 9.53$ mm).

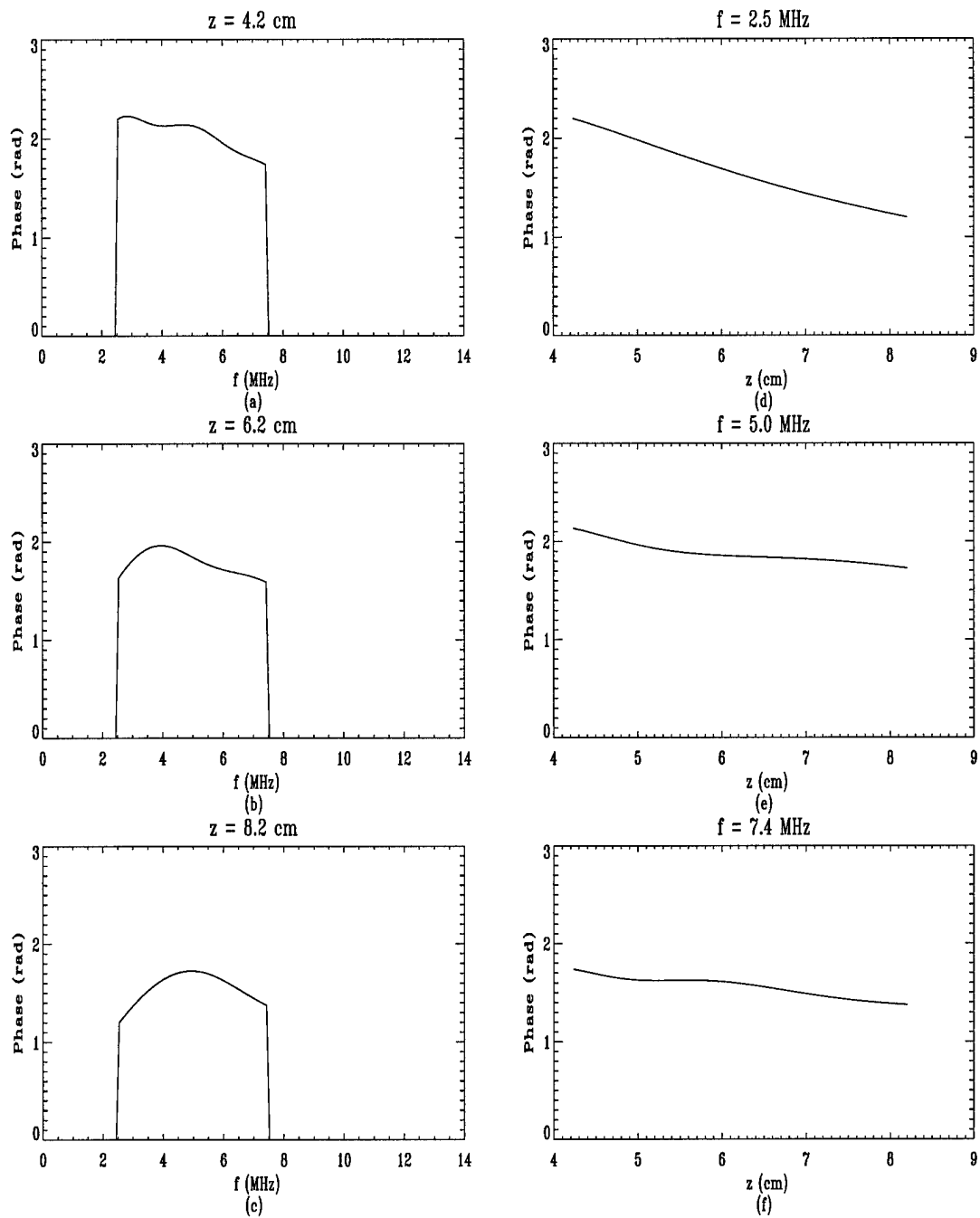


Figure 6.10: Phase response — 5.0 MHz unfocused ($2a = 9.53$ mm).

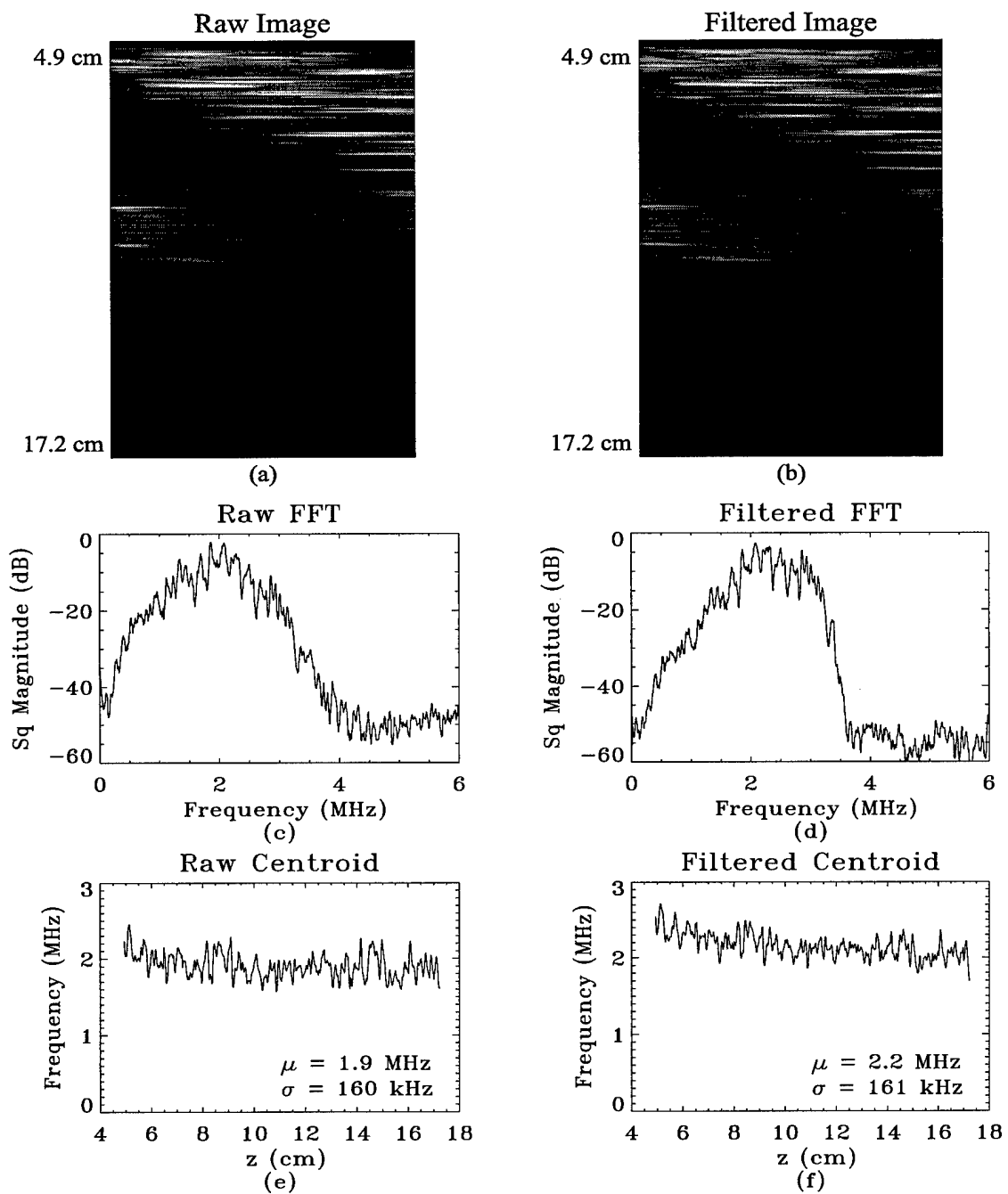


Figure 6.11: Pig liver on sponge — 2.25 MHz unfocused ($2a = 13$ mm).

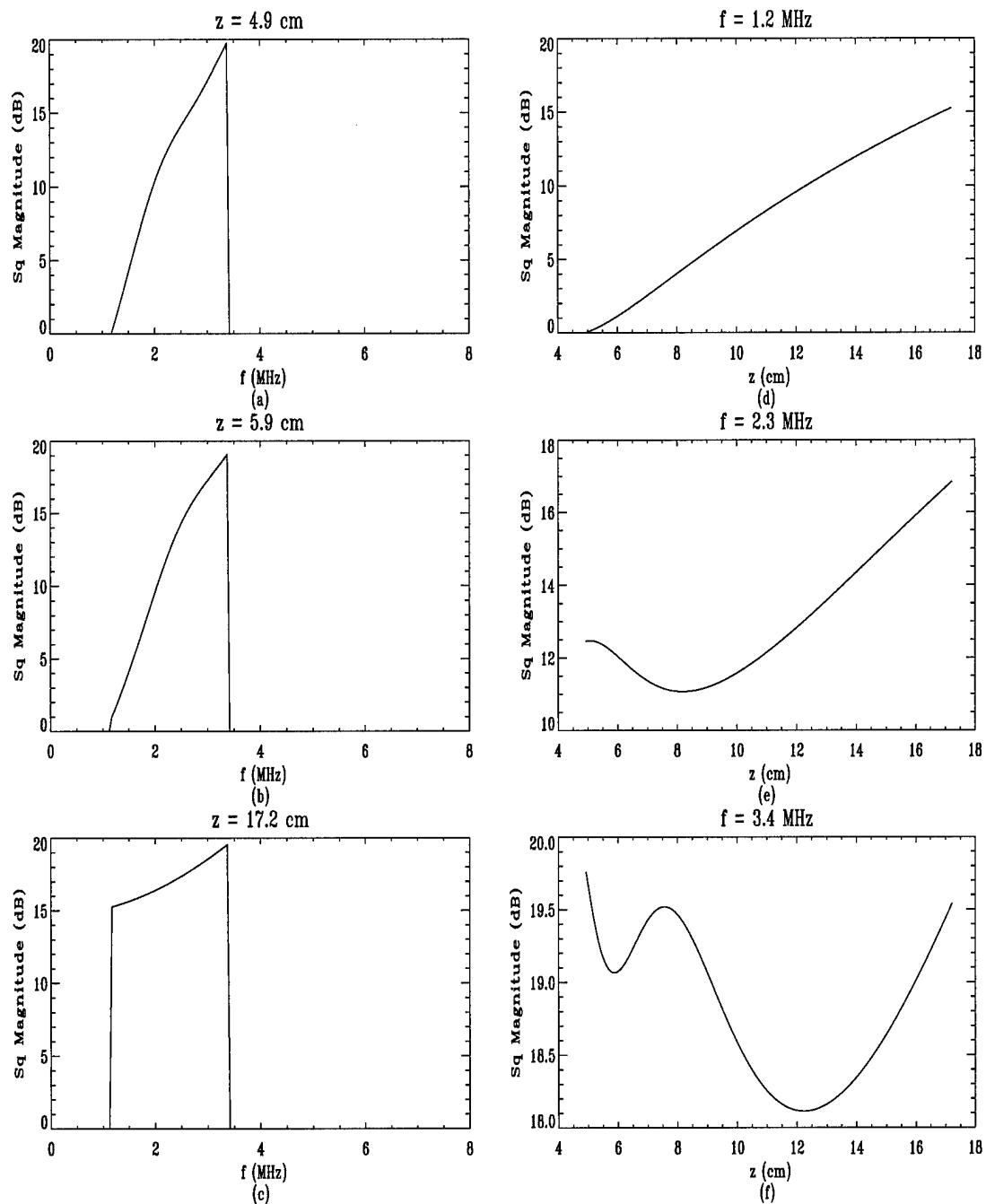


Figure 6.12: Magnitude response — 2.25 MHz unfocused ($2a = 13$ mm).

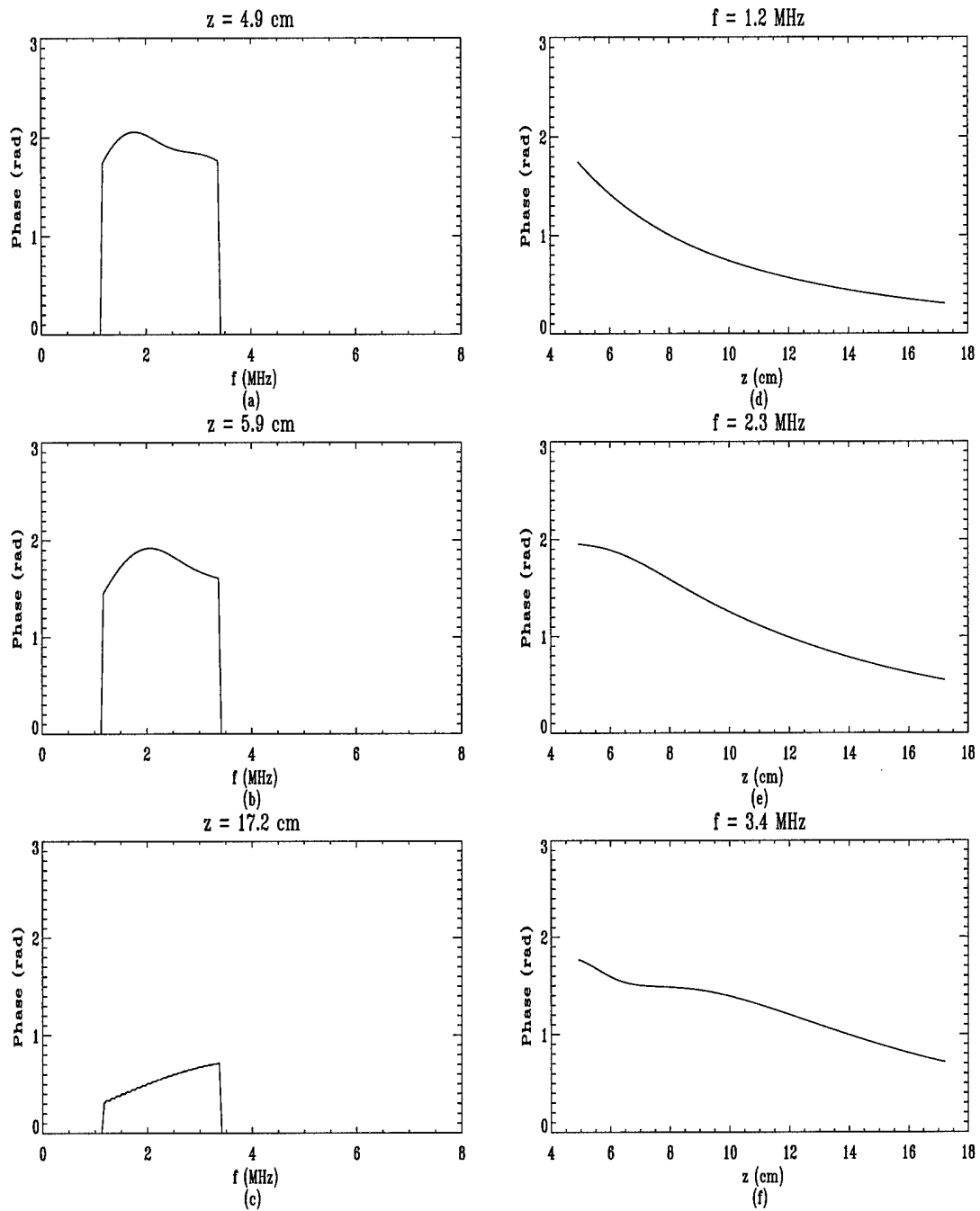


Figure 6.13: Phase response — 2.25 MHz unfocused ($2a = 13$ mm).

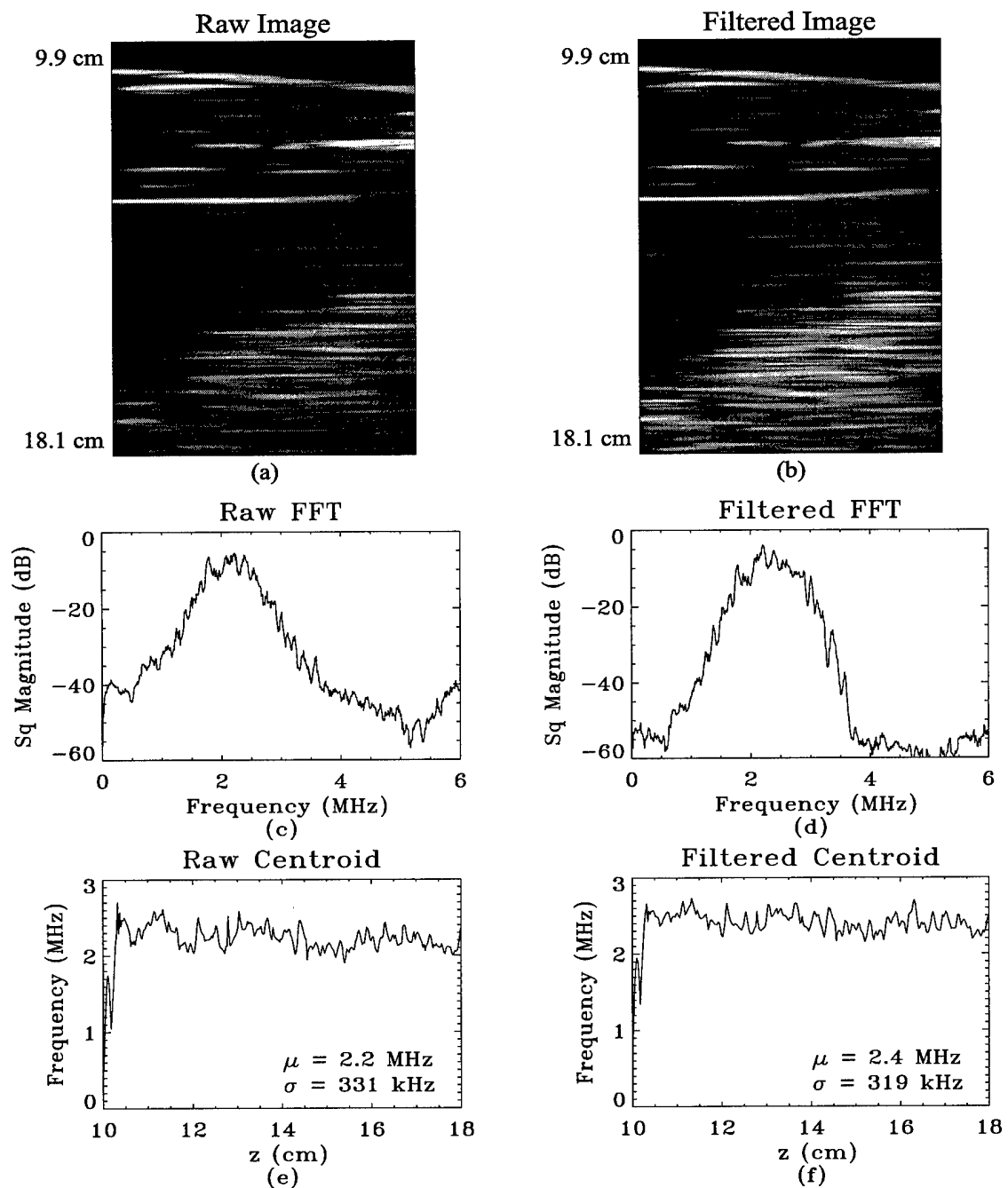


Figure 6.14: Pig liver on sponge — 2.25 MHz long focus ($2a = 13$ mm).

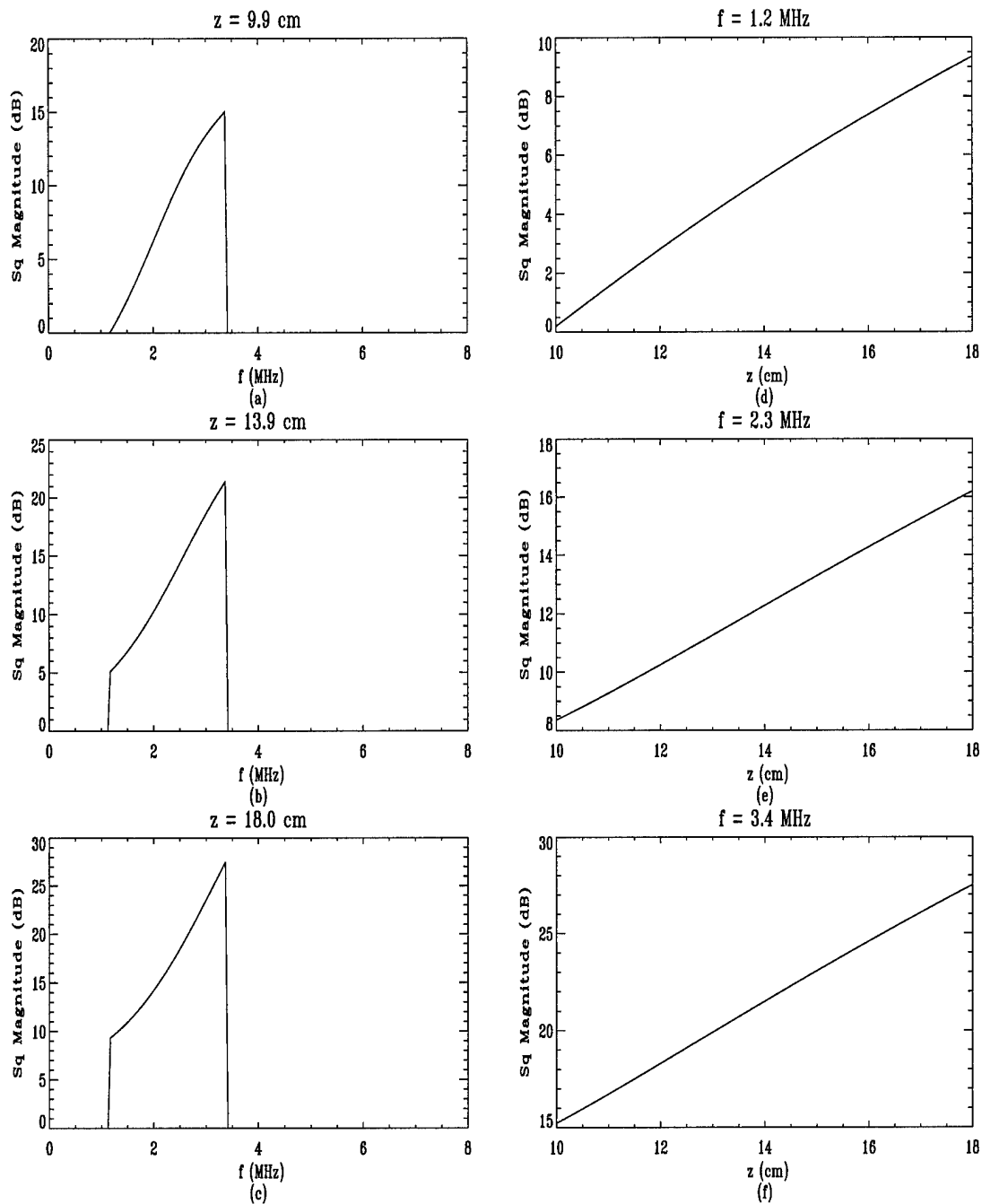


Figure 6.15: Magnitude response — 2.25 MHz long focus ($2a = 13$ mm).

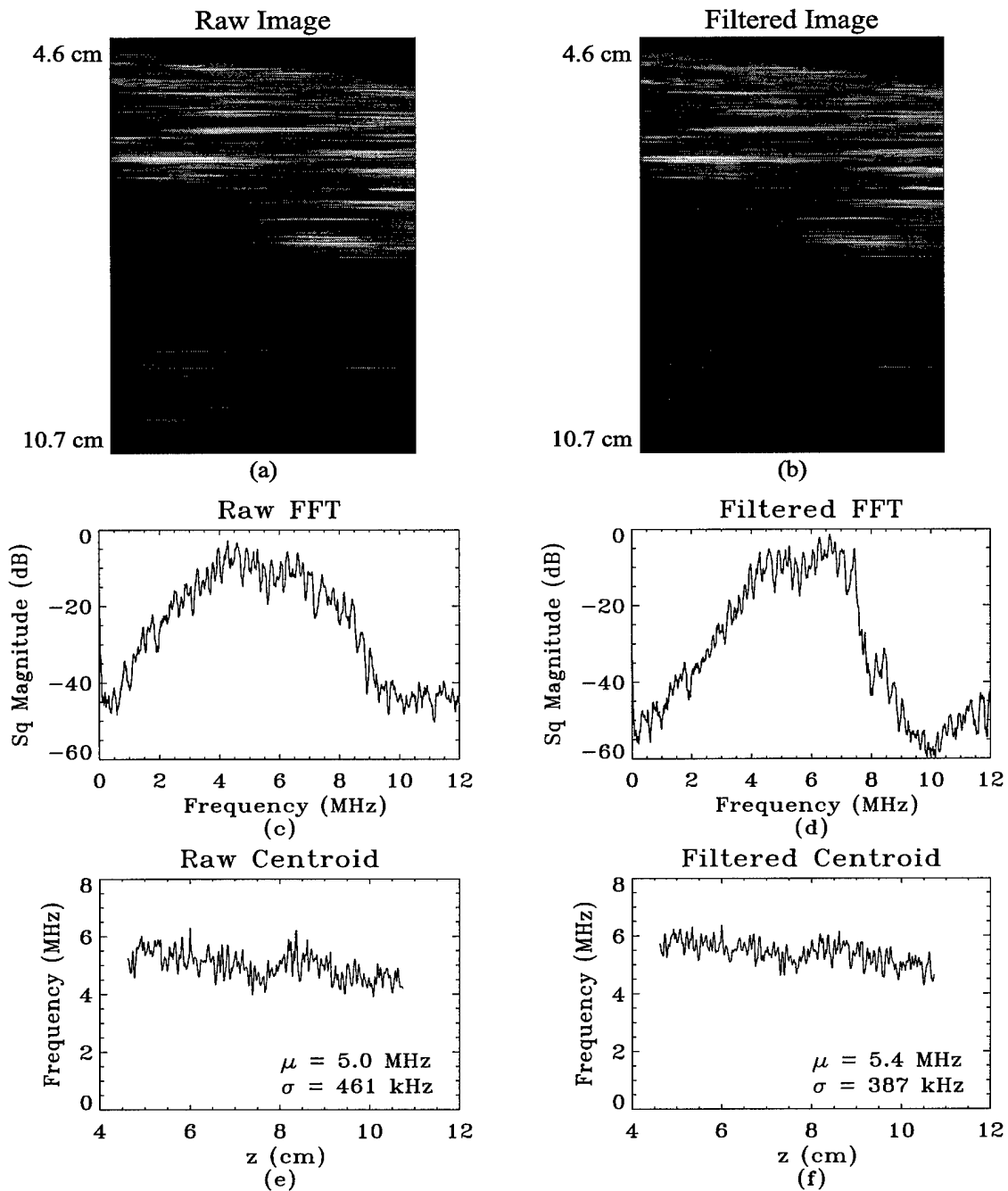


Figure 6.16: Pig liver on sponge — 5.0 MHz unfocused ($2a = 9.53$ mm).

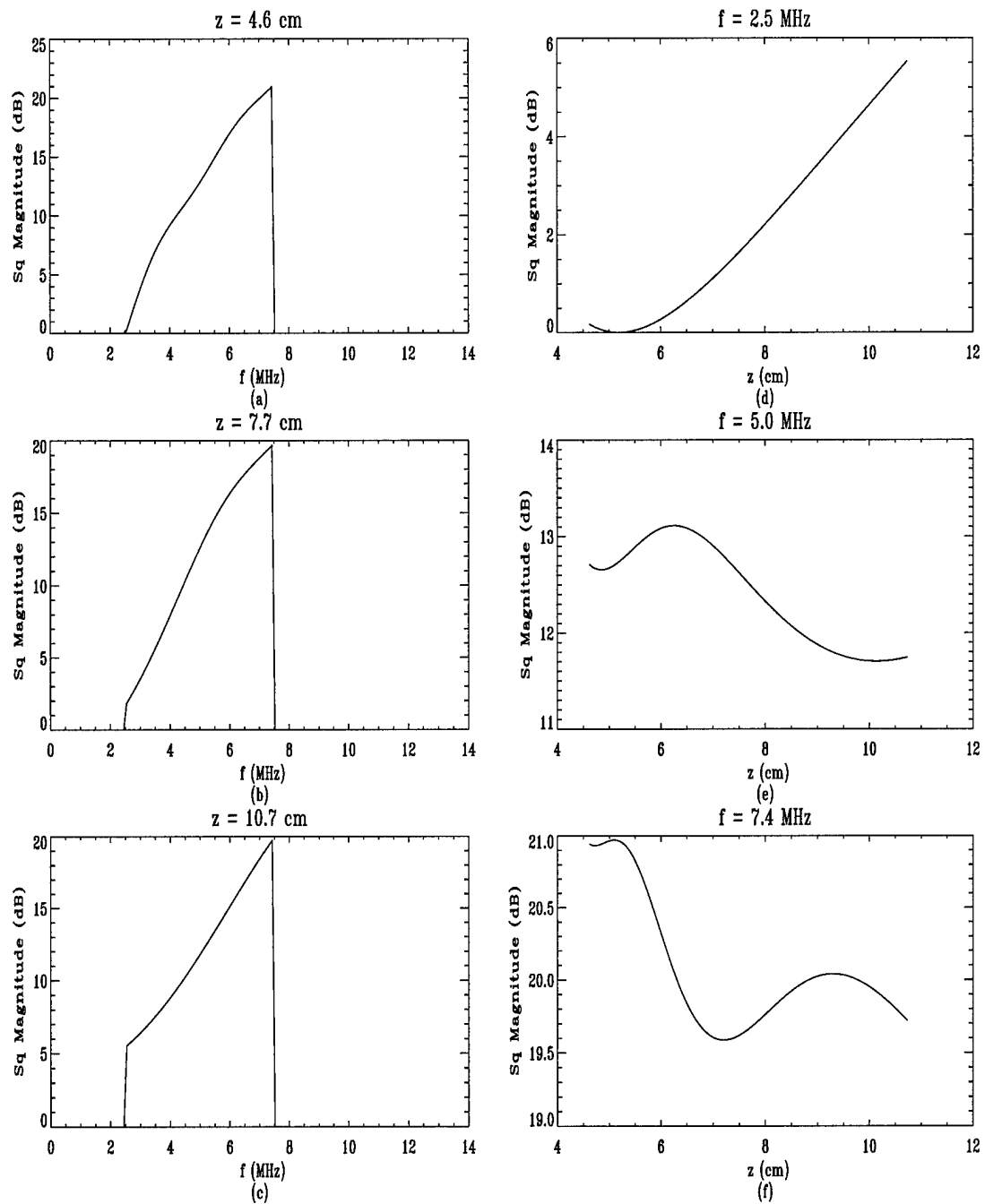


Figure 6.17: Magnitude response — 5.0 MHz unfocused ($2a = 9.53$ mm).

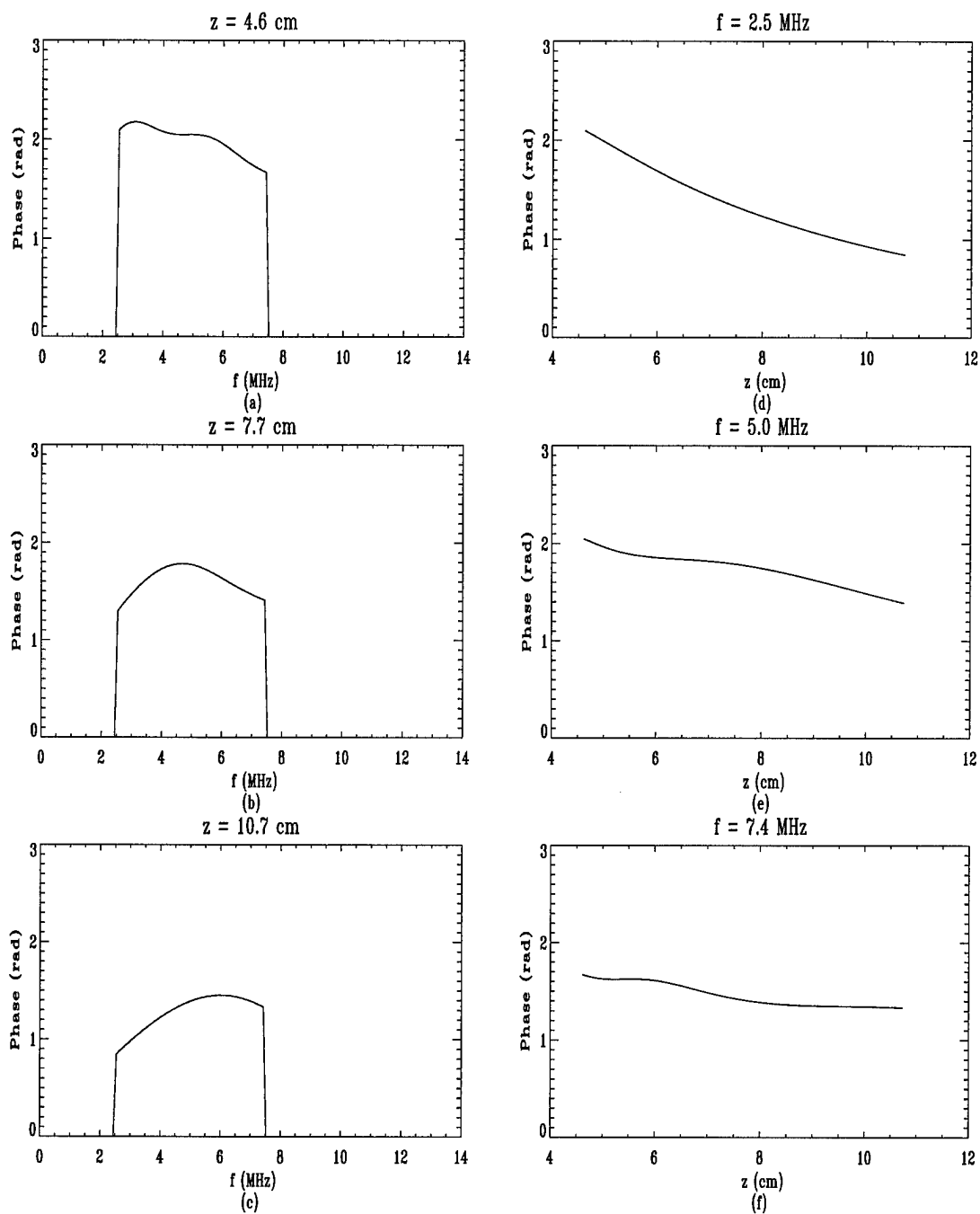


Figure 6.18: Phase response — 5.0 MHz unfocused ($2a = 9.53$ mm).

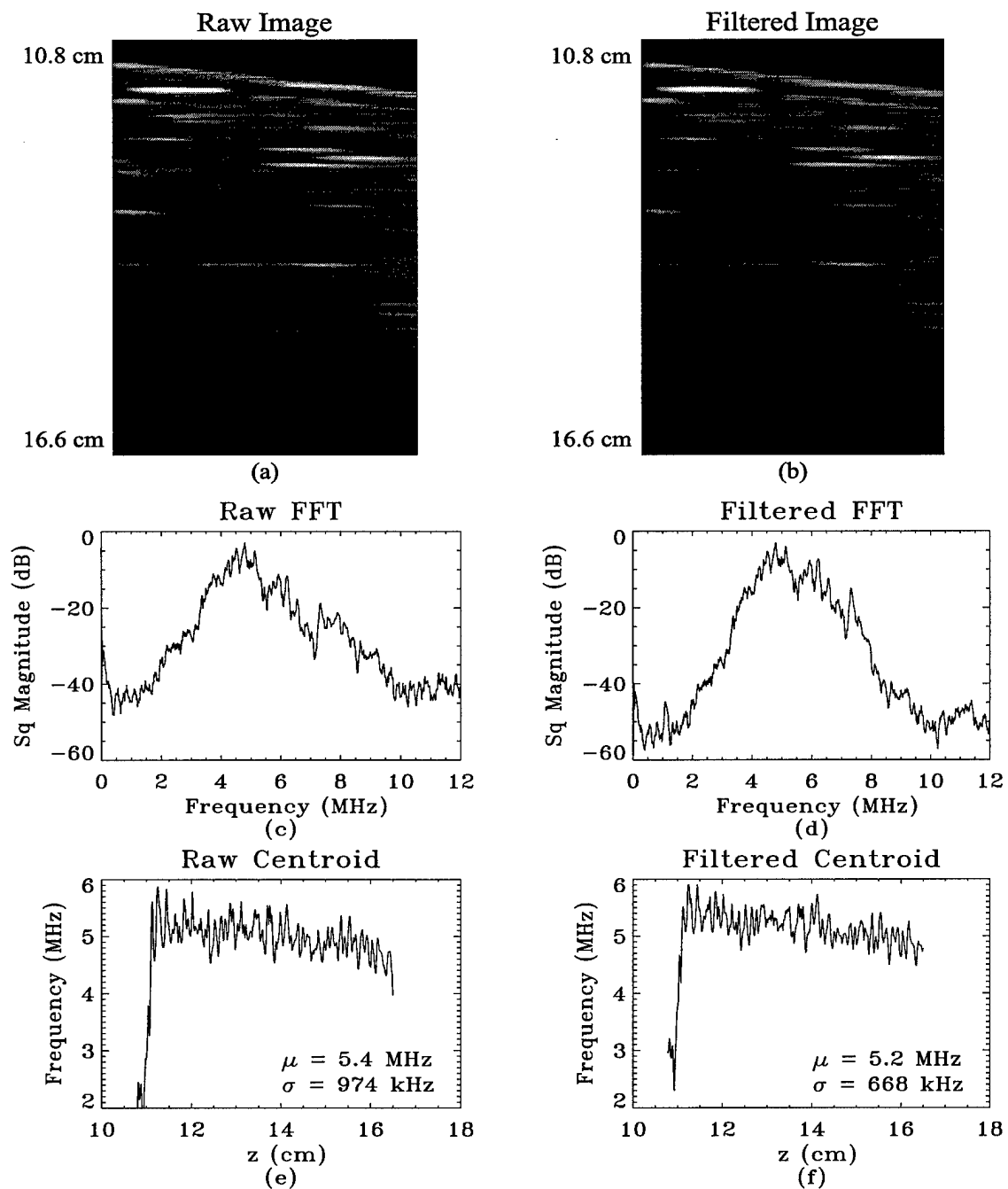


Figure 6.19: Pig liver on sponge — 5.0 MHz long focus ($2a = 13$ mm).

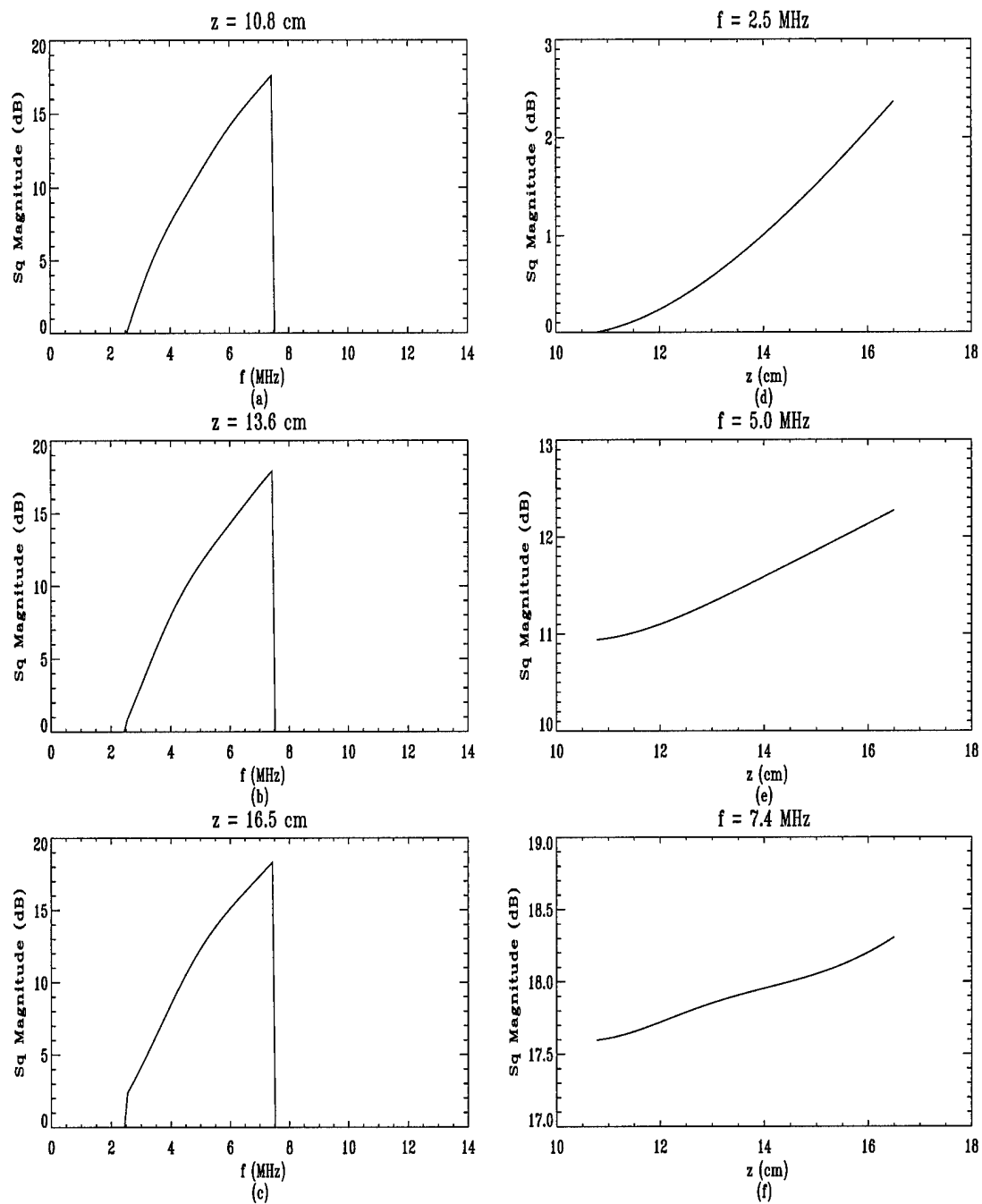


Figure 6.20: Magnitude response — 5.0 MHz long focus ($2a = 13$ mm).

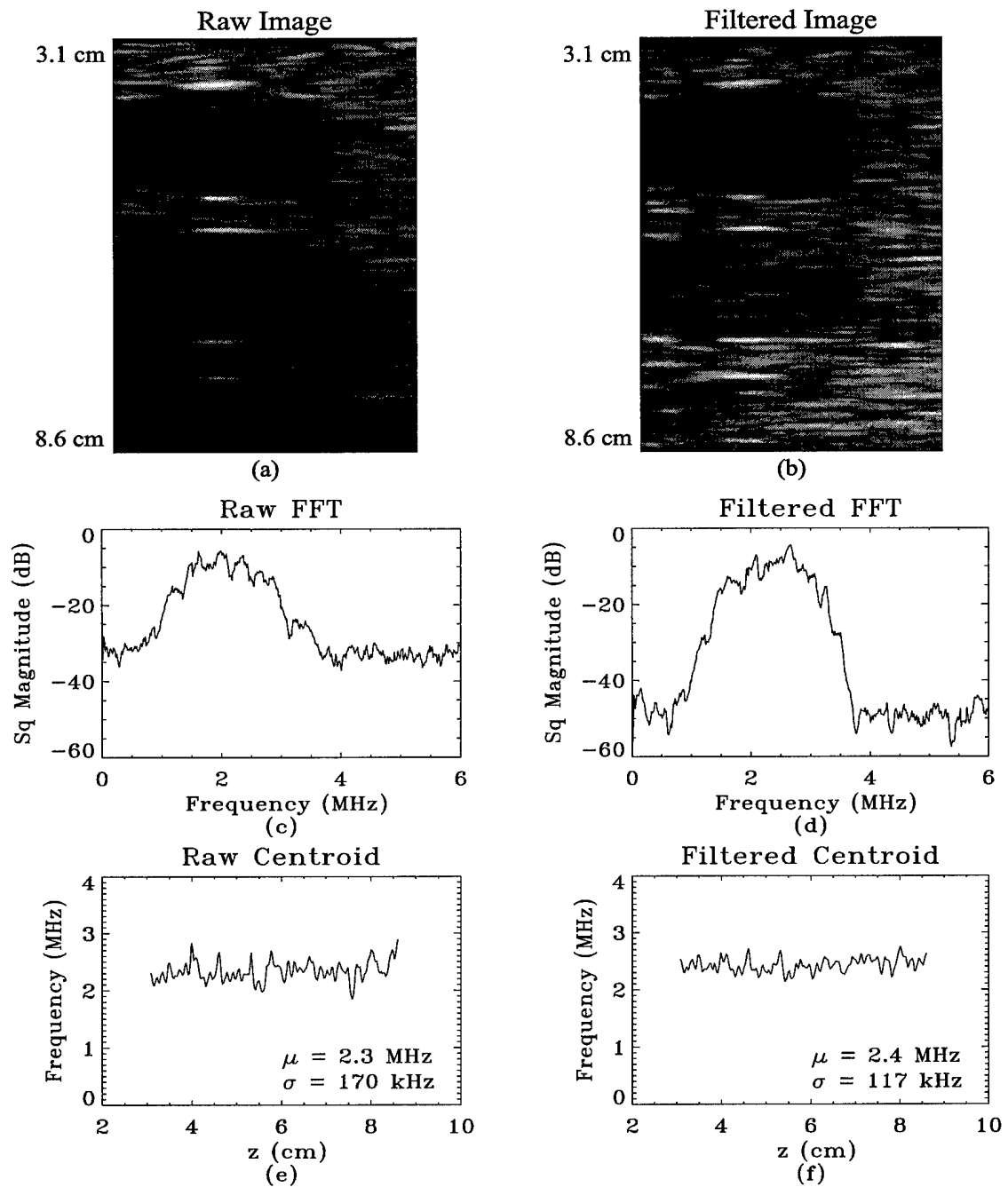


Figure 6.21: Disk phantom — 2.25 MHz medium focus ($2a = 13$ mm).

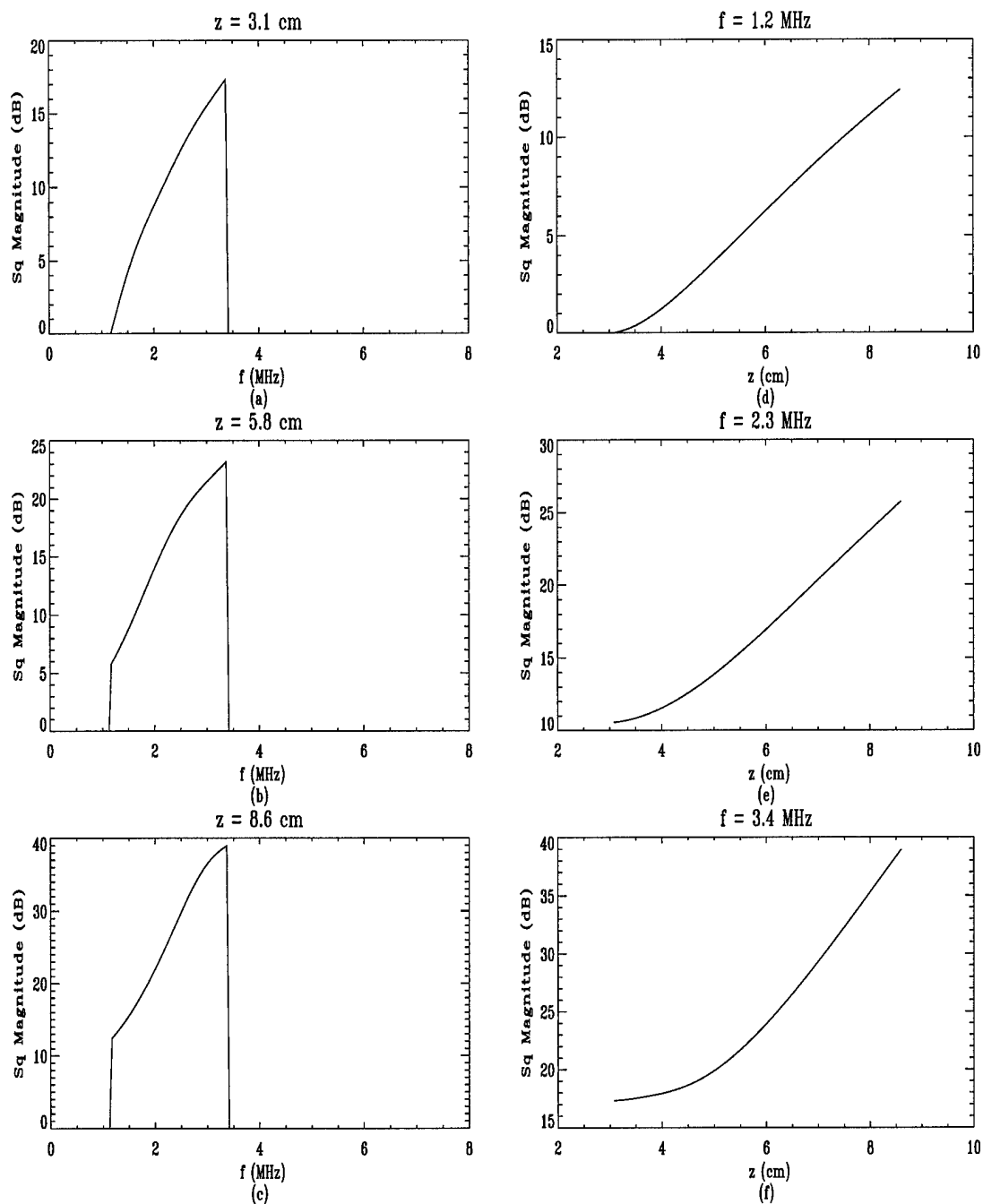


Figure 6.22: Magnitude response — 2.25 MHz medium focus ($2a = 13$ mm).

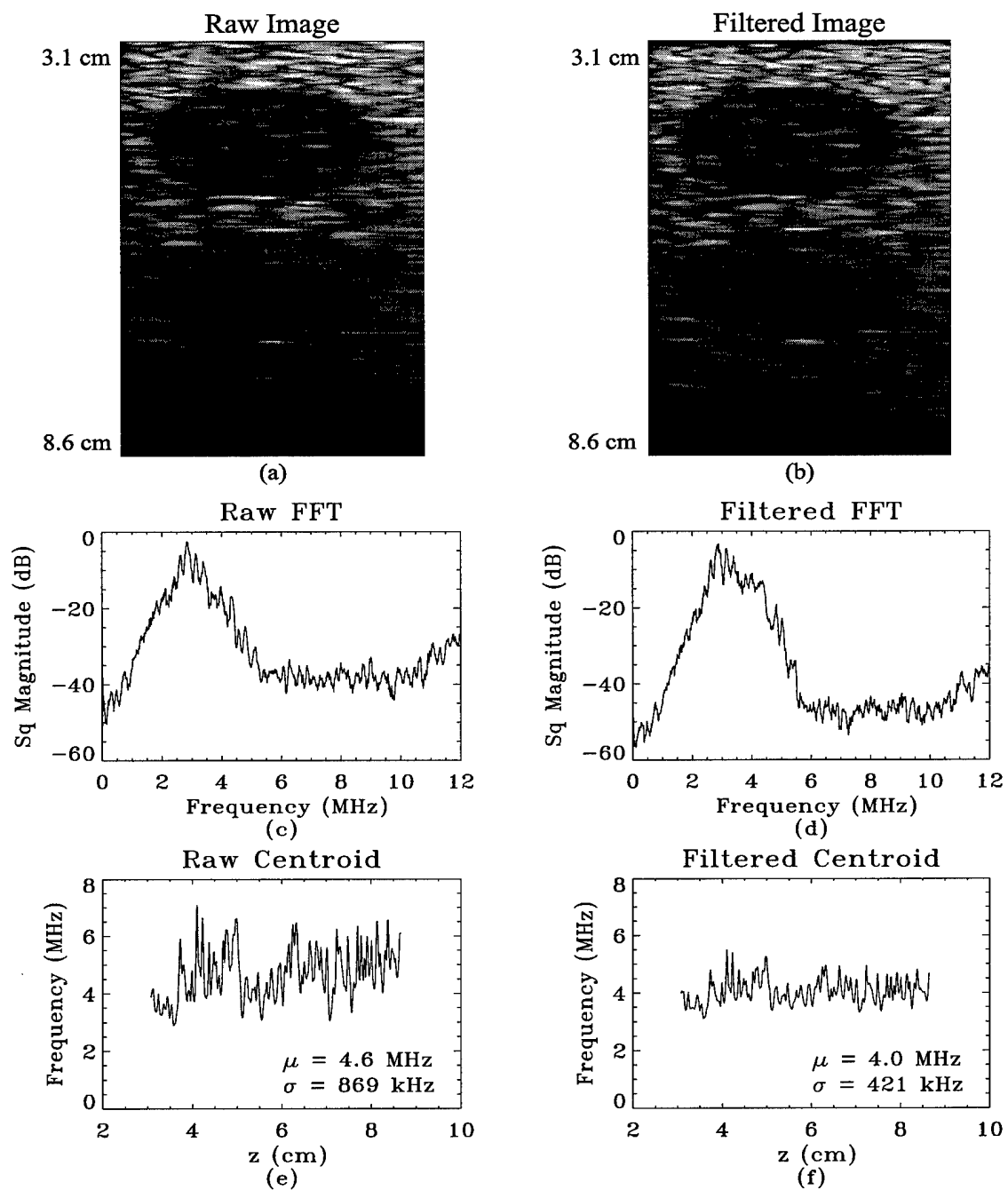


Figure 6.23: Disk phantom — 3.5 MHz medium focus ($2a = 13$ mm).

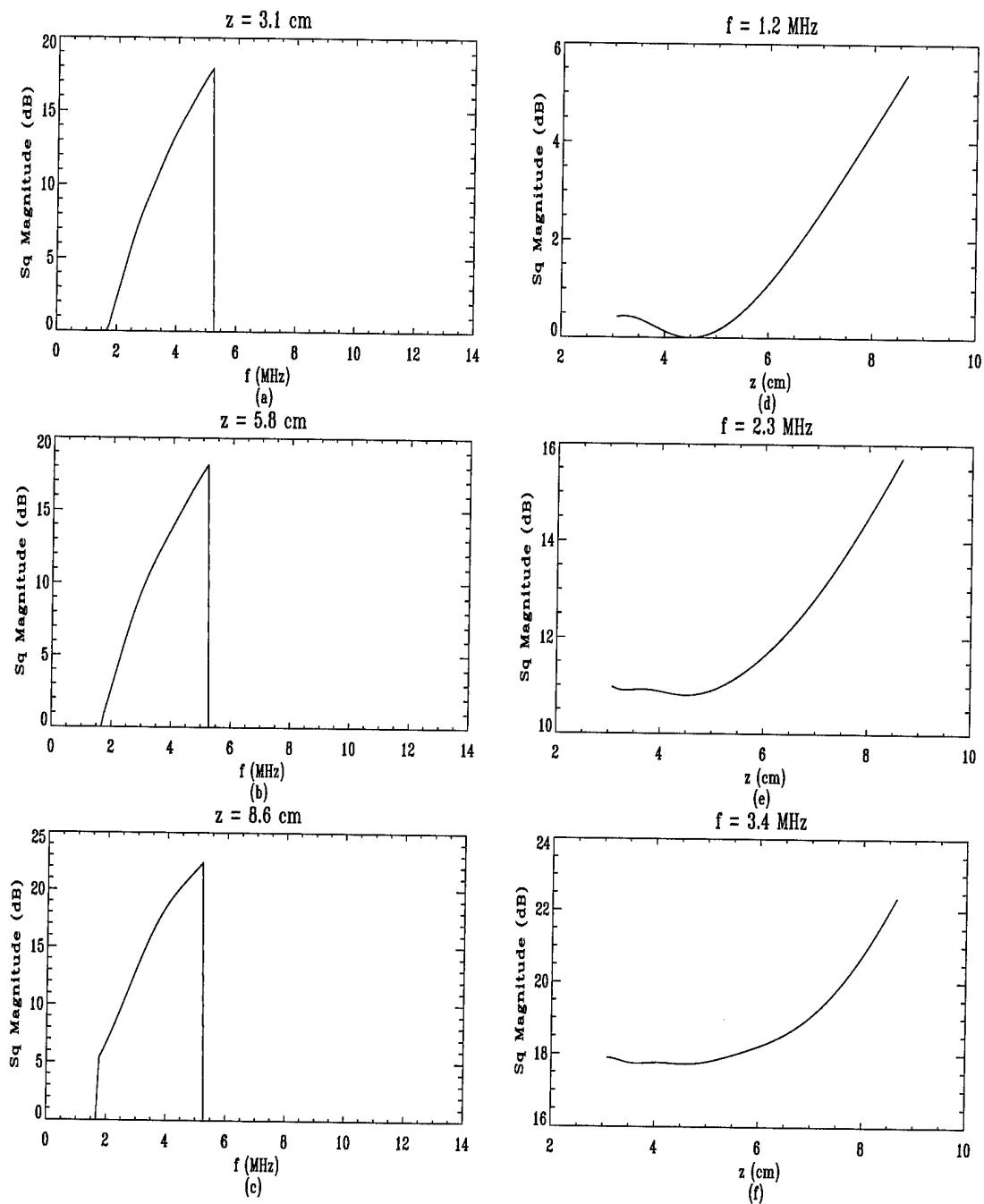


Figure 6.24: Magnitude response — 3.5 MHz medium focus ($2a = 13$ mm).

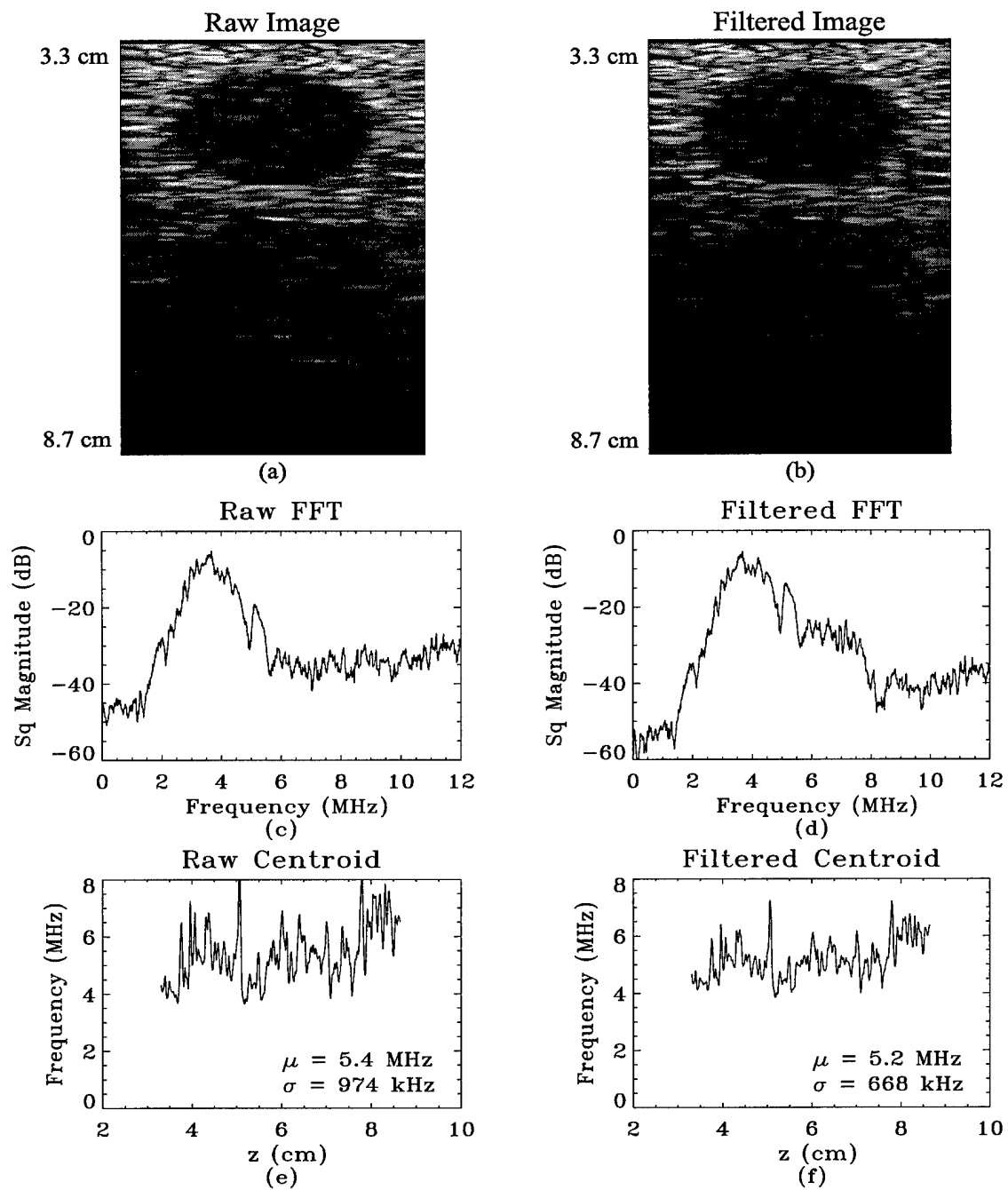


Figure 6.25: Disk phantom — 5.0 MHz medium focus ($2a = 13$ mm).

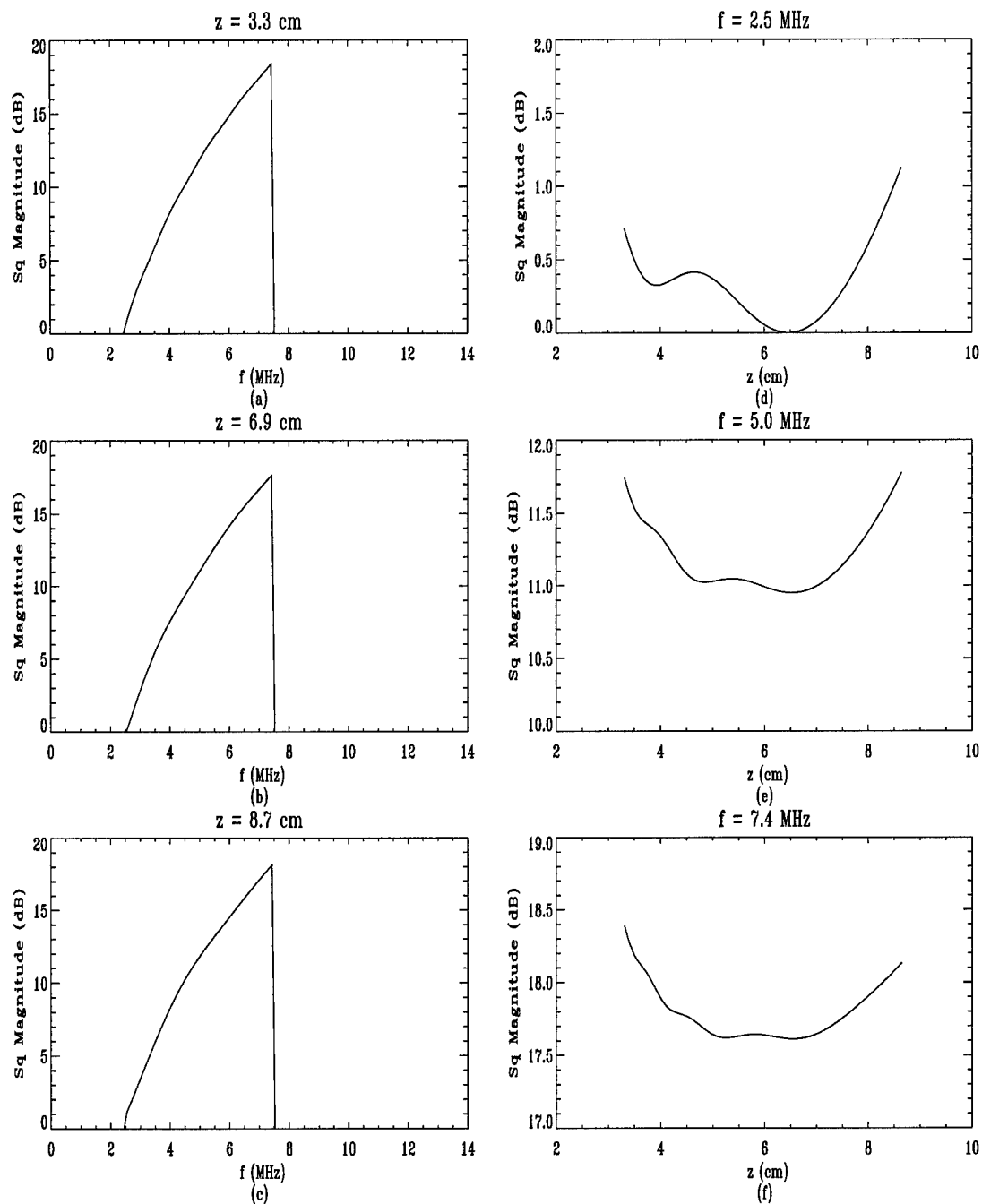


Figure 6.26: Magnitude response — 5.0 MHz medium focus ($2a = 13$ mm).

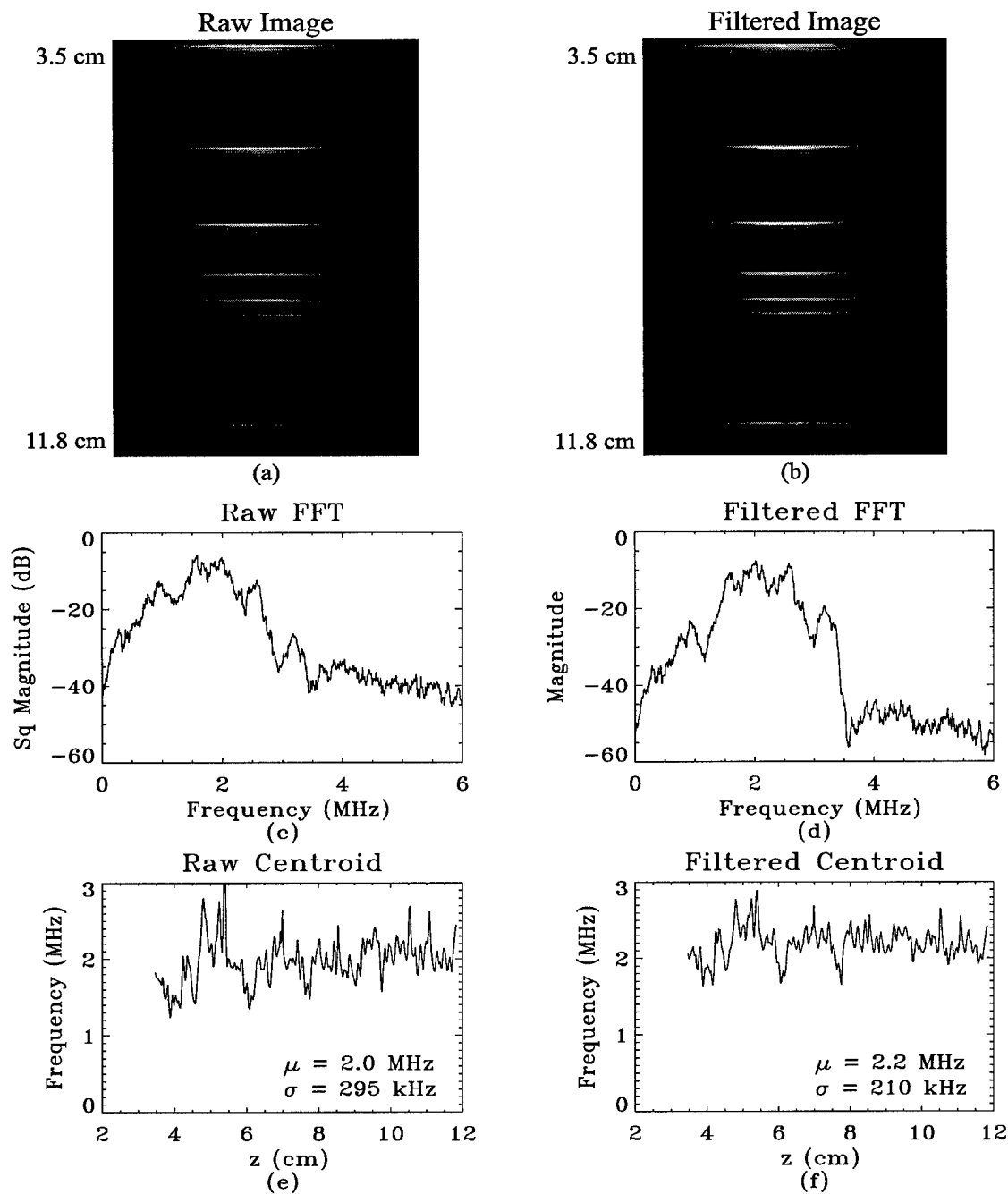


Figure 6.27: Wire targets — 2.25 MHz unfocused ($2a = 13$ mm).

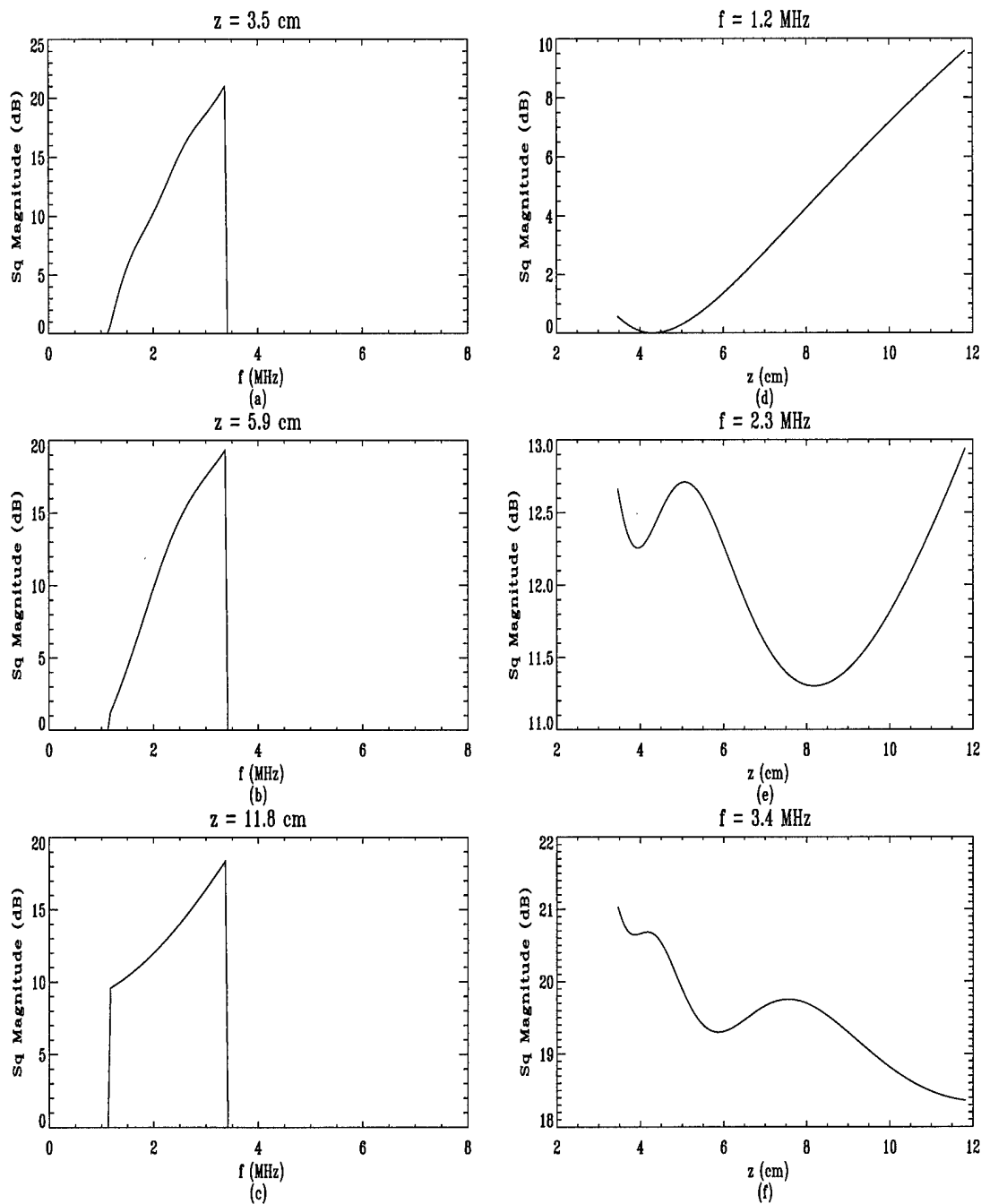


Figure 6.28: Magnitude response — 2.25 MHz unfocused ($2a = 13$ mm).

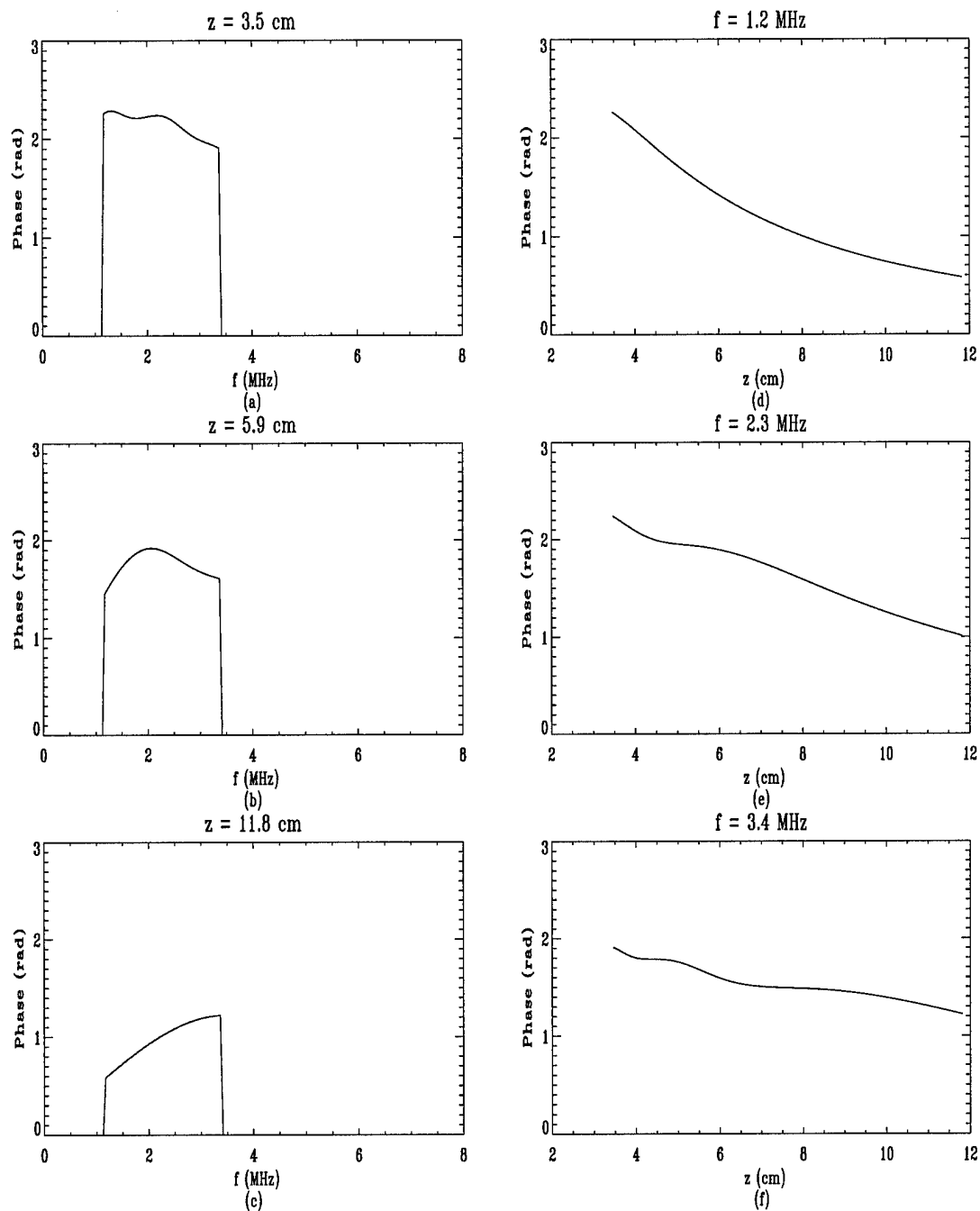


Figure 6.29: Phase response — 2.25 MHz unfocused ($2a = 13$ mm).

Chapter 7

Analytical Investigation

Chapter 3 unified the arccos and Lommel diffraction formulations as an approximate Fourier transform pair. Chapters 4–5 used Lommel’s treatment of Fresnel diffraction to derive closed-form spatially averaged diffraction corrections for one-way and two-way diffraction. The last chapter investigated experimental application of autoconvolution diffraction correction. The analytical investigation in the current chapter demonstrates the predictive power of the proposed unified theory developed and simultaneously ties up some loose ends. The predictive power of the theory is demonstrated in an examination of more subtle aspects of ultrasonic diffraction including mirror-image diffraction, autoconvolution diffraction, and the number of time derivatives necessary in a linear model of ultrasonic reflection imaging. The unified theory developed so far places these aspects of ultrasonic diffraction in new perspective. Taken in its entirety, this chapter presents a new quantitative comparison of the mirror-image and autoconvolution interpretations of two-way diffraction.

Recall the mirror-image interpretation of diffraction claims that results derived for one-way diffraction can be applied to two-way diffraction by simply doubling the distance in the one-way equations. Before this claim can be investigated more fully, it would be wise to re-examine and, where possible, re-validate the closed-form one-way and two-way expressions derived in Chapters 4–5.

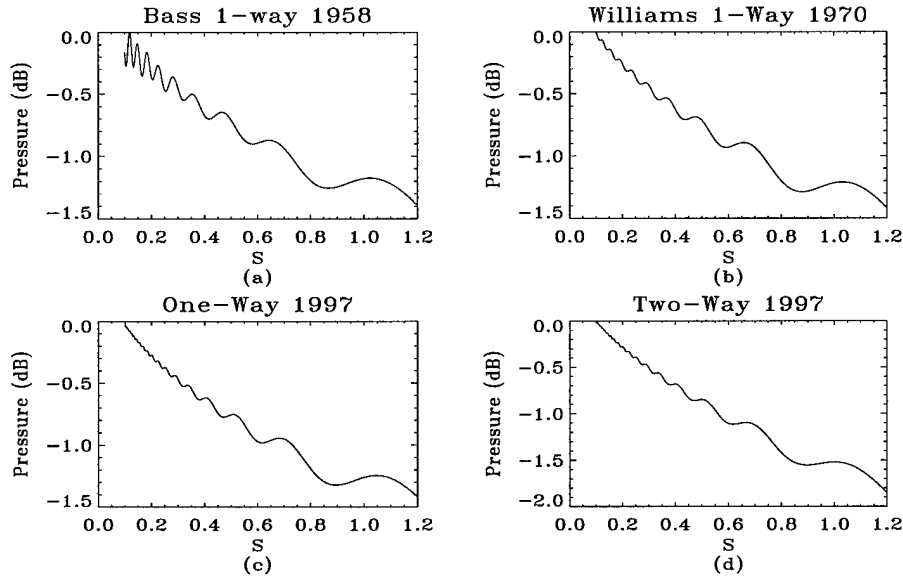


Figure 7.1: Attenuation caused by diffraction as a function of S in the near-field.

7.1 One-way Diffraction

In this section, we re-examine the closed-form frequency-domain expressions in Eq. 4.18, and we are particularly interested in their behavior as a function of the radius of the receiving aperture b . The validity of Eq. 4.18 for $b < a$ has already been demonstrated. Specifically, Section 4.4 showed that Eq. 4.18 approximated the behavior of an on-axis point receiver for the choice of parameter $b = a/1000$. It must be emphasized that the closed-form *spatially averaged* expression captured the salient features of the impulse response predicted by the well-established theory for an on-axis *point* receiver.

The validity of Eq. 4.18 for $b = a$ has already been checked against Eq. 4.5, but it can be double checked against the work done by Bass [5] and Williams [67]. Figs. 7.1–7.2 show spatially averaged one-way diffraction effects for monochromatic excitation plotted as a function of $S = z\lambda/a^2$. The parameters used to compute the data shown in the plots are the same as in Bass’s 1958 article: $c = 1200$ m/s, $a = 1$ cm, and $f = 0.956$ MHz. The data were obtained from (i) Bass’s 1958 equation [5, Eq. (14)], (ii) Williams’

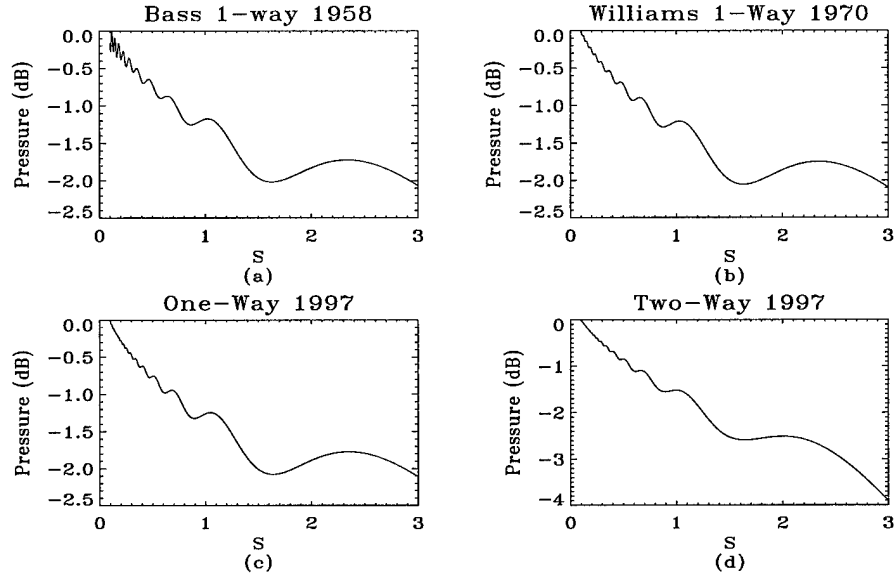


Figure 7.2: Attenuation caused by diffraction as a function of S in both the near-field and far-field.

1970 equation [67, Eq. (6)], and (iii) Eq. 4.11. Note that Williams [67, p. 286] corrected two typos in Bass's 1958 equation. The oscillatory behavior of Bass's result at low S is due to the small number of terms used in his equation. The overall results, however, show excellent agreement, and the plots confirm the well-established fact that attenuation due to diffraction increases with depth z . Thus, we have confidence in the validity of Eq. 4.11. The monochromatic two-way results labeled "Two-Way 1997" in the figures are included for comparison and will be discussed in the next section.

The validity of Eq. 4.18 for $b > a$ can be checked by considering the total pressure impinging on an infinite receiver; this leads to a theoretical result and new insight. Multiplying Eq. 4.18 for $b > a$ by πb^2 and some further algebra yields

$$(\pi b^2) \langle \hat{H}_1(z, \omega) \rangle_b = -j \frac{\pi a^2}{k} e^{-jkz} - 2ze^{-j(kz + \frac{\pi}{2} + \frac{v_b^2}{2u})} [X_2(u, v_b) - jX_1(u, v_b)], \quad (7.1)$$

where $u = ka^2/z$ and $v_b = kab/z$ as before. Letting b approach infinity yields

$$\lim_{b \rightarrow \infty} (\pi b^2) \langle \hat{H}_1(z, \omega) \rangle_b = -j \frac{\pi a^2}{k} e^{-jkz}. \quad (7.2)$$

The same result can be obtained by spatially integrating the Lommel diffraction formulation of Eq. 3.6 directly. Doing so yields

$$\lim_{b \rightarrow \infty} (\pi b^2) \langle \hat{H}_1(z, \omega) \rangle_b = \lim_{b \rightarrow \infty} 2\pi \int_0^b \hat{H}_1(\rho, z, \omega) \rho d\rho \quad (7.3)$$

where the upper limit of infinity is not problematic because of the rapidly converging Lommel functions in the integrand. Eq. 7.2 can be obtained from Eq. 7.3 with the help of Watson [63, p. 541], Wheelon [65, Eq. 1.608 and Eq. 1.610, pp. 76–77], and Euler’s formula.

At any rate, the closed-form result in Eq. 7.2 is the same as that reported by Williams in [67, Eq. 40] for monochromatic diffraction with a theoretically infinite receiver. If Eq. 7.2 is used to calculate total maximum pressure (Section 3.1), it yields the pressure, $c\rho\pi a^2 e^{-jkz}$, “produced by a section of area πa^2 cut out of a plane wave that has the same particle velocity, [unity in this case], as does the piston source. [67, p.289].” In essence, the magnitude of the total maximum pressure detected by the infinite receiver is the same at all z -planes. No pressure/energy is lost because (i) the receiver is infinite and (ii) no loss mechanism has been introduced into the theory. In this case, diffraction introduces only a depth-dependent phase shift via the e^{-jkz} term.

Further insight can be gained by examining Eq. 7.1 and Eq. 7.2 more closely. Note that the first term in Eq. 7.1 is identical to right-hand side of Eq. 7.2. Thus, the first term in Eq. 7.1 represents the infinite-receiver solution, and the second term represents the influence of diffraction [5]. Similar observations can be made about Eqs. 4.10–4.11. Further, the $k = \omega/c$ in the denominator of the infinite-receiver solution of Eq. 7.2 indicates that one-way diffraction is dominated by a $1/f$ lowpass filtering effect. This claim is consistent with the results shown in Figs. 4.5(c)-(d) where the dotted line in each graph shows the squared-magnitude (dB) of $1/f$ with DC removed. Recall Fig. 4.5 was plotted with the parameter $b = a$.

Consider a finite receiver with radius $b = a$ in terms of the beam pattern of a transmitter with radius a . Close in to the transducer, the beam is concentrated in a region bounded by the dimensions of the transmitter. Thus, a finite receiver with radius $b = a$, as

in Fig. 5.4(c), placed close to the transmitter detects most of the transmitted energy because the receiver has the same dimensions as the transmitter. In effect, it is indistinguishable from an infinite receiver, and the data in Fig. 4.5(c) show excellent agreement. Farther out from the transmitter, the beam begins to spread or diffract. A finite receiver placed further away from the transmitter will no longer have the same effect as an infinite receiver. Thus, the data in Fig. 4.5(c) show poor agreement. This insight is further testimony to the practical and theoretical value of the proposed unified theory of spatially averaged diffraction correction.

7.2 Two-Way Diffraction

In this section, the two interpretations of two-way diffraction are considered. First, mirror-image diffraction is briefly discussed. Next, autoconvolution diffraction is discussed in more detail. In particular, the validity of Eqs. 5.13–5.15 is re-examined and new insights are developed. Finally, the mirror-image and autoconvolution interpretations of two-way diffraction are compared.

7.2.1 Mirror-Image Diffraction

The mirror-image interpretation of diffraction claims that results derived for one-way diffraction can be applied to two-way diffraction by simply doubling the distance z in the one-way equations. In the framework of the proposed unified theory, the mirror-image interpretation is

$$\langle h_2(z, t) \rangle_b = \langle h_1(2z, t) \rangle_b \quad (7.4)$$

if Eq. 4.5 is used, or

$$\langle \hat{h}_2(z, t) \rangle_b = \langle \hat{h}_1(2z, t) \rangle_b \quad (7.5)$$

if Eq. 4.18 is used. Note that Eq. 7.4 is based on the arccos diffraction formulation while Eq. 7.5 is based on the Lommel diffraction formulation and that $2z$ appears in both

equations. Since we have already established the depth-dependent time scaling inherent in all the one-way results developed so far (Fig. 3.3 and Figs 4.3–4.7), we can say that the mirror-image interpretation of two-way diffraction is a time-scaled version of one-way diffraction where time is compressed by a factor of two.

7.2.2 Autoconvolution Diffraction

In this section, the closed-form frequency-domain expressions in Eqs. 5.13–5.15 are re-examined; we are particularly interested in their behavior as a function of b , the radius of the reflecting disk. Additionally, we are interested in tying up a loose end, namely the verification of Eqs. 5.13–5.15 for focused transducers. The validity of Eq. 5.13 has been demonstrated already for an unfocused transducer. Specifically, Section 5.4 showed that Eq. 5.13 with $b = a/1000$ approximated the behavior of an on-axis point scatterer. It must be emphasized that the closed-form *spatially averaged* expression in conjunction with the assumption of minimum phase captured the salient features of the impulse response predicted by the well-established theory for an on-axis *point* scatterer.

Figs. 7.3–7.14 validate the theory for both focused and unfocused transducers in a magnitude-squared sense; the figures are grouped at the end of the chapter for convenience. The figures show attenuation due to diffraction (the diffraction filter) as a function of frequency f and depth z for different values of the parameter b and for different types of focusing (Section 6.1). Relevant parameters are annotated in the figures.

As before, the speed of sound was set at $c = 1540$ m/s, and piston diameters were set at $2a = 13$ mm. The transducers were assumed to have an infinitely broadband response, and the excitation was assumed to be an impulse. The sampling frequency was set at $f_S = 36$ MHz; thus, the Nyquist frequency was 18 MHz. The annotation $f = 2.25$ in the plots is a reminder that sampling rate was set based on 2X oversampling of real piston transducer with $f_c = 2.25$ MHz and an upper frequency of 4.5 MHz.

Understanding the figures requires some explanation; for the purposes of this discussion, $Z = a^2 f_c / c$ is taken as the focal point for an unfocused transducer (Section 3.3).

Consider the discussion about conservation of energy in terms of a disk with some finite radius b (Section 6.1); the disk is free to move along the z -axis. For a disk of fixed radius b , the theory predicts that the reflected energy received by the transducer peaks when the disk is near focus and drops off as the disk is moved away from the focus. Thus, the attenuation due to diffraction will be minimized near the focus of the transducer. Figs. 7.3–7.10 confirm the prediction quite nicely. For a fixed depth z , the attenuation due to diffraction should decrease as the radius b of the reflecting disk is increased because the disk will reflect more energy. Again, Figs. 7.3–7.10 confirm this prediction quite nicely.

The previous discussion considered a disk with some finite radius. A theoretical result and new physical insight can be gained by considering Eq. 5.15 and Fig. 5.1 in terms of an infinite disk and the total energy it reflects back to a transducer. Multiplying Eq. 5.15 by πa^2 produces

$$(\pi a^2) \langle \hat{H}_2(z, \omega) \rangle_b \approx \left(\frac{\pi a^2}{k^2} - \frac{\pi a^2}{k^2} \sum_{s=0}^{\infty} \frac{(-1)^s}{2s+1} \left(\frac{u}{v_b} \right)^{2s} Q_{2s}(v_b) \right). \quad (7.6)$$

Letting b approach infinity yields

$$\lim_{b \rightarrow \infty} (\pi a^2) \langle \hat{H}_2(z, \omega) \rangle_b = \frac{\pi a^2}{k^2}. \quad (7.7)$$

Eq. 7.7 can be used to calculate the magnitude of the total maximum pressure (Section 3.1) reflected by infinite disk; the result is proportional to $\rho \pi a^2$. This quantity can be thought of as the magnitude of the total pressure reflected by an infinite disk which was disturbed by acoustic energy produced by a section of area πa^2 cut out of a plane wave that has the same particle velocity, [in our case unity], as does the piston source. This is simply an extension of Williams' reasoning discussed at the end of Section 7.1. In essence, the magnitude of the total pressure detected by the transducer is the same from all z -planes; no pressure/energy is lost because the reflecting disk is infinite and no loss mechanism has been introduced into the theory. Diffraction, in this case, probably introduces only a depth-dependent phase shift.

More insight can be gained by examining Eqs. 7.6–7.7. Note the first term in Eq. 7.6 is identical to right-hand side of Eq. 7.7. Thus, the first term in Eq. 7.6 represents

the infinite-reflector solution, and the second term represents the influence of diffraction [5]. Similar observations can be made about Eqs. 5.13–5.14. Furthermore, the factor of $1/k^2$ in the infinite-reflector solution indicates that the autoconvolution interpretation of two-way diffraction is dominated by a $1/f^2$ lowpass filtering effect.

The claim that autoconvolution diffraction with an infinite reflector is dominated by a $1/f^2$ filtering effect is consistent with the dotted lines shown in Figs. 5.4(c)–(d). Consider a finite reflector with radius $b = a$ in terms of the beam pattern of a transducer with radius a . Close in to the transducer, the beam is concentrated in a region bounded by the dimensions of the transducer. Thus, a finite reflector with radius $b = a$, as in Fig. 5.4(c), placed close to the transducer reflects most of the transmitted energy because it has the same dimensions as the transmitter. In effect, it is indistinguishable from an infinite reflector, and the dotted line in Fig. 5.4(c) is in excellent agreement with the theory.

Farther out from the transducer, the beam begins to spread or diffract, and a finite reflector placed further away from the transducer will not have the same effect as an infinite reflector. Thus, the dotted line in Fig. 5.4(c) are not consistent with the theory. Finally, the $1/f^2$ low-pass filtering effect for two-way diffraction is intuitively appealing: one-way diffraction squared. The result is appealing because of its symmetry, and this tempts us to claim that the depth-dependent phase shift associated with Eq. 7.7 is e^{-jk2z} .

7.2.3 Mirror-Image vs. Autoconvolution Diffraction

The previous sections offered new insights into diffraction from a circular aperture and revalidated certain aspects of the unified theory developed in the Chapters 3–5. The theory will now be used to present a new comparison of the mirror-image and autoconvolution interpretations of ultrasonic reflection imaging. This new comparison is based on Eq. 4.18 and Eqs. 5.13–5.15.

Specifically, monochromatic mirror-image and autoconvolution diffraction effects for different values of b were computed and plotted as a function of normalized depth. The parameters used were $c = 1540$ m/s, $a = 1$ cm, and $f = 1$ MHz. These parameters are

similar to those chosen by Bass in his 1958 work [5]. Both focused and unfocused diffraction effects were investigated, and Figs. 7.15–7.18 show the results. Fig. 7.15 illustrates unfocused results, and Figs. 7.16–7.18 show focused results. Spatially averaged results for mirror-image diffraction from a focused piston transducer are not included.

A detailed explanation of the figures is required because the graphs are difficult to interpret at first glance. The value of b used in computing the data is indicated in the title of each plot. The dotted line that appears in each of the plots in Fig. 7.15 is the well established one-way on-axis magnitude fluctuation for an unfocused piston transducer (circular aperture) [24, 48]:

$$\left| \hat{H}_1(\rho, z, t) \right|_{\rho=0}^2 = \frac{4}{k^2} \sin^2 \left(\frac{ka^2}{4z} \right). \quad (7.8)$$

This dotted line is often used to demarcate the near field and far field and is included as a familiar reference. Note that it is plotted in dB as a function of $z\lambda/a^2$ and that z has been used in calculating Eq. 7.8. Hence, the dotted line exhibits its last maximum at $z\lambda/a^2 = 1$.

The dashed lines in Fig. 7.15 show unfocused results based on a mirror-image interpretation of Eq. 4.18. That is, Eq. 4.18 was calculated using a depth of $2z$ but plotted as function of $z\lambda/a^2$ rather than $2z\lambda/a^2$. The solid lines show unfocused autoconvolution results based on Eqs. 5.13–5.15. These unfocused results will be discussed after explaining how to interpret the focused results in Figs. 7.16–7.18.

The value of b used in computing the focused data is indicated in each of the plots, and the dotted line that appears in each of the plots in Figs. 7.16–7.18 is based on the well established one-way on-axis magnitude fluctuation for a focused piston transducer [35]:

$$\left| \hat{H}_1(\rho, z, t) \right|_{\rho=0}^2 \approx \left[\frac{R}{R-z} \sin \left(\frac{ka^2}{4z} \frac{(R-z)}{R} \right) \right]^2. \quad (7.9)$$

Specifically, the dotted line in each of the plots in Figs. 7.16–7.18 is based on a mirror-image interpretation of Eq. 7.9; thus, the data were calculated using $2z$ in Eq. 7.9 but plotted as a function of $z\lambda/a^2$. This choice was made because no closed-form expressions were derived for spatially averaged one-way diffraction from a focused piston transducer

and no such results are plotted in the figures. The solid lines show focused autoconvolution results based on Eqs. 5.13–5.15.

The unfocused results shown in Fig. 7.15 reveal new insights into mirror-image and autoconvolution diffraction and simultaneously re-validate the theory developed in Chapters 3–5. First, the plots reveal that the mirror-image and autoconvolution interpretations of two-way diffraction are not as similar as previously thought. Section 1.5 stated that both the mirror-image and autoconvolution interpretations of ultrasonic reflection imaging have merit and implied that both interpretations produced similar results. Figs. 7.15–7.18 refute the implication for $b < a$ but confirm it for $b \approx a$ and $b > a$.

Specifically, attenuation predicted by the two interpretations for $b < a$ differs in two ways: (i) the minimum attenuation associated with each of the two interpretations occurs at different depths, and (ii) the attenuation predicted by the two interpretations varies greatly for all z . When $b \approx a$, the mirror-image and autoconvolution data are quite similar; they differ only by a fraction of a dB. (See also Figs. 7.1(d) and 7.2(d) which are included for comparison.)

When $b > a$, the attenuation predicted by the two interpretations does not differ by much. Note however that the mirror-image interpretation starts to break down for $b = 2a$, and this is probably due to the Fresnel approximation. Nonetheless, the graphs explain the popularity and acceptance of the mirror-image interpretation of two-way diffraction for $b \approx a$. They might also help to explain certain differences that Bass reported in his 1958 experiment on mirror-image diffraction [5, Fig. 2]. In particular, the plots of Bass's theoretical predictions and his experimental data are strikingly similar to the plots shown in Figs. 7.15 for $b = a$.

The unfocused results further validate the theory discussed in the previous chapters. Specifically, attenuation for a fixed depth z decreases with increasing b in both interpretations. In the limit as b approaches infinity, the attenuation theoretically is constant with depth z . The results shown in Fig. 7.15 are consistent with the mirror-image interpretation of Eq. 7.2 and Eq. 7.7. Loosely interpreted, the two equations state that an infinite

disk reflects all the energy originally emitted by the transducer. The magnitude of the reflected energy is modified only by a factor of k or k^2 depending on which interpretation is invoked; there is no dependence on depth z . The focused results shown in Figs. 7.16–7.18 show similar trends.

7.3 Two-Way Diffraction and Linear Models

Section 5.1 alluded to idiosyncrasies of linear models of ultrasonic reflection imaging. There are a number of linear models from which to choose, and several references propose suitable models [18, 29, 31, 60, 61, 64]. These linear models are similar in that they incorporate the autoconvolution interpretation of reflection imaging, but they differ in order and placement of time derivatives. Indeed, the linear model presented in Section 5.1 is the same as that proposed by Hunt, *et al.* [29] but modified with a second-order time-derivative. The focus of this section will be on the mirror-image and autoconvolution interpretations of two-way diffraction in linear models of ultrasonic imaging. The discussion will be axiomatic, cursory, and for the most part, qualitative. Nonetheless, new insights are promised.

Since the linear models in question are based on an autoconvolution of the one-way velocity potential impulse response, the model of one-way diffraction requires some discussion. Consider an ideal piston transducer being excited by one cycle of a sinusoid of a given frequency and a theoretical point receiver located some coaxial distance z from the transducer. This situation was investigated experimentally by Weight and Hayman [64] in 1978. The researchers investigated the response of a $75\text{-}\mu\text{m}$ radius wideband receiving element in the beam of a wideband unfocused piston transducer of 8-mm radius that was excited by a single cycle of a 3-MHz sinusoid. In the framework of our unified theory, the mathematics of the above experiment may be modeled as

$$v_R(z, t) = c_1 \left[\frac{\partial v_T(t)}{\partial t} * \langle h_1(z, t) \rangle_b \right] \quad (7.10)$$

where c_1 captures any constants of proportionality, $z = 20$ mm, $b = 75\mu\text{m}$, and the remaining terms are the same as before (Eq.5.1). Note the first derivative is used in Eq. 7.10

because we are considering one-way diffraction. Fig. 7.19 shows a plot of the results obtained from the one-way model in Eq. 7.10.

The results compare quite favorably to the theoretical and experimental results reported by Weight and Hayman; indeed, the theoretical results are virtually identical. Similar results would have been obtained had we used $\langle \hat{h}_1(z, t) \rangle_b$ instead of $\langle h_1(z, t) \rangle_b$ in Eq. 7.10. However, any derivative of other than first order would give very different results. Furthermore, it is important to emphasize that the results shown in Fig. 7.19 are based on spatially averaged diffraction theory, *not* on point theory.

Attention is now focused on two-way diffraction. Consider an ideal piston transducer being excited by one cycle of a given frequency and a theoretical point scatterer located at some coaxial distance z from the transducer. This situation was also investigated experimentally by Weight and Hayman. The researchers investigated the response obtained by insonifying a 0.4-mm on-axis disk with 4-MHz single-cycle excitation of a 16-mm diameter unfocused wideband transducer operating in pulse-echo mode.

In the autoconvolution interpretation of reflection imaging, the mathematics of the above experiment may be modeled

$$v_R(z, t) = c_2 \left[\frac{\partial^2 v_T(t)}{\partial t^2} * \langle \hat{h}_2(z, t) \rangle_b \right] \quad (7.11)$$

where c_2 captures any constants of proportionality, $z = 20$ mm, $b = 0.4$ mm, and the remainder of the terms are the same as before. Note the second derivative in Eq. 7.11. Fig. 7.20 shows that results obtained from Eq. 7.11 again compare quite favorably to the theoretical and experimental results reported by Weight and Hayman [64]. Similar results would have been obtained had $\langle h_2(z, t) \rangle_b$ in Eq. 7.11 been used. However, any derivative other than second order would give different results. It is again important to emphasize that the results shown in the figure are based on a spatially averaged diffraction theory, *not* on point theory.

Let us now apply the mirror-image interpretation of two-way diffraction in Eq. 7.11. In the mirror-image interpretation of reflection imaging, the mathematics of the previous

experiment may be modeled

$$v_R(z, t) = c_2 \left[\frac{\partial^2 v_T(t)}{\partial t^2} * \langle \hat{h}_1(2z, t) \rangle_b \right] \quad (7.12)$$

where $\langle \hat{h}_1(2z, t) \rangle_b$ captures the mirror-image interpretation, and the remainder of the terms are the same as before. The results from Eq. 7.12 are plotted in Fig. 7.21.

Unlike the previous results, the mirror-image results do not compare favorably to the theoretical and experimental results reported by Weight and Hayman [64]. Indeed, the mirror-image interpretation predicts only two output pulses while the autoconvolution interpretation predicts three. Two output pulses would have been obtained had $\langle \hat{h}_1(2z, t) \rangle_b$ been used in Eq. 7.12. An interesting observation in regards to time scaling is also noted. Recall that velocity-potential impulse responses are compressed with time for increasing values of z . Since $2z$ is used in computing mirror-image results, it is not surprising that the time separation between the two output pulses shown in Fig. 7.21 is half the separation between the two pulses shown in Fig. 7.19.

7.4 Chapter Summary

This chapter presented new material on mirror-image diffraction, autoconvolution diffraction, and linear models of ultrasound. Three special cases of one-way and two-way diffraction were investigated: (i) $b = a$ and two limiting cases (ii) $b \rightarrow 0$, and (iii) $b \rightarrow \infty$. The investigation further verified the predictive power of the proposed unified theory and led to a deeper understanding of diffraction from a circular aperture.

The limiting case $b \rightarrow 0$ demonstrated that the spatially integrated theory captured all salient features predicted by point theory. The second limiting case $b \rightarrow \infty$ revealed that one-way and two-way diffraction may be characterized as $1/f$ and $1/f^2$ filters, respectively. The comparison of mirror-image and autoconvolution diffraction revealed that the two interpretations behave quite differently for different values of b , and they are not as similar as previously thought. An investigation of linear models of ultrasonic reflection imaging

revealed that one-way models require only a first-order time derivative while two-way models require a second-order time derivative. Finally, it was discovered that the mirror-image interpretation of reflection imaging is probably not a good choice for computing the two-way velocity-potential impulse response.

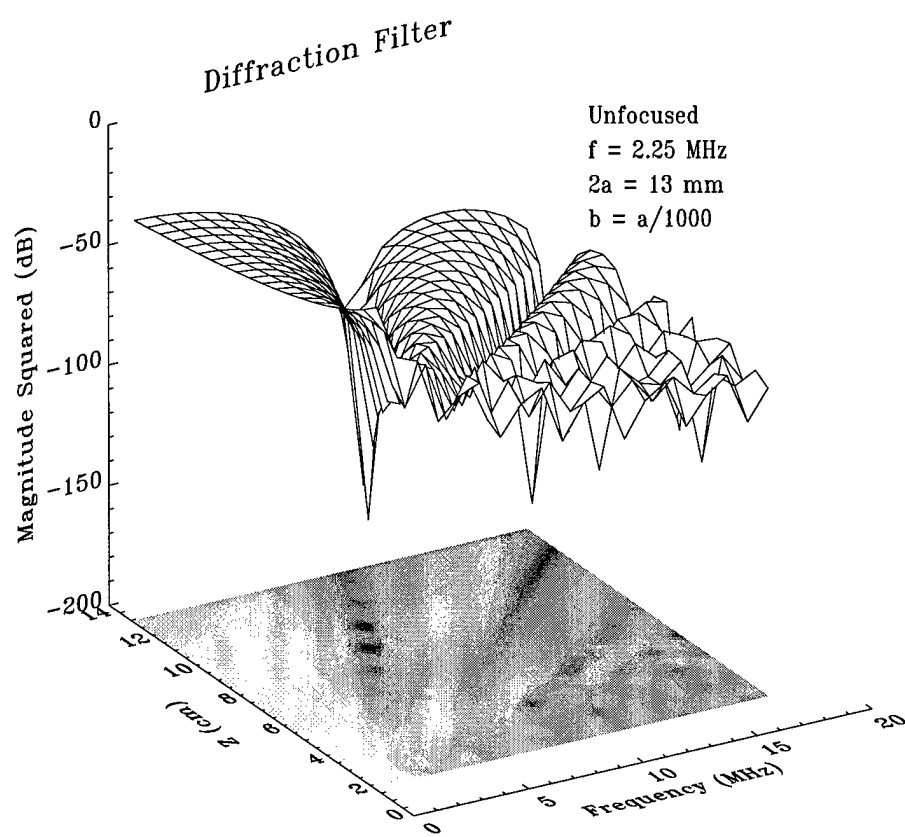


Figure 7.3: Unfocused autoconvolution: $b = a/1000$.

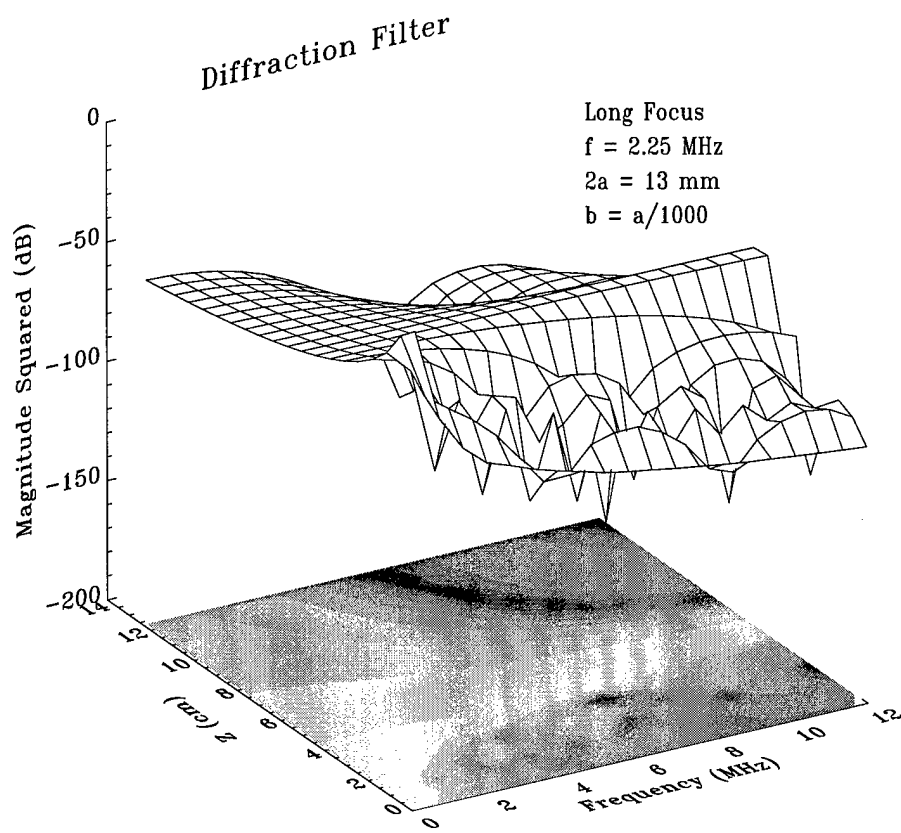


Figure 7.4: Long focus autoconvolution: $b = a/1000$.

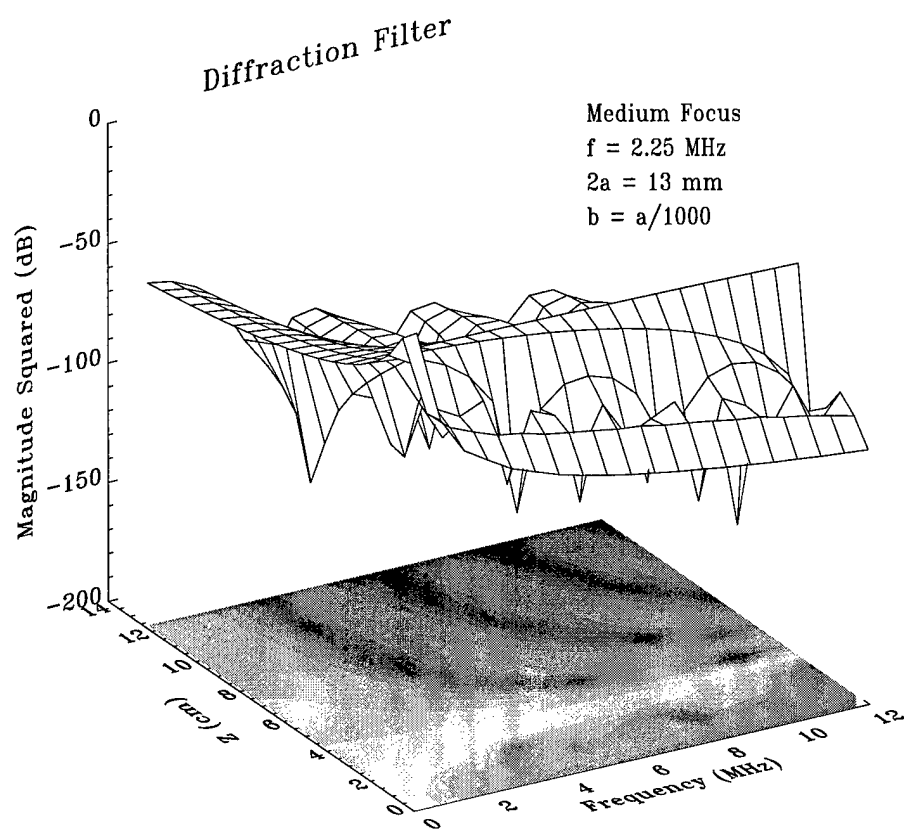


Figure 7.5: Medium focus autoconvolution: $b = a/1000$.

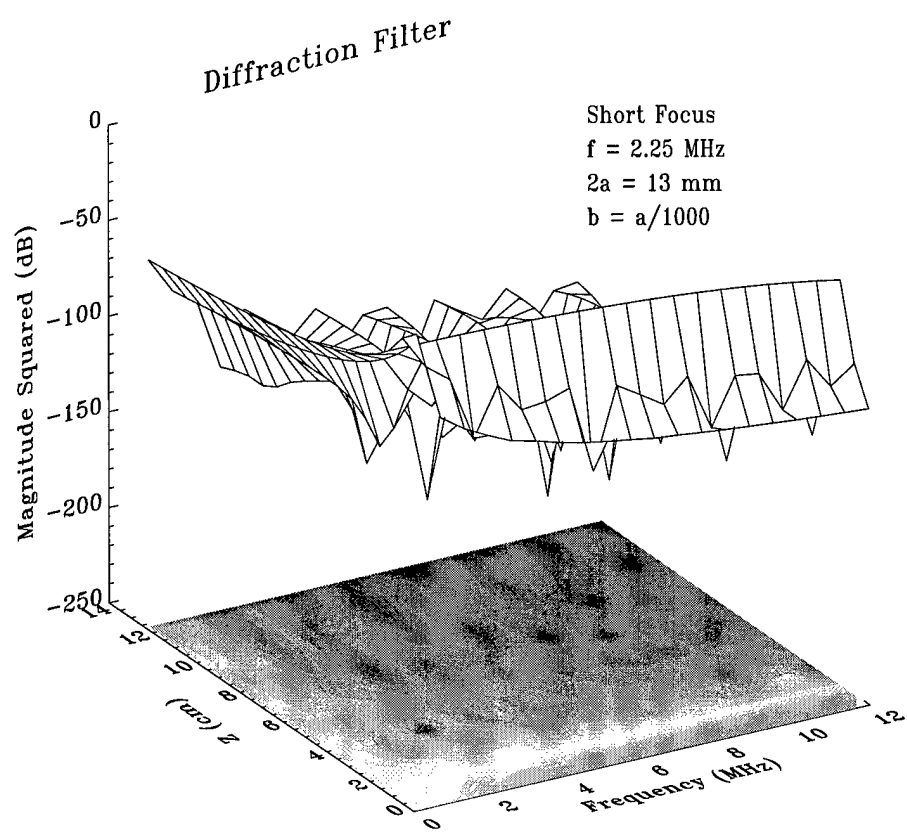


Figure 7.6: Short focus autoconvolution: $b = a/1000$.

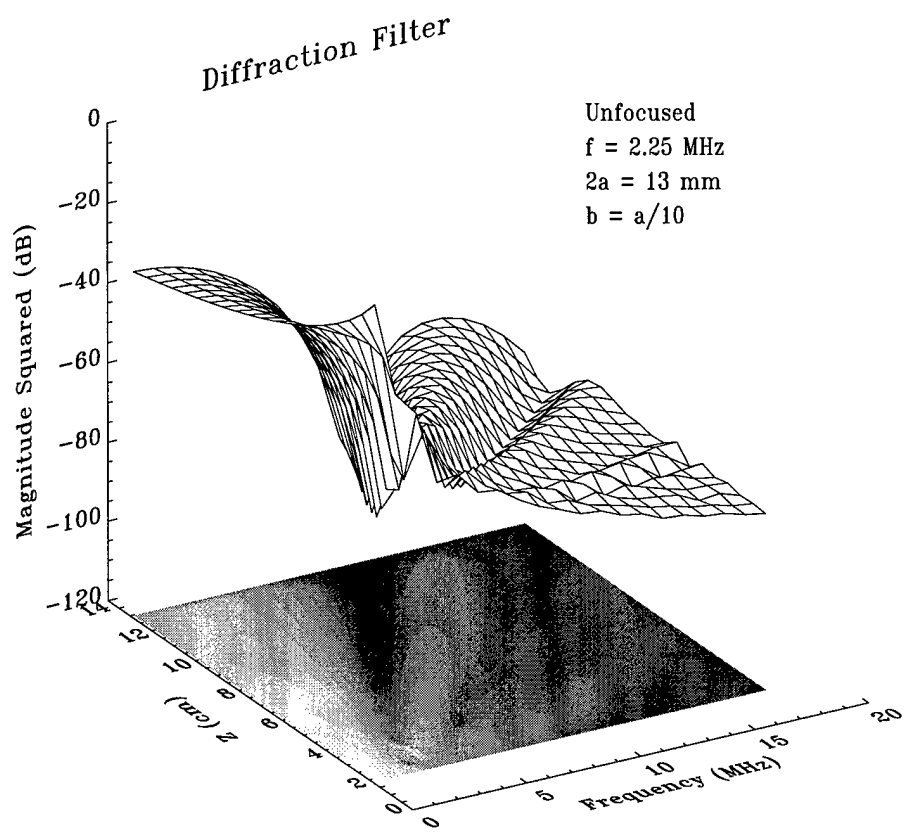


Figure 7.7: Unfocused autoconvolution: $b = a/10$.

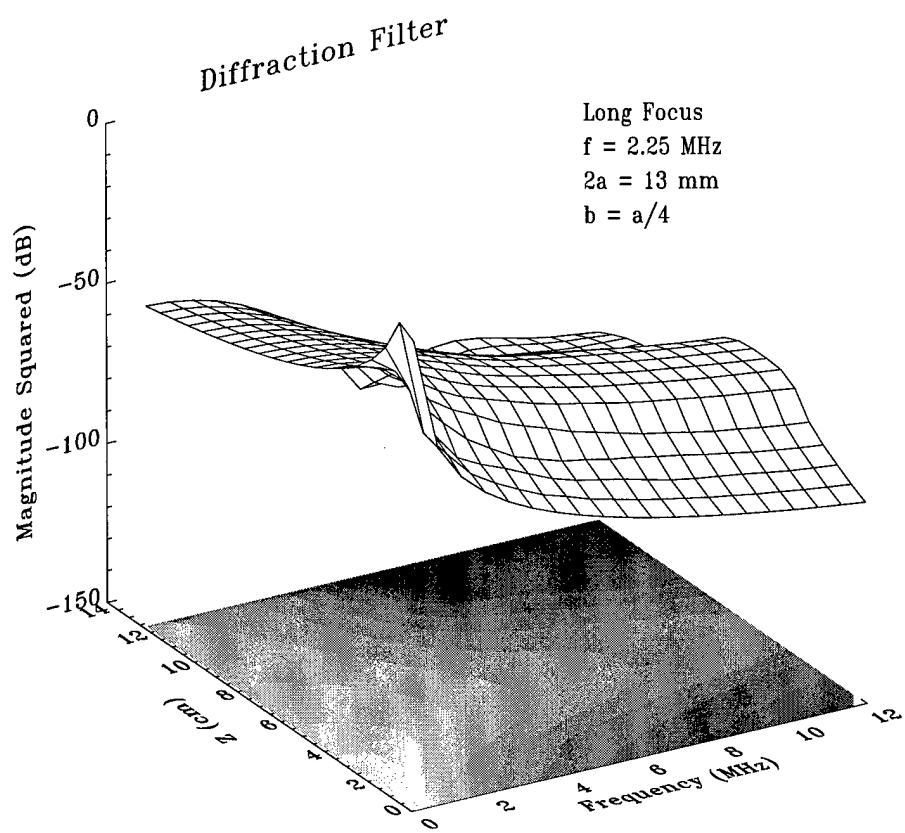


Figure 7.8: Long focus autoconvolution: $b = a/4$.

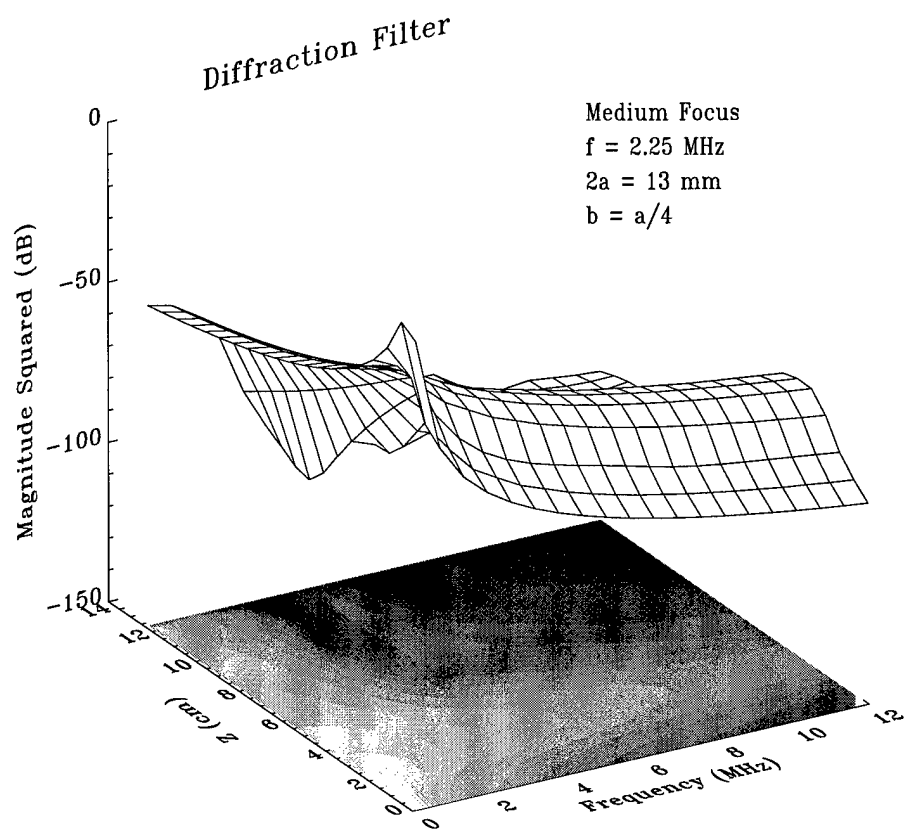


Figure 7.9: Medium focus autoconvolution: $b = a/4$.

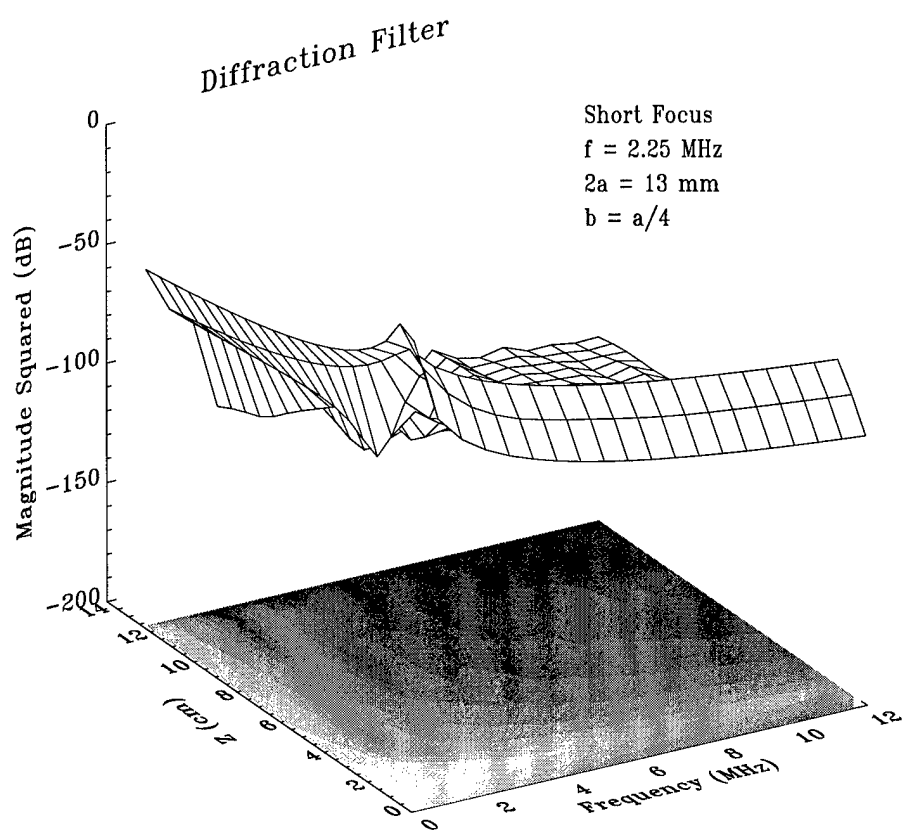


Figure 7.10: Short focus autoconvolution: $b = a/4$.

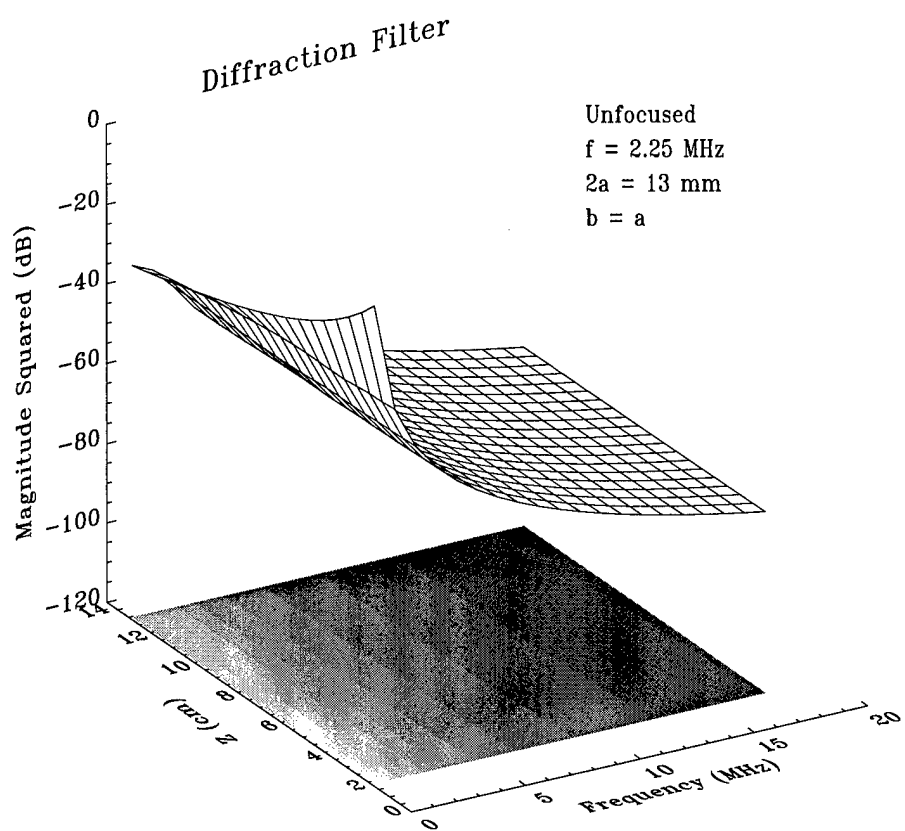


Figure 7.11: Unfocused autoconvolution: $b = a$.

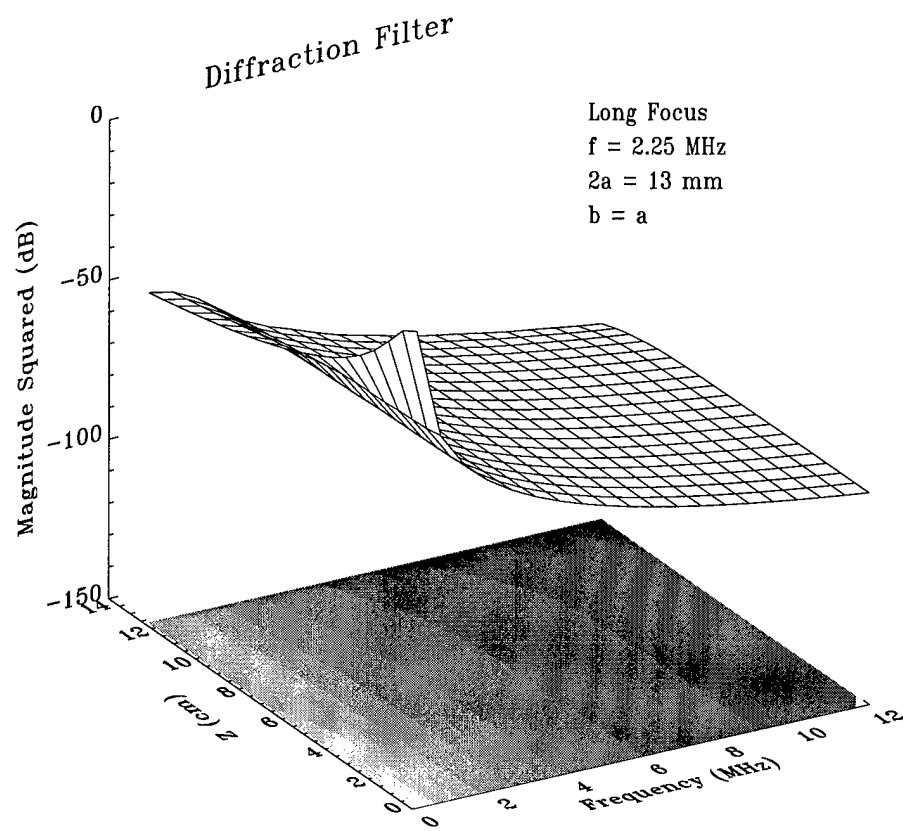


Figure 7.12: Long focus autoconvolution: $b = a$.

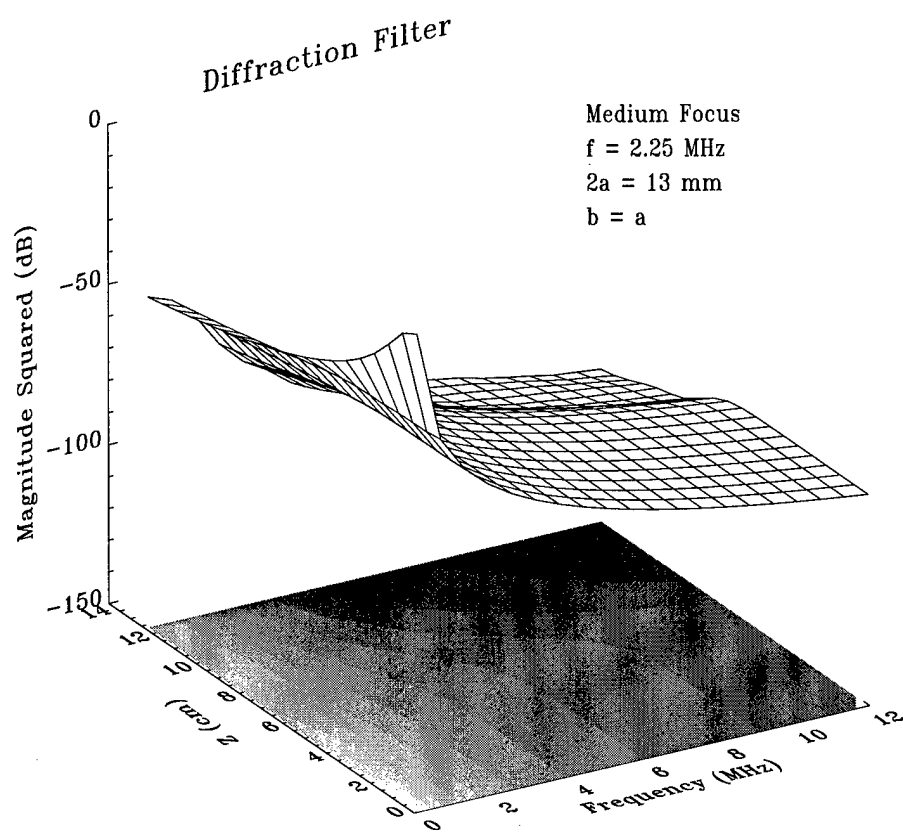


Figure 7.13: Medium focus autoconvolution: $b = a$.

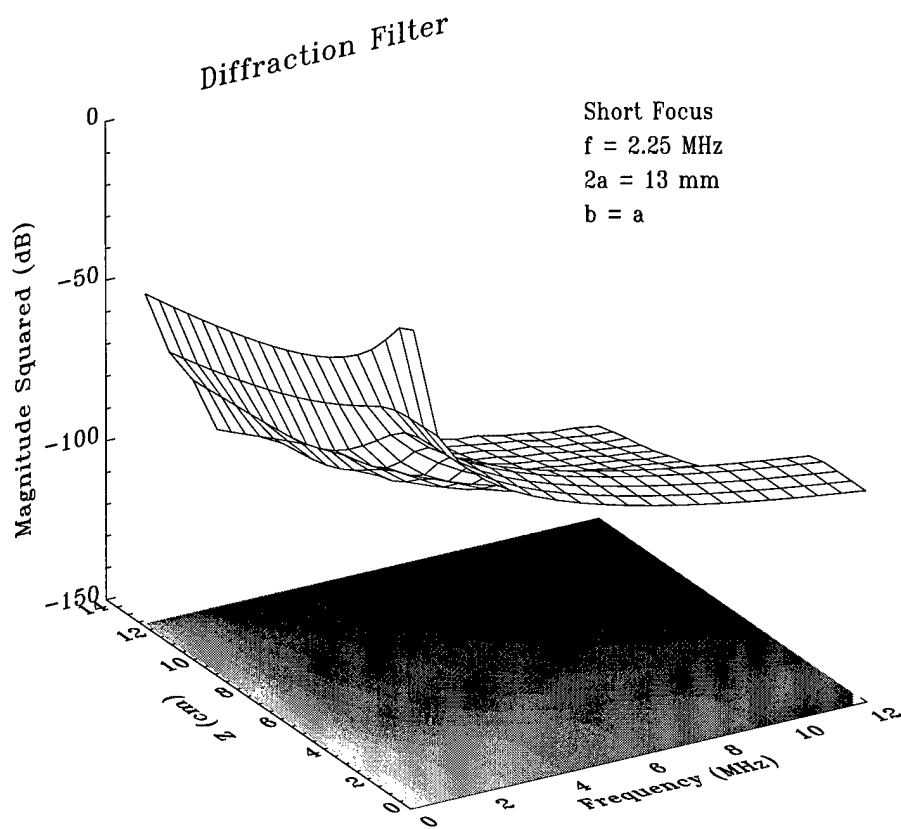


Figure 7.14: Short focus autoconvolution: $b = a$.

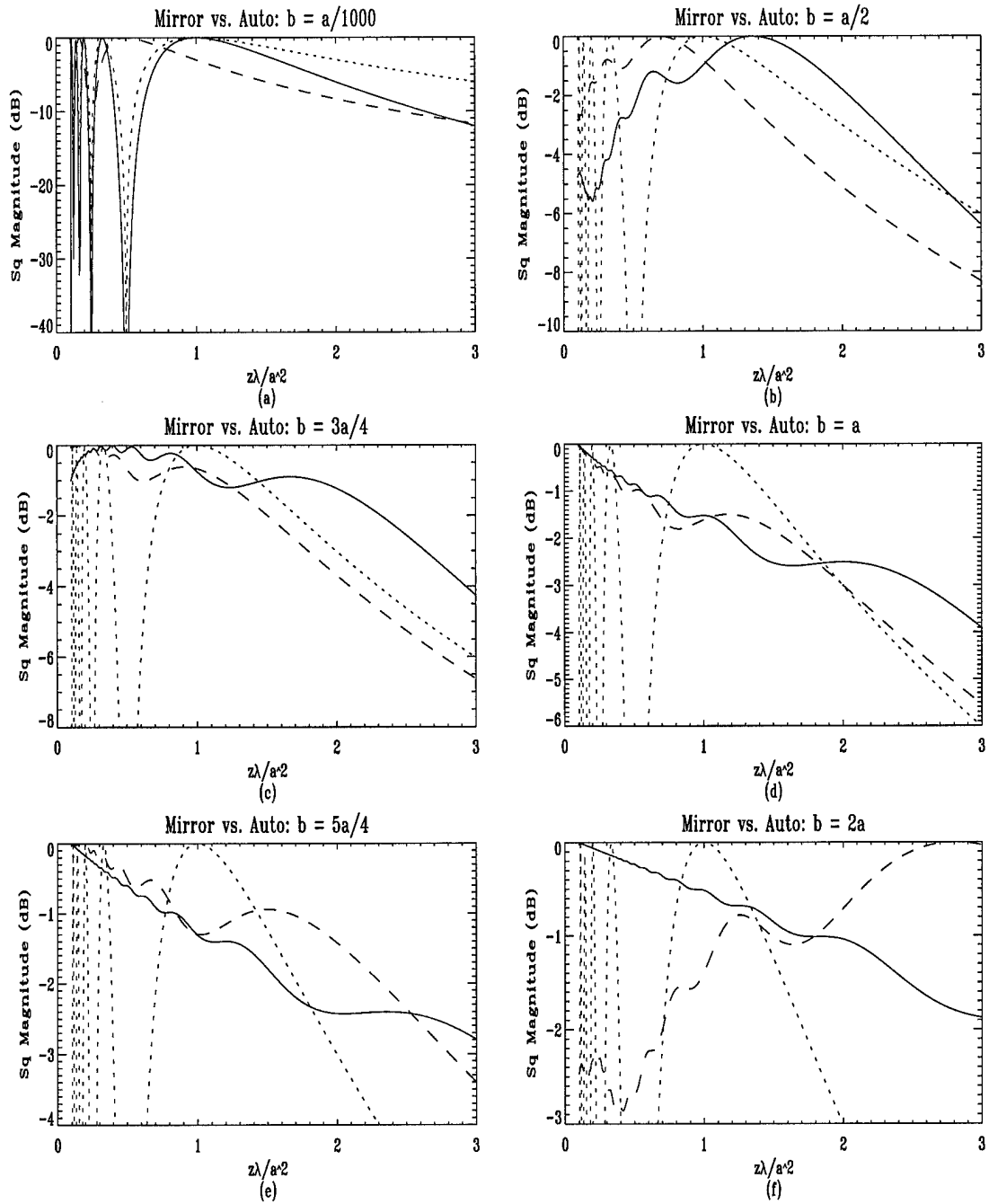


Figure 7.15: Mirror-image (dashed), autoconvolution diffraction (solid), and near-far field (dotted): unfocused.

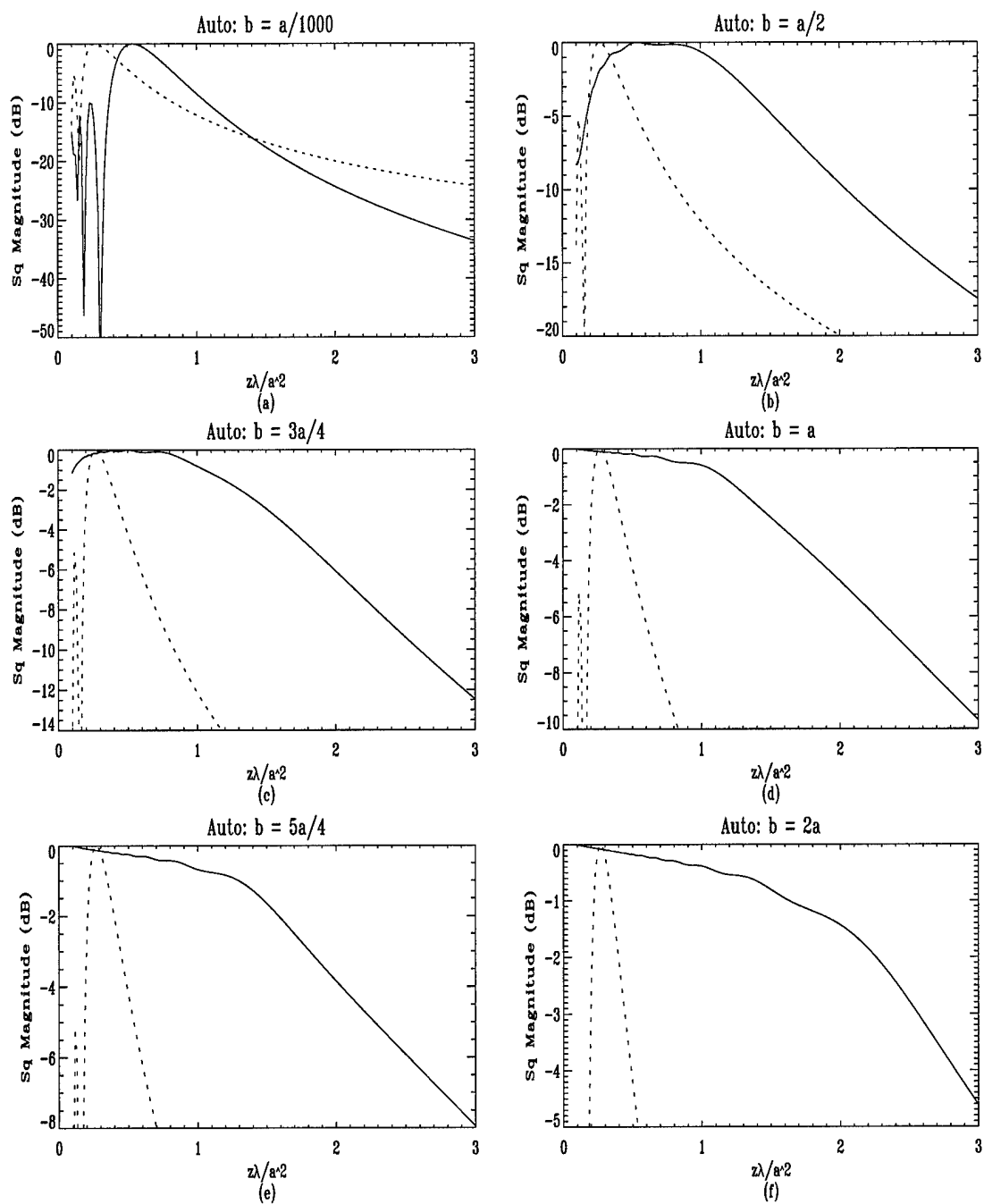


Figure 7.16: Mirror-image (dotted) and autoconvolution diffraction (solid): long focus.

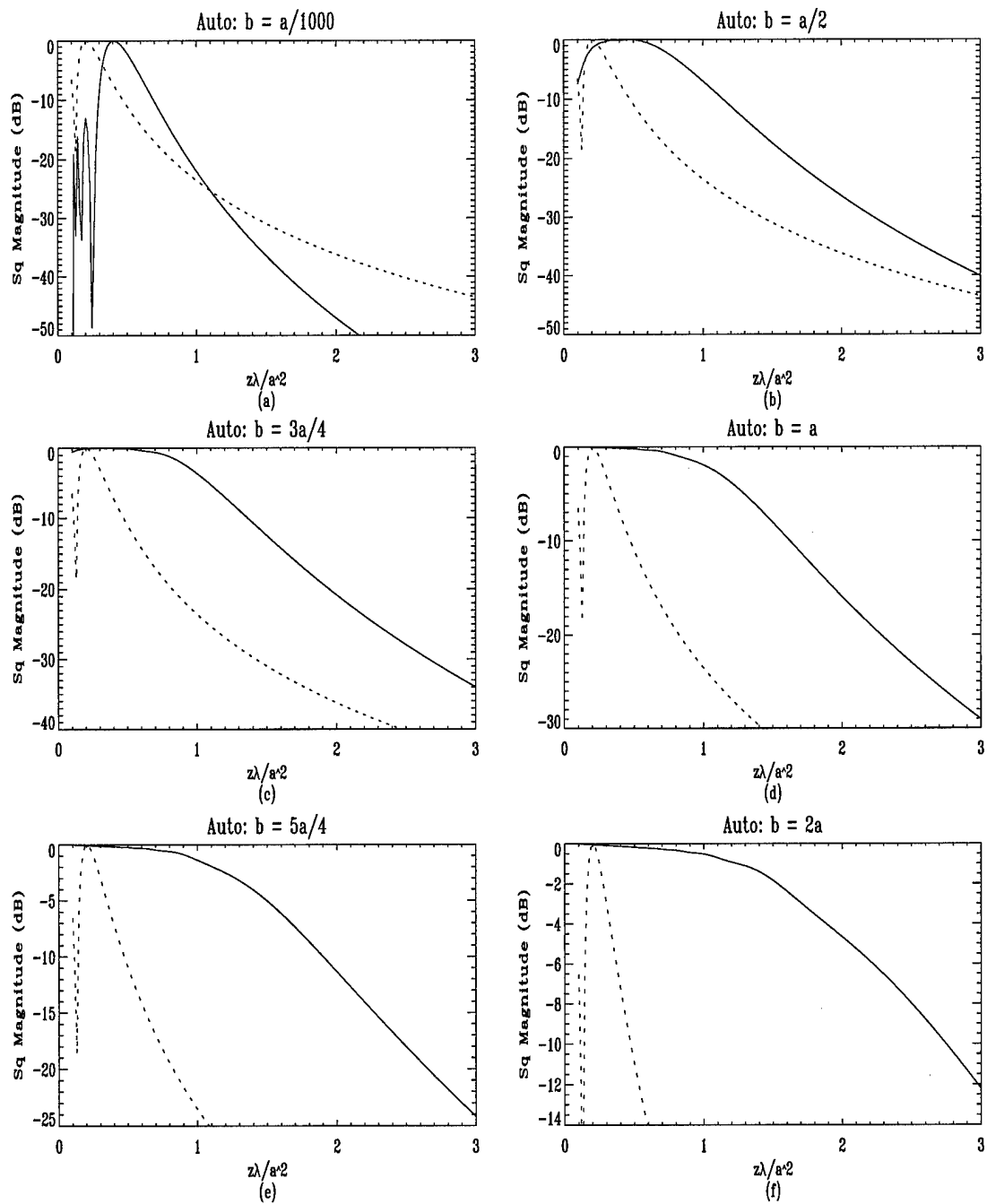


Figure 7.17: Mirror-image (dotted) and autoconvolution diffraction (solid): medium focus.

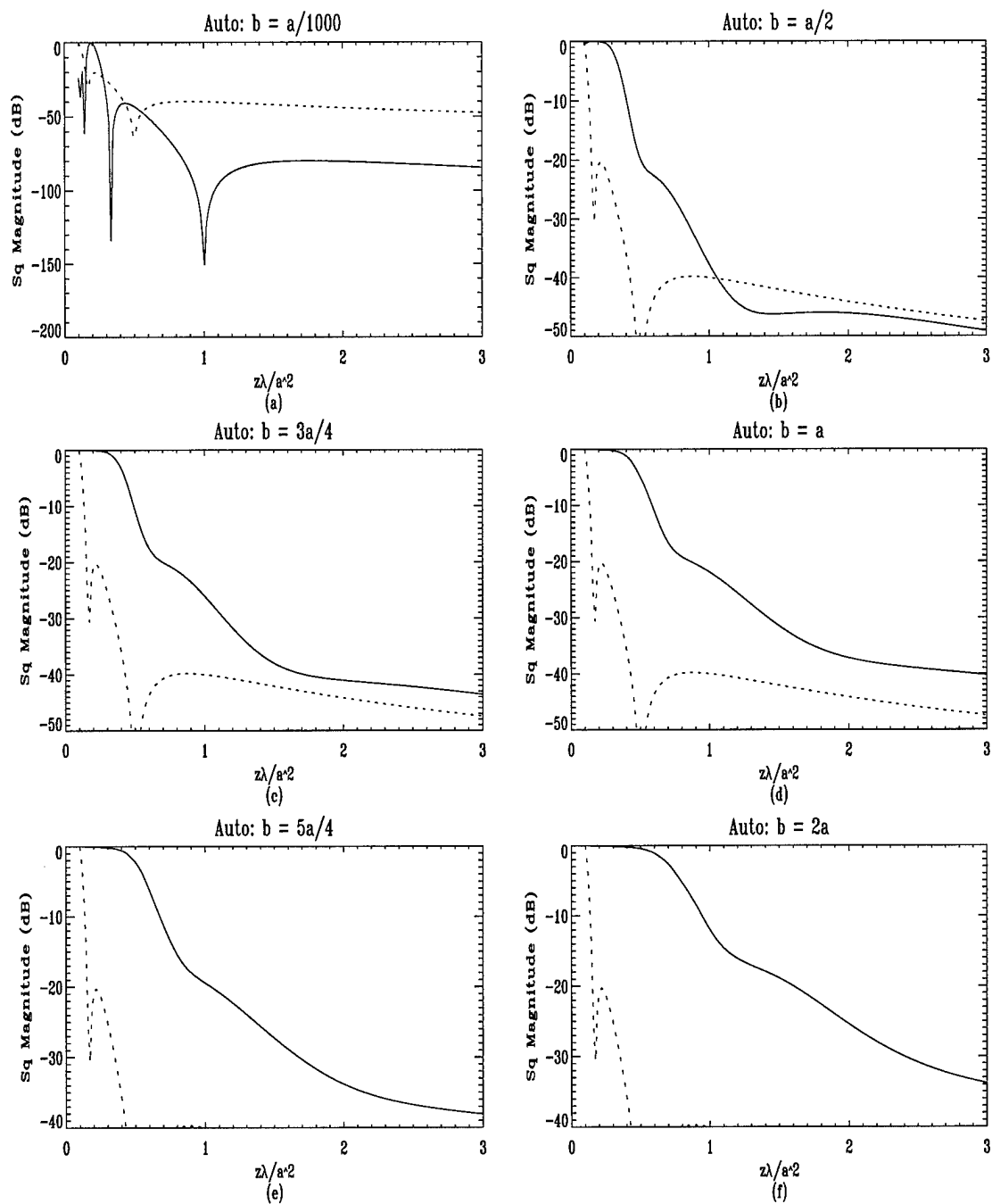


Figure 7.18: Mirror-image (dotted) and autoconvolution diffraction (solid): short focus.

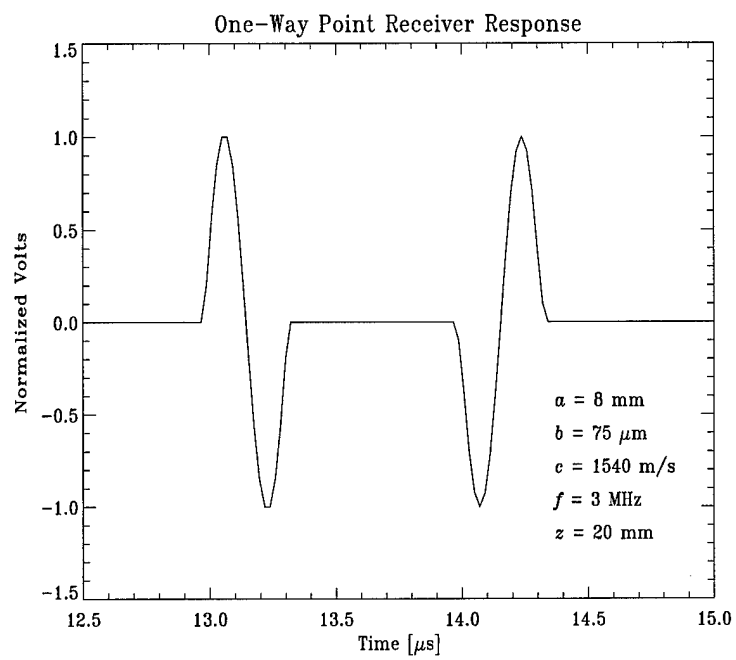


Figure 7.19: One-way response of an ideal point receiver: On- axis.

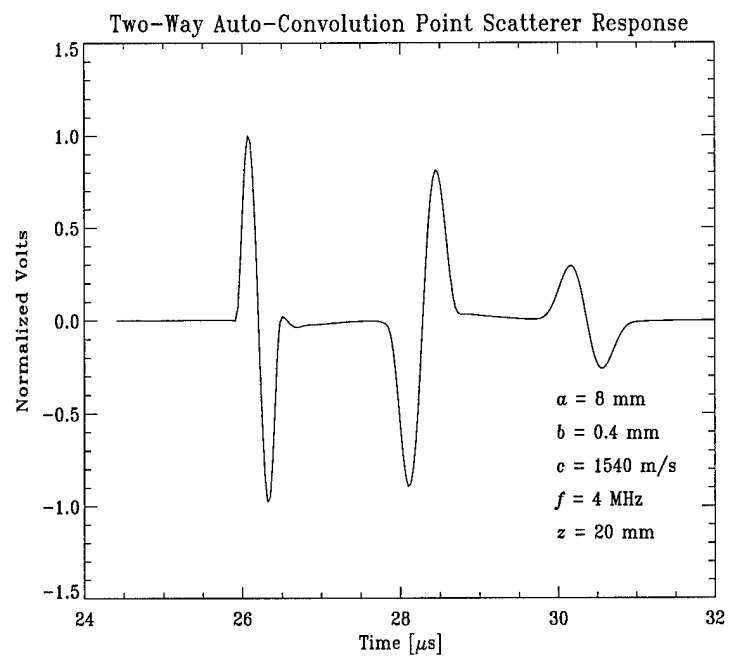


Figure 7.20: Ideal transducer response to on-axis point scatterer: autoconvolution.

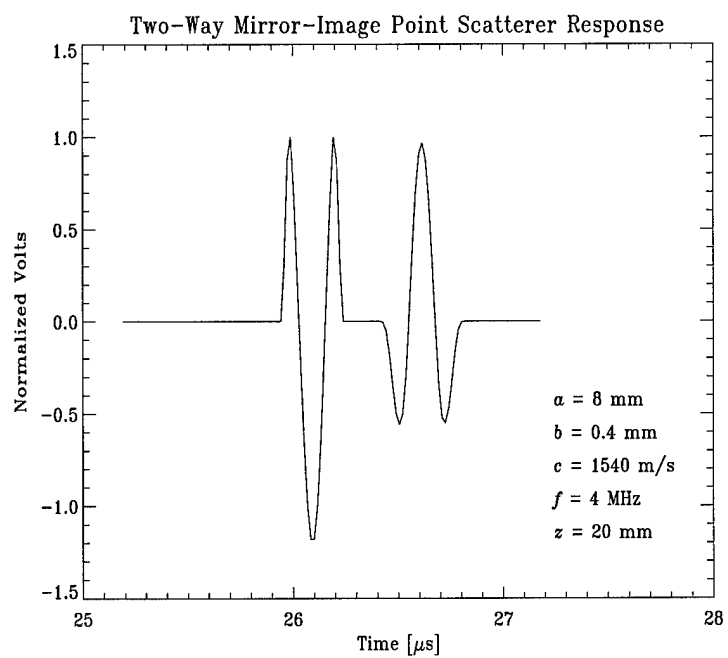


Figure 7.21: Ideal transducer response to on-axis point scatterer: Mirror-Image.

Chapter 8

Conclusions and Recommendations

Chapter 1 presented tutorial material, described the goals of this research, and explained how the research goals would be achieved. Chapter 2 provided a literature review and supplemented the tutorial material in Chapter 1 with more background information. Chapter 3 through Chapter 7 presented development, derivation, verification, validation, and application of a unified theory of spatially averaged diffraction corrections for piston transducers operating in pulsed mode. This chapter puts the unified theory and the entire document in perspective by combining a comparative literature review with a discussion of results. The document is concluded with a number of specific recommendations for further research.

8.1 Conclusions

8.1.1 Research Goals

This research had three goals. The first was to derive a closed-form spatially averaged two-way diffraction correction for a focused piston transducer operating in pulsed mode. The second was to develop a unified theory of spatially averaged diffraction corrections for piston transducers. The final goal was to advance the scientific community's understanding of diffraction from a circular aperture. The goals were met.

8.1.2 Fourier Equivalence

Section 1.3 stated that the Fourier equivalence of the arccos and the Lommel diffraction formulations as an approximate Fourier transform pair has been overlooked. It has been overlooked for two reasons. First, the Lommel and arccos formulations are based on monochromatic and impulsive excitation, respectively; hence, they are usually treated separately in the literature on ultrasound. Second, the very notion of an *approximate* Fourier transform in terms of time and frequency is unconventional.

In Chapter 3, we outlined derivations of the arccos and Lommel diffraction formulations, compared the two formulations, introduced the notion of an approximate Fourier transform pair, and, ultimately, unified the arccos and Lommel diffraction formulations in way previously unreported in the literature on ultrasound. Chapter 3 also put these two seminal descriptions of diffraction from a circular aperture in new perspective. Specifically, Section 3.1 showed that the Lommel formulation for diffraction from a circular aperture is a monochromatic frequency-domain expression based on the Fresnel approximation to the Rayleigh-Sommerfeld integral of scalar diffraction theory. Thus, the Lommel diffraction formulation can be interpreted as a convolution involving a depth-dependent quadratic phase factor (Eq. 3.5). On the other hand, Section 3.2 showed that the arccos formulation for diffraction from a circular aperture is a set of polychromatic time-domain expressions based on the exact Rayleigh-Sommerfeld integral (with obliquity factor of unity). The arccos diffraction formulation was interpreted in terms of a depth-dependent time-scaling operation.

Section 3.4 presented quantitative evidence leading to the conclusion that the Fourier equivalence of the arccos and Lommel diffraction formulations form an approximate Fourier transform pair for both focused and unfocused piston transducers. Indeed, it was shown that the Lommel diffraction formulation captures the magnitude response, phase response, and time-scaling predicted by the arccos diffraction formulation. Numerical results obtained from both formulations showed good overall agreement in the Fresnel region.

8.1.3 Spatially Averaged One-Way Diffraction

The Fourier equivalence of the arccos and Lommel diffraction formulations as an approximate Fourier transform pair was established in Chapter 3. This Fourier equivalence was further exploited in Chapter 4 to derive general closed-form frequency-domain expressions describing one-way diffraction for unfocused piston transmitters and receivers (Eq 4.18). The expressions are general in the sense that the area of the receiver may be less than, equal to, or greater than that of the transmitter. The frequency-domain expressions were derived within the framework of Lommel's treatment of Fresnel diffraction. Additionally, a closed-form time-domain description of one-way diffraction for a finite receiver of any radius (Eq. 4.5) was derived. No focused results were derived for the one-way case.

Arccos Diffraction Formulation

The closed-form time-domain expression describing spatially averaged one-way diffraction effects for a finite receiver of any radius was derived in Section 4.1. The expression itself is not new [10] but its derivation is. The derivation consisted of spatially averaging the integral form of the arccos diffraction formulation and interpreting the result as a Fourier-Bessel or Hankel transform. The result, Eq. 4.5, was shown to be simply a scaled version of the cylinder-function cross correlation derived by Gaskill [22, pp. 302–304] for optical diffraction. This realization led to interesting insights concerning optical and one-way ultrasonic diffraction.

Lommel Diffraction Formulation

A general set of closed-form frequency-domain expressions that describe spatially averaged one-way diffraction effects for a finite receiver of any radius was derived (Eq. 4.18). Lommel's interpretation of Fresnel diffraction served as a unified framework for the derivation. The derivation of Eq. 4.18 differs from previous treatments. For example, Williams [66, Eq. 28] derived one of the first spatially integrated results for one-way diffraction from an unfocused

piston transducer in 1951. His result also is monochromatic but is limited to a receiver having an area equal to that of the transmitter. Bass's 1958 closed-form result [5, Eq. 14] is limited in a similar way. Almost two decades would pass before Williams derived a more general result applicable to transmitters and receivers having different areas [67, Eq. 39]. Unlike the derivation of Eq. 4.5, Williams' 1951 and 1971 results were not derived in a unified mathematical framework; thus, the derivations are somewhat difficult to follow.

It should be mentioned that Rogers and Van Buren used Lommel's treatment of Fresnel diffraction in deriving a closed-form spatially integrated result for one-way diffraction from a unfocused piston transducer in 1974 [54]. However, their work differs from that presented in Section 4.2 in two ways. First, their result is limited to transmitters and receivers having equal areas. Second, they did not integrate the Lommel diffraction formulation directly; instead they presented two alternative methods of obtaining their result. The first relied on the method of stationary phase [48], while the second began with an adaptation of Weber's second exponential integral [63]. Eq. 4.18, which includes Eq. 10 in [54], was derived in a more accessible and elegant fashion by integrating the Lommel diffraction formulation directly. While Eq. 4.18 is general in terms of transmitter and receiver areas, it *is not* applicable to focused transducers. The interested reader is referred to Chen *et al.* for closed-form expressions [11, Eq. 22 & Eq. 24] describing spatially averaged one-way diffraction from a focused piston transducer.

Extending Fourier Equivalence

Section 4.3 compared results obtained from the time-domain and frequency-domain expressions just discussed. These showed remarkable agreement for conditions meeting the Fresnel approximation. Furthermore, the results verified the theoretical prediction that the Fourier equivalence of the arccos and Lommel diffraction formulations can be extended to spatially averaged one-way diffraction. No such comparison or analysis exists in the literature. Finally, all results derived in Section 4.3 can be used in the mirror-image interpretation of two-way diffraction simply by doubling z in Eq. 4.5 and Eq. 4.18.

8.1.4 Spatially Averaged Autoconvolution Diffraction

Chapter 5 attacked autoconvolution diffraction using Lommel's treatment of Fresnel diffraction from a circular aperture. Application of the Cauchy-Schwarz inequality for integrals along with an *ad hoc* assumption allowed a set of closed-form expressions derived by Wolf in 1951 [68] for optical diffraction to be applied to spatially averaged autoconvolution diffraction (Eqs. 5.13–5.15). Although the expressions in Eqs. 5.13–5.15 do not consider phase, they are completely general in that they are theoretically applicable to a reflecting disk of any radius and to both focused and unfocused piston transducers. Fourier equivalence of the arccos and Lommel diffraction formulations was extended to spatially averaged autoconvolution diffraction, and the assumption of minimum phase allowed estimation of the phase response. Results obtained from the closed-form Lommel-based expressions autoconvolution diffraction were compared with the results obtained by numerically integrating an autoconvolution of the arccos diffraction formulation. The normalized results showed remarkable agreement in the Fresnel region despite the number of assumptions made to arrive at the results.

The only other closed-form solution for spatially averaged autoconvolution diffraction was derived by Cardoso and Fink [9] in 1991. Their work is limited to a magnitude-only expression, and magnitude responses derived via Eqs. 5.13–5.15 agree qualitatively with those presented in [9]. Fink and Cardoso did not obtain impulse responses from their results nor did they compare magnitude-only results to numerically integrated arccos results. The application of Wolf's 1951 equations for optical diffraction to ultrasound and the results obtained are new developments in ultrasound.

8.1.5 Experimental Investigation

Chapter 6 presented results from an experimental investigation of the unified diffraction theory developed in Chapter 5. Specifically, autoconvolution diffraction corrections based on Eqs. 5.13–5.15 were implemented with time-varying filters, and diffraction-corrected

B-mode images were reconstructed using a short-time Fourier analysis/synthesis algorithm. The raw and diffraction-corrected images were compared qualitatively. Differences between raw and corrected RF data were analyzed via spectral quantitatively centroids.

The experimental investigation was a preliminary application of theory designed to gauge only the practicality of autoconvolution diffraction corrections; it was not designed to be a comprehensive test of the theory. Despite its preliminary nature, the investigation included ten laboratory experiments. No study on diffraction correction contains as many examples as presented in Chapter 6; see, for example, [9, 13, 20]. Although the visual and spectral differences between the raw and diffraction-corrected data were subtle, the overall results are quite promising. At best, the proposed autoconvolution diffraction corrections improved the visual quality of the ultrasound images while simultaneously unbiasing the spectral centroids. At worst, the proposed diffraction corrections did, as Hippocrates taught, no harm.

8.1.6 Analytical Investigation

An analytical investigation presented in Chapter 7 demonstrated the practicality and power of the unified theory developed in Chapters 3–5. The investigation showed the unified theory accurately predicts diffraction effects in the limiting cases of a point receiver (scatterer) and an infinite receiver (reflector). Section 7.2.3 quantitatively compared the mirror-image and autoconvolution interpretations of two-way diffraction in a new way; the comparison showed that the two interpretations are not as similar as previously thought. Finally, linear models of ultrasonic reflection imaging were considered in Section 7.3; it was shown that mirror-image interpretation may not be suitable for computing two-way impulse responses.

8.2 Recommendations for Improvement and Further Research

This research has produced a unified theory of spatially averaged diffraction corrections for ultrasonic piston transducers operating in pulsed mode. Most of the theory has been

cast in closed-form and verified analytically and numerically. Additionally, autoconvolution diffraction corrections were applied experimentally. Despite this, much more work needs to be done.

8.2.1 General

This section points out three general aspects of the unified theory requiring further research. First, the closed-form spatially averaged results and the numerically integrated results neglect the mathematical singularities inherent in the arccos and Lommel diffraction formulations. The Lommel diffraction formulation was spatially averaged by integrating over $\rho d\rho$; thus, these results do not account for energetic contributions from the radial origin ($\rho = 0$). Similarly, the arccos diffraction formulation (Eqs. 3.11–3.12) is problematic when $ct = z$ and $\rho = a$. For the purposes of this work, these two singularities were neglected. Despite this, the overall results presented in the previous chapters showed reasonable agreement. Energetic contributions from these singularities may need to be included in future work.

The second issue concerns computation of the equations presented in Section 1.9. In this work, all results were obtained by programming the equations explicitly in do-loops. This style may be avoided if recursion relations are used which may also reduce processing time. At any rate, recursion relations for most of the equations in Section 1.9 can be found in the references [25, 63, 68, 69]. Finally and most importantly, large-scale experimentation designed to test the practical limits and clinical applicability of the entire theory is imperative.

8.2.2 Fourier Equivalence

The Fourier equivalence of the arccos and Lommel diffraction formulations as an approximate Fourier transform pair was rigorously demonstrated for unfocused piston transducers and indirectly demonstrated for focused piston transducers. Thus a study of focused piston transducers following the same format as Chapter 3.5 is required. The arccos diffraction formulation for a focused piston transducer can be found in [2], and Eq. 3.18 gives the

Lommel diffraction formulation for a focused piston transducer. The study should investigate long, short, and medium focusing [46]; it should also delineate where the arccos and Lommel diffraction formulations for focused piston transducers agree and disagree.

8.2.3 Spatially Averaged One-Way Diffraction

Chapter 4 presented a detailed theoretical treatment of spatially averaged one-way diffraction for unfocused piston transducers. An experimental study of finite receivers is needed to validate the theory; the experiments could be modeled after those in [64]. From a theoretical perspective, a study comparing spatially averaged one-way diffraction effects obtained from Eq. 4.11 and previously tabulated values [7, 32] would make a useful project.

No results for focused piston transducers were derived in Chapter 4, and this gaping hole needs to be filled. Doing so, however, will be difficult. Basic probability reveals that a completely general closed-form solution for spatially averaged one-way diffraction would have to cover 36 combinations including the following variations:

- focused or unfocused transmitter: 2 choices,
- focused or unfocused receiver: 2 choices,
- transmitter area $<$, $=$, and $>$ receiver area: 3 choices,
- transmitter focal length $<$, $=$, and $>$ receiver focal length: 3 choices.

Add to this the fact that closed-form results would have to be derived in the time and frequency domains. The strictly unfocused results in Eq. 4.5 and Eq. 4.18 and the focused results derived by Chen, *et al.* [11] would ease the burden somewhat but, clearly, this is a long-term project. Here again, experiments modeled after those in [64] would serve to test the theory.

8.2.4 Spatially Averaged Autoconvolution Diffraction

Chapter 5 presented an *ad hoc* derivation of spatially averaged autoconvolution diffraction effects for both focused and unfocused piston transducers. The Fourier equivalence of the

arccos and Lommel diffraction formulations in conjunction with the assumption of minimum phase allowed the derivation of Eq. 5.16. To the extent that Eq. 5.11 is valid, Eq. 5.16 is also valid for both focused and unfocused transducers. Eq. 5.16 was analytically verified for the unfocused case in terms of both magnitude and phase and for the focused case in terms of magnitude only.

Thus, a study of focused piston transducers following the format of Section 5.4 is required. The arccos diffraction formulation for a focused piston transducer can be found in [2], and it would have to be numerically integrated. Eq. 5.16 could be used as is, as long as the time reversal for $z > R$ is observed. The study should investigate long, short, and medium focusing [46] and delineate where the arccos and Lommel diffraction formulations for spatially averaged autoconvolution diffraction agree and disagree. Of course, an experimental study of reflection by large planar disk reflectors is needed to validate the theory; the experiments could be modeled, again, after those done by Weight and Hayman [64].

The derivation of spatially averaged autoconvolution diffraction is lacking in three respects. First, a closed-form time-domain expression for spatially averaged autoconvolution diffraction could not be derived because Eq. 5.3 was too difficult to solve analytically even for the unfocused case. We are doubtful that a closed-form solution can be found, if indeed one exists. Smarter minds may prevail. Along the same lines, Eq. 5.4 proved difficult to solve in closed form even after substituting $H_1(\rho, z, \omega)$ with $\hat{H}_1(\rho, z, \omega)$, the Lommel diffraction formulation. Nonetheless, we are somewhat optimistic that a closed-form solution can be found provided the Lommel diffraction formulation is used in Eq. 5.4. Despite our less-than-enthusiastic optimism, finding a closed-form solution, if one exists, will take great ingenuity and tenacity. Finally, the *ad hoc* assumption of approximate equality in Eq. 5.11 requires quantitative and qualitative elucidation.

8.2.5 More Experiments and Analysis

Section 1.5 explained that ultrasonic reflection imaging is a volumetric or 3-D imaging modality; thus, volume averaging is more realistic than spatial averaging over a planar disk.

Thus, both the mirror-image and autoconvolution interpretations of two-way diffraction are patently incorrect. However, spatial averaging over a volume is significantly more difficult, both analytically and computationally, than spatial averaging over a planar disk. With no other viable alternative, numerous researchers in ultrasound assume spatial averaging over a planar disk gives a reasonably accurate estimate of reality. The question then becomes what size disk should be used in calculating diffraction corrections. Though touched on in Section 6.1, no definitive answer was postulated. Obtaining a more definitive answer is possible with extensive experimentation and subsequent data analysis. Our suspicion is that the radius of the disk b will have to be varied as a function of depth z .

As mentioned in Section 1.4, both the mirror-image and autoconvolution interpretations of two-way diffraction have physical merit and mathematical appeal. Experiments designed to compare the two interpretations would be of great interest to the ultrasound community. The experiments should focus not on which interpretation is correct; neither can be in a strict sense. Rather, the experiments should be designed to determine conditions under which the two interpretations hold. Another suggestion is for an analytical and experimental investigation of linear models of ultrasound. The analytical portion of the investigation would compile a reasonably thorough and authoritative bibliography of linear models on ultrasonic reflection imaging. The bibliography should include (i) a quantitative and qualitative discussion of similarities and differences amongst the models, (ii) rigorous dimensional analysis of terms contained in the models, and (iii) simulations based on a representative sampling of the more cogent models. The experimental portion would compare data obtained from experimental data with results obtained from simulations.

One final recommendation is to study the psychophysical effects of diffraction correction. Trained observers, such as radiologists, sonographers, and researchers in ultrasound, could compare raw and diffraction-corrected images and provide qualitative and quantitative evaluations of the images. The evaluations could be subsequently analyzed using the tools of psychophysics. This is probably the most meaningful follow-on work that could be done.

Appendix A

Two Lemmas

Lemma 1.

$$\sum_{s=0}^{\infty} (-1)^s U_{n+2s}(u, v) = Z_n(u, v) \quad (\text{A.1})$$

Proof.

$$\begin{aligned} \sum_{s=0}^{\infty} (-1)^s U_{n+2s}(u, v) &= \sum_{s=0}^{\infty} (-1)^s \sum_{p=0}^{\infty} (-1)^p \left(\frac{u}{v}\right)^{n+2s+2p} J_{n+2s+2p}(v) \\ &= \sum_{s=0}^{\infty} \sum_{p=0}^{\infty} (-1)^{s+p} \left(\frac{u}{v}\right)^{n+2s+2p} J_{n+2s+2p}(v) \end{aligned} \quad (\text{A.2})$$

Collecting terms of the same order in $J_n(v)$ and arranging the series in ascending order, the lemma follows. The grouping of terms is justified since the series is absolutely convergent.

□

Lemma 2.

$$\begin{aligned} \frac{1}{u} \int_u^{v_b} v U_n(u, v) e^{-j \frac{v^2}{2u}} dv &= \left\{ e^{-j \frac{u}{2}} [Z_{n+1}(u, u) - j Z_n(u, u)] \right. \\ &\quad \left. + e^{-j \frac{v_b^2}{2u}} [j Z_n(u, v_b) - Z_{n+1}(u, v_b)] \right\} \end{aligned} \quad (\text{A.3})$$

Proof.

$$\begin{aligned} \frac{1}{u} \int_u^{v_b} v U_n(u, v) e^{-j \frac{v^2}{2u}} dv &= \frac{1}{u} \int_u^{v_b} v \left\{ \sum_{s=0}^{\infty} (-1)^s \left(\frac{u}{v} \right)^{n+2s} J_{n+2s}(v) \right\} e^{-j \frac{v^2}{2u}} dv \\ &= \sum_{s=0}^{\infty} (-1)^s \int_u^{v_b} \left(\frac{v}{u} \right)^{1-(n+2s)} J_{n+2s}(v) e^{-j \frac{v^2}{2u}} dv \end{aligned} \quad (\text{A.4})$$

The interchanging of the summation and integration sign above is justified since the series under the integral sign is uniformly convergent in the range of integration. An observation due to Watson [63, p. 543] in conjunction with Euler's formula leads to

$$\begin{aligned} \frac{d}{dt} \left[j e^{-j \frac{1}{2} w t^2} U_n \left(\frac{z^2}{w}, z t \right) - e^{-j \frac{1}{2} w t^2} U_{n+1} \left(\frac{z^2}{w}, z t \right) \right] \\ = z \left(\frac{w t}{z} \right)^{1-n} J_n(z t) e^{-j \frac{1}{2} w t^2}. \end{aligned} \quad (\text{A.5})$$

Setting $t = v, w = 1/u$, and $z = 1$ yields

$$\frac{d}{dv} \left[j e^{-j \frac{v^2}{2u}} U_n(u, v) - e^{-j \frac{v^2}{2u}} U_{n+1}(u, v) \right] = \left(\frac{v}{u} \right)^{1-n} J_n(v) e^{-j \frac{v^2}{2u}}. \quad (\text{A.6})$$

The right-hand side of Eq. A.6 and the integrand of Eq. A.4 are in the same form. Thus, Lemma 2 follows from the fundamental theorem of integral calculus and application of Lemma 1. \square

Lemma 1 and Lemma 2 are simply extensions of Lemma 8 and Lemma 9, respectively, in [68].

Bibliography

- [1] R. Altes and W. Faust. A unified method of broad-band echo characterization for diagnostic ultrasound. *IEEE Transactions on Biomedical Engineering*, BME-27(9):520–538, September 1980.
- [2] M. Arditi. Transient fields of concave annular arrays. *Ultrasonic Imaging*, 3:37–61, 1981.
- [3] M. Averkiou, *et al.* A new imaging technique based on the nonlinear properties of tissues. In *1997 IEEE Ultrasonics Symposium*, pages 1561–1565, 1997.
- [4] J. Bamber and M. Tristram. Diagnostic ultrasound. In S. Webb, editor, *The Physics of Medical Imaging*, chapter 7. IOP Publishing Ltd, Bristol, England, 1988. ISBN 0-85274-349-1.
- [5] R. Bass. Diffraction effects in the ultrasonic field of a piston source. *Journal of the Acoustical Society of America*, 30(7):602–605, July 1958.
- [6] P. Bello. Characterization of randomly time-variant linear channels. In B. Goldberg, editor, *Communications Channels: Characterization and Behavior*, pages 4–37. IEEE Press, New York, NY, 1976. Reprinted from *IEEE Trans. Comm. Sys.*, Vol. CS-11, Dec 1963, pp. 360–393.
- [7] G. Benson and O. Kiyohara. Tabulation of some integral functions describing diffraction effects in the ultrasonic field of a circular piston source. *Journal of the Acoustical Society of America*, 55(1):184–185, January 1974.
- [8] R. Bracewell. *Two-Dimensional Imaging*. Prentice-Hall, Englewood Cliffs, NJ, 1995.
- [9] J. Cardoso and M. Fink. Echographic diffraction filters and the diffraction function for random media through an instantaneous time-frequency approach. *Journal of the Acoustical Society of America*, 90(2, Part 1):1074–1084, August 1991.
- [10] D. Cassereau, *et al.* Time deconvolution of diffraction effects—Application to calibration and prediction of transducer waveforms. *Journal of the Acoustical Society of America*, 84(3):1073–1085, September 1988.
- [11] X. Chen, *et al.* Acoustic coupling from a focused transducer to a flat plate and back to the transducer. *Journal of the Acoustical Society of America*, 95(6):3049–3054, June 1994.
- [12] T. Christopher. Finite amplitude distortion-based inhomogeneous pulse echo ultrasonic imaging. *IEEE Transactions on Ultrasonics, Ferroelectronics, and Frequency Control*, 44(1):125–139, January 1997.
- [13] I. Claesson and G. Salomonsson. Frequency- and depth-dependent compensation of ultrasonic signals. *IEEE Transactions on Ultrasonics, Ferroelectronics, and Frequency Control*, 35(5):1–6, September 1978.
- [14] R. Courant and F. John. *Introduction to Calculus and Analysis*, volume I. Interscience Publishers, New York, NY, 1965.
- [15] R. Crochiere. A weighted overlap-add method of short-time fourier analysis/synthesis. *IEEE Transactions on Acoustics, Speech, and Signal Processing*, ASSP-28(1):99–101, February 1980.
- [16] P. Daponte, *et al.* Detection of echoes using time-frequency analysis techniques. *IEEE Transactions on Instrumentation and Measurements*, 45(1):30–40, February 1996.
- [17] F. Dunn, editor. *Ultrasonic Tissue Characterization*. Springer, Hong Kong, 1996.
- [18] M. Fink. Theoretical study of pulsed echographic focusing procedures. In P. Alais and A. Metherell, editors, *Acoustical Imaging*, volume 10. Plenum Press, New York, NY, 1982.

- [19] M. Fink and J. Cardoso. Diffraction effects in pulse-echo measurement. *IEEE Transactions on Sonics and Ultrasonics*, SU-31(4):313–329, July 1984.
- [20] M. Fink, *et al.* Ultrasonic signal processing for *in vivo* attenuation measurement: Short-time Fourier analysis. *Ultrasonic Imaging*, 5:117–135, 1983.
- [21] R. Gagliardi. *Introduction to Communications Engineering*. John Wiley & Sons., New York, NY, second edition, 1988.
- [22] J. Gaskill. *Linear Systems, Fourier Transforms, and Optics*. Wiley, New York, NY, 1978.
- [23] H. Goldstein. *Classical Mechanics*. Addison-Wesley, Reading, MA, 1950.
- [24] J. Goodman, editor. *Introduction to Fourier Optics*. McGraw-Hill Book Co., San Francisco, CA, 1968.
- [25] A. Gray and G. Mathews. *A Treatise on Bessel Functions and Their Applications to Physics*. Dover Publications, Inc., New York, NY, 1966. First published in 1922.
- [26] G. Harris. Review of transient field theory for a baffled planar piston. *Journal of the Acoustical Society of America*, 70(1):10–19, July 1981.
- [27] G. Harris. Transient field of a baffled planar piston transducer having an arbitrary vibration amplitude distribution. *Journal of the Acoustical Society of America*, 70(1):186–204, July 1981.
- [28] F. Hlawatsch and G. Boudreaux-Bartels. Linear and quadratic time-frequency signal representations. *IEEE Signal Processing Magazine*, 9(2):21–67, 1992.
- [29] J. Hunt, *et al.* Ultrasound transducers for pulse-echo medical imaging. *IEEE Transactions on Biomedical Engineering*, BME-30(8):453–481, 1983.
- [30] H. Huntington, *et al.* Ultrasonic delay lines. I. *Journal of the Franklin Institute*, 245(1), January 1948. See pp. 16–23.
- [31] J. Jensen. A model for the propagation and scattering of ultrasound in tissue. *Journal of the Acoustical Society of America*, 89:182–190, January 1991.
- [32] A. Khimunin. Numerical calculation of the diffraction corrections for the precise measurement of ultrasound absorption. *Acustica*, 27:173–181, January 1972.
- [33] G. Kino, editor. *Acoustic Waves: Devices, Imaging, & Analog Signal Processing*. Prentice-Hall, Inc., Englewood Cliffs, NJ, 1987.
- [34] L. Kinsler, *et al.* *Fundamentals of Acoustics*. John Wiley & Sons., New York, NY, third edition, 1982.
- [35] G. Kossoff. Analysis of focusing action of spherically curved transducers. *Ultrasound in Medicine & Biology*, 5:359–365, 1979.
- [36] R. Kuc. Modeling acoustic attenuation of soft tissue with a minimum-phase filter. *Ultrasonic Imaging*, 6:24–36, 1984.
- [37] R. Kuc and D. Regula. Diffraction effects in reflected ultrasound spectral estimates. *IEEE Transactions on Biomedical Engineering*, BME-31(8):537–545, August 1984.
- [38] J. Lim, editor. *Advanced Topics in Signal Processing*. Prentice-Hall, Inc., Englewood Cliffs, NJ, 1988.
- [39] M. Linzer, editor. *Ultrasonic Tissue Characterization*, volume 453. National Bureau of Standards, October 1976. A NBS Special Publication.
- [40] A. Macovski. *Medical Imaging Systems*. Prentice-Hall, Englewood Cliffs, NJ, 1983.
- [41] M. Malik, *et al.* Joint-time frequency processing of ultrasonic signals. In D. Thompson and D. Chimenti, editors, *Review of Progress in Quantitative Nondestructive Evaluation*, volume 15, pages 2089–2096. Plenum Press, New York, NY, 1996.
- [42] P. Morse and K. Ingard. *Theoretical Acoustics*. McGraw-Hill, New York, NY, 1968.
- [43] S. Nawab and T. Quatieri. Short-time fourier transform. In Lim [38], chapter 6.
- [44] F. Oberhettinger. On transient solutions of the “baffled piston” problem. *Journal of Research of the National Bureau of Standards-B: Mathematics and Mathematical Physics*, 65B(1):1–5, 1961.

- [45] A. Oppenheim and R. Shafer. *Discrete-Time Signal Processing*. Prentice Hall, Englewood Cliffs, NJ, 1989.
- [46] Panametrics, Inc., Waltham, MA. *Ultrasonic Products for Nondestructive Testing*, 1988.
- [47] E. Papadakis and K. Fowler. Broad-band transducers: Radiation field and selected application. *Journal of the Acoustical Society of America*, Unknown(Unknown):729–745, December 1969.
- [48] A. Papoulis. *Systems and Transforms with Applications in Optics*. McGraw-Hill Book Co., New York, NY, 1968. See Chapters 5 and 9.
- [49] A. Penttinen and M. Luukkala. The impulse response and pressure nearfield of a curved ultrasonic radiator. *Journal of Physics D: Applied Physics*, 9:1547–1557, 1976.
- [50] J. Quistgaard. Signal acquisition and processing in medical diagnostic ultrasound. *IEEE Signal Processing Magazine*, pages 21–67, 1997.
- [51] S. Rabiner and D. Schaefer. *Digital Processing of Speech Signals*. Prentice-Hall PTR, Upper Saddle River, NJ, 1996.
- [52] T. Rhyne. Radiation coupling of a disk to a plane and back or a disk to disk: An exact solution. *Journal of the Acoustical Society of America*, 61(2):318–324, February 1977.
- [53] M. Riley. *Speech Time-Frequency Representations*. Kluwer Academic Publishers, Boston, MA, 1989.
- [54] P. Rogers and A. Van Buren. An exact expression for the Lommel diffraction correction integral. *Journal of the Acoustical Society of America*, 55(4):728–728, April 1974.
- [55] G. Salomonsson and L. Bjökman. On the separation of attenuation and texture of tissue using a parametric time-varying network. *IEEE Transactions on Ultrasonics, Ferroelectrics, and Frequency Control*, UFFC-33(3):280–286, May 1986.
- [56] H. Seki, *et al.* Diffraction effects in the ultrasonic field of a piston source and their importance in the accurate measurement of attenuation. *Journal of the Acoustical Society of America*, 28(2):230–238, March 1956. There are numerous typos in this article.
- [57] K. Shung, *et al.* *Principles of Medical Imaging*. Academic Press, San Diego, CA, 1992.
- [58] R. Silverman, *et al.* Measurement of ocular tumor volumes from serial, cross-sectional ultrasound scans. *Retina*, 13(1):69–74, January–March 1993.
- [59] P. Stepanishen. Transient radiation from pistons in an infinite planar baffle. *Journal of the Acoustical Society of America*, 49:1627–1638, July 1971.
- [60] P. Stepanishen. Pulsed transmit/receive response of ultrasonic piezoelectric transducers. *Journal of the Acoustical Society of America*, 69:1815–1826, June 1981.
- [61] J. Thijssen. Echographic image processing. In P. Hawkes, editor, *Advances in Electronics and Electron Physics*, volume 84, pages 317–349. Academic Press, Inc., San Diego, CA, 1992.
- [62] Y. Wang and P. Fish. Comparison of doppler signal analysis techniques for velocity waveform, turbulence and vortex measurement: A simulation study. *Ultrasound in Medicine & Biology*, 22(5):635–649, 1996.
- [63] G. Watson. *A Treatise on The Theory of Bessel Functions*. Cambridge University Press, New York, NY, 1980. First published in 1922.
- [64] J. Weight and A. Hayman. Observations of the propagation of very short ultrasonic pulses and their reflection by small targets. *Journal of the Acoustical Society of America*, 63(2):396–404, February 1978.
- [65] A. Wheelon. *Tables of Summable Series and Integrals Involving Bessel Functions*. Holden-Day, San Francisco, CA, 1968.
- [66] A. Williams, Jr. The piston source at high frequencies. *Journal of the Acoustical Society of America*, 23(1):1–6, January 1951.
- [67] A. Williams, Jr. Integrated signal on circular piston receiver centered in a piston beam. *Journal of the Acoustical Society of America*, 48(1):285–289, 1970.
- [68] E. Wolf. Light distribution near focus in an error-free diffraction image. *Proceedings of the Royal Society, A*, 204:533–548, 1951.

- [69] E. Wolf. The X_n and Y_n functions of Hopkins, occurring in the theory of diffraction. *Journal of the Optical Society of America*, 43(3):218, March 1953.
- [70] R. Ziemer, *et al.* *Signals and Systems*. Macmillan Publishing Co., Inc., New York, NY, 1983.